Materials
Technology Reports

https://ojs.acad-pub.com/index.php/MTR

2024 VOLUME 2 ISSUE 1
ISSN: 3029-2646 (Online)

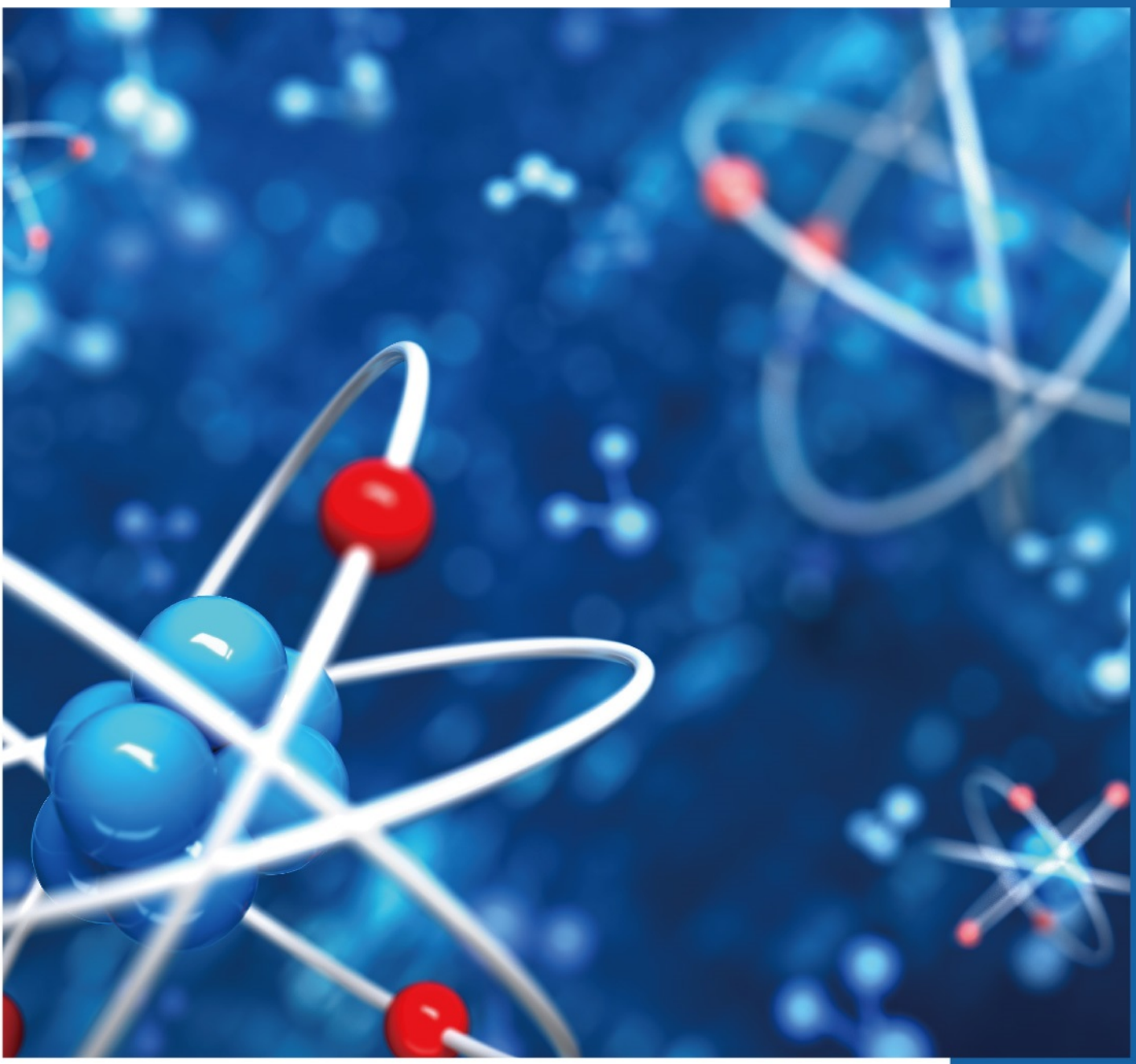

1

Editorial Team

Editor-in-Chief

Editorial Board Members

Maiyong Zhu
Jiangsu University
China

Aqib Mashood Khan
Nanjing University of Aeronautics and Astronautics
China

Volume 2 Issue 1 • 2024

Materials Technology Reports

ACADEMIC
ACADEMIC PUBLISHING PTE LTD

2024 | Volume 2 | Issue 1

Materials Technology Reports

https://ojs.acad-pub.com/index.php/MTR

Contents

Articles

Materials Technology Reports 2024, 2(1), 461.
https://doi.org/10.59400/mtr.v2i1.461

Article

Structural and electrical characteristics of Zr-doped HfO_2 (HZO) thin films deposited by atomic layer deposition for RRAM applications

P. R. Sekhar Reddy

Semiconductor Laboratory, SASTRA-MHI Training Center, SASTRA Deemed University, Thanjavur 613401, India;
drsekharreddy@sastra.ac.in

CITATION

Sekhar Reddy PR. Structural and electrical characteristics of Zr-doped HfO_2 (HZO) thin films deposited by atomic layer deposition for RRAM applications. Materials Technology Reports. 2024; 2(1): 461. https://doi.org/10.59400/mtr.v2i1.461

ARTICLE INFO

Received: 27 June 2023
Accepted: 2 August 2023
Available online: 8 January 2024

Abstract: In this study, Zr-doped HfO_2 (HZO) based resistive random-access memory (RRAM) device were fabricated. The Hf:Zr (1:1) ratio in the HZO films were controlled by changing the HfO_2 and ZrO_2 cycle ratio during the atomic layer deposition (ALD) process. Next, we studied the structural and electrical properties of the Au/HZO/TiN RRAM device structure. The RRAM devices exhibits an excellent resistance ratio of the high resistance state (HRS) to the low resistance state (LRS) of ~10^3 A, and as well as good endurance (300 cycles) and retention (>10^3 s), respectively. Further, the device showed different conduction mechanism in LRS and HRS modes. The lower biased linear region is dominated by ohmic conductivity, whereas the higher biased nonlinear region is dominated by a space charge limited current conduction. This device is suitable for application in future high-density nonvolatile memory RRAM devices.

Keywords: non-volatile memory; RRAM; resistive switching; atomic layer deposition; charge transport mechanism

1. Introduction

Resistive random access memory (RRAM), is emerging as an potential candidate for next-generation data storage system [1]. The key features of RRAM are high-speed operation, simple fabrication, low-power consumption, and good-scalability [2,3]. The RRAM devices consist of a simple capacitor-like structure consisting of an insulating/dielectric layer sandwiched between two metal electrodes [4,5]. They exhibit reversible resistive switch behaviour when applied to unipolar or bipolar voltages [6].

In RRAM devices, resistive switching behaviour can be achieved with variety of transition metal oxides (TMOs), including HfO_2, ZrO_2 TiO_2, NiO, and ZnO [7]. In recent years, TMO materials have attracted considerable attention and have been widely investigated due to their excellent resistive switching abilities and simple fabrication process [8]. Among them, the HfO_2 and ZrO_2 films are extremely promising candidates because of their high dielectric constant, wide band gap, excellent thermal stability and complementary metal oxide semiconductor (CMOS) technology [9,10]. This makes them a significant advantage for integrating resistive switching devices using CMOS technology. Meanwhile, flexible electronic devices that are light weight and flexibility are drawing a lot of attention in the next generation of wearable devices. The thin films based on HfO_2/ZrO_2 are hence ideal for flexible RRAM applications.

In order to achieve better resistive switching characteristics for memory devices, a doping process is often required to improve endurance performance and uniformity

[11]. Previously, limited studies have been performed on HZO-based RRAM devices [12,13]. However, while HfO_2 and ZrO_2-based resistive switches perform well in certain areas, their characteristics are still insufficient to meet the application requirements [14]. So far, the resistive switching capabilities of strongly orientated HZO film RRAMs have not been investigated. It is worthwhile to develop highly orientated HZO thin films and test their performance as resistive switching memories. Herein, a low-temperature ALD technique was developed for Zr-doped HfO_2 RRAM structures. However, the Au/HZO/TiN RRAM device exhibited significant suppression of leakage currents, and good endurance (>300 cycles) and retention (>10^4 s). Further, the typical conduction mechanisms in Au/HZO/TiN RRAM device are also discussed.

2. Materials and methods

A 10 nm thick HZO film were then deposited on TIN/SiO_2/Si substrate by atomic layer deposition (ALD) at substrate temperature of 280 ℃ using $Hf[N(C_2H_5)CH_3]_4$ (TEMA–Hf), $Zr[N(C_2H_5)\ CH_3]_4$ (TEMA-Zr), and ozone as the Hf-precursor, Zr-precursor, and oxygen source, respectively. Because HfO_2 and ZrO_2 have an almost identical ALD growth rate, the HZO films were deposited with a 1:1 ALD cycle ratio. Further, a 50 nm thick Au top electrodes (TE) layer with an area of 100 × 100 μm^2 were deposited by physical vapor deposition followed by metal shadow mask. The schematic diagram of the Au/HZO/TiN RRAM device shown in **Figure 1a**. The electrical characterizations were measured by using semiconductor parameter analyzer (Agilent B1500A) with a room temperature. The measurements were carried out in a dc voltage sweep mode, with all basis voltages applied to the Au electrode while the TiN was grounded.

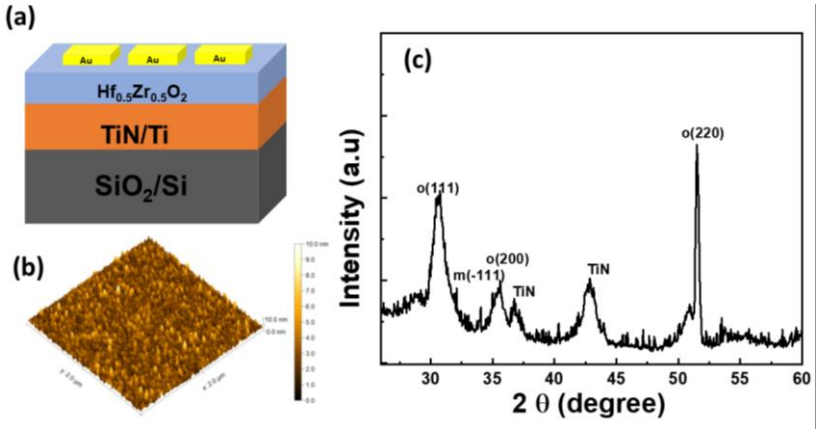

Figure 1. (a) Schematic view of the Au/HZO/TiN RRAM device; **(b)** AFM image of the HZO thin film; **(c)** X-ray diffraction pattern (XRD) analysis.

3. Results and discussions

Figure 1b shows the 3D AFM images of the scan area of 2 μm × 2 μm of HZO thin film. The surface morphology of the HZO thin film root-mean-square (RMS) values of 1.216 nm, which indicate that the thin film surface was uniformly deposited and smoothly. The thicknesses of HZO films control by ALD cycles have a noticeable

effect on the RMS roughness's of the thin films. **Figure 1c** shows the structural characterization of HZO films was investigated using the grazing incidence X-ray diffraction (GI-XRD). The HZO films displayed two crystalline structures: (1) m-phase with reflections of (111), and (–111); (2) o-phase with reflections of (111), (200) and (220). Note that o-phase phase in HZO is mainly responsible for the ferroelectric properties.

Figure 2a,**b** presents the typical current-voltage (*I-V*) characteristics of the Au/ HZO/TiN RRAM device structure. The *I-V* characteristics of RRAM device exhibited a clear resistive switching behaviour. The RRAM device displays an excellent resistive switching behaviour with a high on/off ratio of ~10^3. The resistive switching effect was evident since the SET process was detected at TE in the negative voltage directions whereas the RESET process was accomplished at TE with positive polarity. No forming process was necessary for activating the resistive switching effect. For the SET process, the negative voltage was swept in a sequence of 0 V→–3 V and –3 V→0 V. In the first positive bias from 0 V to –3 V, the current of the device increased steadily at –2.34 V for Au/HZO/TiN RRAM, while switching the resistance of device from HRS to LRS. In subsequent negative bias, the resistance change in the devices was retained, indicating non-volatile behaviour. The positive voltage was swept in a sequence of 0 V→3 V and 3 V→0 V for the RESET process. Interestingly, in positive forward bias at 2.72 V for Au/HZO/TiN, the current decreased sharply while the resistance of device switched from LRS to HRS. In subsequent positive bias, the resistance change was maintained throughout the sweep from 3 V to 0 V.

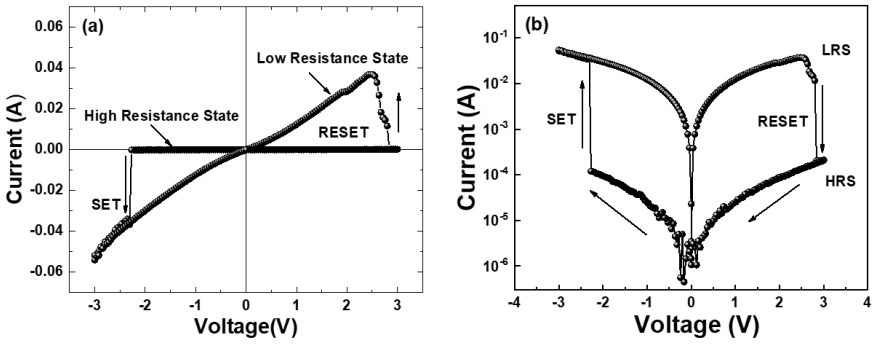

Figure 2. Current-voltage characteristics linear and logarithmic plots of the Au/HZO/TiN RRAM device.

In principle, reliability is an important index to evaluate the function of memory in application. In order to investigate the reliability of the Au/HZO/TiN RRAM devices, the endurance and the retention properties were presented in **Figure 3**. The endurance characteristics of the devices were performed under DC voltage sweeping mode, and the reading voltage was 0.5 V, as presented in **Figure 3a**. The plots clearly illustrate that the RRAM device demonstrate reliable endurance >300 cycles by maintaining a memory window 10^3. Further, the retention stability of the Au/HZO/TiN RRAM device was measured with a readout voltage of 0.1 V, as presented in **Figure 3b**. The retention characteristics of the Au/HZO/TiN RRAM device showed highly stable behaviour up to 10^3 seconds at +0.5 V without any noticeable degradation

Figure 3b. These findings suggest that the Au/HZO/TiN RRAM device has improved endurance and retention characteristics.

To understand the charge transport mechanism in the device, the double logarithmic of current voltage characteristics in both low resistance state and high resistance state is analyzed. **Figure 4a,b** show the positive bias and negative bias region of double logarithmic plots *I-V* characteristics of Au/HZO/TiN RRAM devices. The slope (S) of the curve is labeled by S_1, S_2, and S_3 was observed. In the low voltage region, the *I–V* characteristics exhibits ohmic conduction ($I \propto V$) with a S_1 ~1 due to the density of thermally generated free carriers is greater than the density of injected charge carriers [15,16]. In the HRS region, the device has a relatively high resistance, and the current flow is relatively small. At lower applied voltages, the current transport is not significantly affected by the resistive switching mechanism, and the conduction can be approximated as ohmic. Further, the values of S_2 increases to >2, such behavior follows from the relation ($I \propto V^2$) and is confirmed by the space charge limited conduction [17]. Finally, the LRS state shows the S_3 ~1 for Au/HZO/TiN devices, which due to ohmic conduction, indicating the linear behavior of the devices where current is proportional to the voltage is observed [18,19]. However, the Au/HZO/TiN device offers stability and improved migration of oxygen vacancies in the migration in the devices structure.

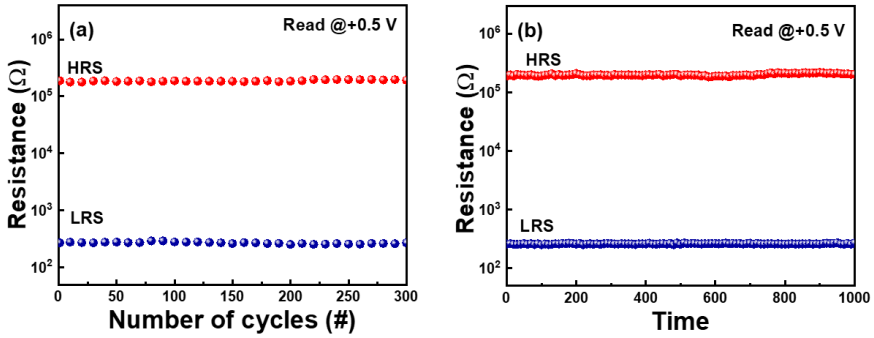

Figure 3. (a) Plot of the resistances of the device at HRS and LRS versus cycle number in the endurance characteristics of Au/HZO/TiN RRAM device; **(b)** Plot of the resistances of the device at HRS and LRS versus time in the retention characteristics time of Au/HZO/TiN RRAM device.

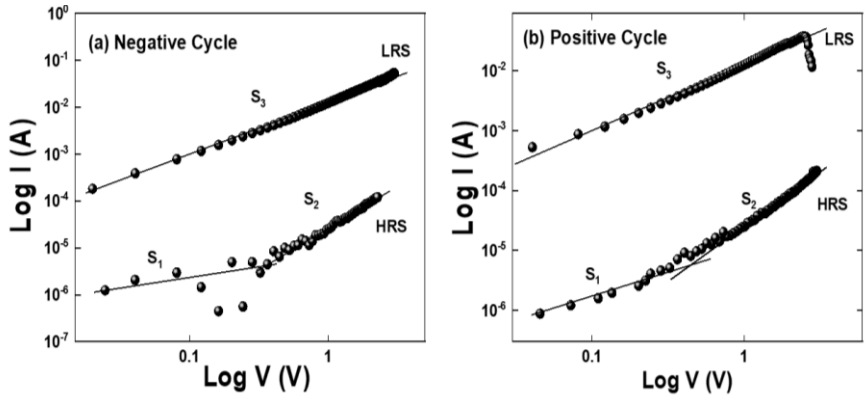

Figure 4. Double logarithmic plot of Au/HZO/TiN RRAM device **(a)** negative cycle and **(b)** positive cycle.

4. Conclusion

In this study, we fabricated and investigated the Au/HZO/TiN based random-access memory (RRAM) device. The RRAM devices showed the excellent stability and good reliability. As prepared device showed an excellent resistive switching behaviour with a high on/off ratio of ~10^3. The endurance test revealed that the devices can be stable for up to 300 cycles, and the retention test revealed that the resistance could be retained at HRS (or LRS) for up to 10^3 s with no fluctuation under a read voltage of 0.1 V. Further, the carrier transport mechanism has been investigated to explain the resistive switching characteristics of Au/HZO/TiN RRAM devices, which shows the LRS and HRS are consistent with the ohmic conduction and space charge limited conduction. This device is appropriate for use in future high-density non-volatile memory RRAM devices.

Conflict of interest: The author declares no conflict of interest.

References

1. Mahata C, Kang M, Kim S. Multi-Level Analog Resistive Switching Characteristics in Tri-Layer $HfO_2/Al_2O_3/HfO_2$ Based Memristor on ITO Electrode. Nanomaterials. 2020, 10(10): 2069. doi: 10.3390/nano10102069
2. Yingtao Li, Shibing Long, Manhong Zhang, et al. Resistive Switching Properties of Au/ZrO_2/Ag Structure for Low-Voltage Nonvolatile Memory Applications. IEEE Electron Device Letters. 2010, 31(2): 117-119. doi: 10.1109/led.2009.2036276
3. Napolean A, Sivamangai NM, Rajesh S, et al. Review on role of nanoscale HfO_2 switching material in resistive random access memory device. Emergent Materials. 2022, 5(2): 489-508. doi: 10.1007/s42247-022-00356-0
4. Lee SY, Chang J, Choi J, et al. Investigation of ultrathin Pt/ZrO_2–Al_2O_3–ZrO_2/TiN DRAM capacitors Schottky barrier height by internal photoemission spectroscopy. Current Applied Physics. 2017, 17(2): 267-271. doi: 10.1016/j.cap.2016.12.004
5. Wang ZJ, Bai Y. Resistive Switching Behavior in Ferroelectric Heterostructures. Small. 2019, 15(32). doi: 10.1002/smll.201805088
6. Kim S, Jeong HY, Choi SY, et al. Comprehensive modeling of resistive switching in the Al/TiOx/TiO_2/Al heterostructure based on space-charge-limited conduction. Applied Physics Letters. 2010, 97(3). doi: 10.1063/1.3467461
7. Wang Z, Wu H, Burr GW, et al. Resistive switching materials for information processing. Nature Reviews Materials. 2020, 5(3): 173-195. doi: 10.1038/s41578-019-0159-3
8. Ielmini D. Resistive switching memories based on metal oxides: mechanisms, reliability and scaling. Semiconductor Science and Technology. 2016, 31(6): 063002. doi: 10.1088/0268-1242/31/6/063002
9. Xiao Z, Kisslinger K, Chance S, et al. Comparison of Hafnium Dioxide and Zirconium Dioxide Grown by Plasma-Enhanced Atomic Layer Deposition for the Application of Electronic Materials. Crystals. 2020, 10(2): 136. doi: 10.3390/cryst10020136
10. Li Y, Long S, Lv H, et al. Improvement of resistive switching characteristics in ZrO_2 film by embedding a thin TiOxlayer. Nanotechnology. 2011, 22(25): 254028. doi: 10.1088/0957-4484/22/25/254028
11. Wu Z, Zhu J, Zhou Y, et al. Bipolar Resistive Switching Properties of $Hf_{0.5}Zr_{0.5}O_2$ Thin Film for Flexible Memory Applications. physica status solidi (a). 2017, 215(1). doi: 10.1002/pssa.201700396
12. Ryu SW, Cho S, Park J, et al. Effects of ZrO_2 doping on HfO_2 resistive switching memory characteristics. Applied Physics Letters. 2014, 105(7). doi: 10.1063/1.4893568
13. Huang CY, Huang CY, Tsai TL, et al. Switching mechanism of double forming process phenomenon in ZrOx/HfOy bilayer resistive switching memory structure with large endurance. Applied Physics Letters. 2014, 104(6). doi: 10.1063/1.4864396
14. Yan X, Xiao Z, Lu C. Characteristic investigation of highly oriented $Hf_{0.5}Zr_{0.5}O_2$ thin-film resistive memory devices. Applied Physics Letters. 2020, 116(1). doi: 10.1063/1.5141132
15. Sekhar Reddy PR, Janardhanam V, Rajagopal Reddy V, et al. Effects of Rapid Thermal Annealing on the Structural, Optical, and Electrical Properties of Au/CuPc/n-Si (MPS)-type Schottky Barrier Diodes. Applied Physics A. 2021, 127(10). doi: 10.1007/s00339-021-04945-4

16. Mikhaylov AN, Belov AI, Guseinov DV, et al. Bipolar resistive switching and charge transport in silicon oxide memristor. Materials Science and Engineering: B. 2015, 194: 48-54. doi: 10.1016/j.mseb.2014.12.029
17. Lim E, Ismail R. Conduction Mechanism of Valence Change Resistive Switching Memory: A Survey. Electronics. 2015, 4(3): 586-613. doi: 10.3390/electronics4030586
18. Yuan FY, Deng N, Shih CC, et al. Conduction Mechanism and Improved Endurance in HfO_2-Based RRAM with Nitridation Treatment. Nanoscale Research Letters. 2017, 12(1). doi: 10.1186/s11671-017-2330-3
19. Reddy PRS, Nallagatla VR, Kumar YA, et al. Enhanced resistive switching properties of HfAlOx/ZrO_2- based RRAM devices. Progress in Natural Science: Materials International. 2022, 32(5): 602-607. doi: 10.1016/j.pnsc.2022.09.013

Materials Technology Reports 2024, 2(1), 483.
https://doi.org/10.59400/mtr.v2i1.483

Article

Electrochemical performance of $Pr_{0.6}Sr_{0.4}Fe_{0.8}Co_{0.2}O_{3-\delta}$ as potential cathode material for IT-SOFC

M. Shamshi Hassan

Department of Chemistry, College of Science, Al-Baha University, Albaha 65799, Saudi Arabia; mshasan@bu.edu.sa

CITATION

Hassan MS. Electrochemical performance of $Pr_{0.6}Sr_{0.4}Fe_{0.8}Co_{0.2}O_{3-\delta}$ as potential cathode material for IT-SOFC. Materials Technology Reports. 2024; 2(1): 483. https://doi.org/10.59400/mtr.v2i1.483

ARTICLE INFO

Received: 3 November 2023
Accepted: 12 January 2024
Available online: 29 February 2024

Abstract: Solid oxide fuel cells (SOFCs) are renowned for being effective energy sources that have potential to influence how energy is developed in future. SOFCs operate at low temperatures provides different benefits for widespread commercialization. In the present study a perovskite material $Pr_{0.6}Sr_{0.4}Fe_{0.8}Co_{0.2}O_{3-\delta}$ (PSFCo) was investigated as cathode for SOFC in intermediate temperature range. Glycine nitrate process was used for the preparation of the samples. PSFCo exhibited cubic structure having small particle size (100–200 nm). The electrical conductivity of the PSFCo was measured as function of temperature up to 850 ℃. The sample displayed maximum electrical conductivity of 370 Scm^{-1} at around 550–600 ℃. The polarization behavior of PSFCo was calculated by means of AC impedance with $Sm_{0.8}Ce_{0.2}O_2$ (SDC) as electrolyte. The value of area specific resistance (ASR) was calculated as 0.146 Ωcm^2 at 800 ℃ and 0.248 Ωcm^2 at 700 ℃.

Keywords: cathode; PSFCo; electrical conductivity; impedance spectra; IT-SOFC

1. Introduction

The urgent need to minimize carbon emissions on a global scale and the quick depletion of fossil fuel supplies are driving up predicted demand for renewable energy sources. Fuel cells are energy-conversion systems that electrochemically combine fuel and oxidant to generate electricity and heat without the Carnot constraint [1–3]. Comparatively, SOFCs provide a variety of fuel sources, minimal noise, low CO_2 emissions, a long lifespan (40,000–80,000 h), and excellent conversion rate [4,5].

Typical SOFCs run at temperatures of about 1000 ℃. However, the high temperature causes a lot of issues, for example, the materials get damaged because of chemical and physical instability. Thus, there is a rather narrow options for the components that can be utilized in the construction and subsequent operation of SOFCs. If the working temperature were decreased, the affordable ferritic stainless steel can be utilized as connector, and the components' chemical, thermal, and physical durability would all be improved too [6]. For the effective launch of SOFC technology to the market, reduced temperature operation at 600–800 ℃ is an essential factor. These reduced temperature SOFC offer shorter start-up times, are more readily realistically designed, and are economically preferable. One of the vital challenge for low temperature operation is to nullify the stability problems while keeping a positive efficiency. Nevertheless, the electrolytes' ion conductivity will drop and the cathode resistance will rise at such a low operating temperature. Hence, ceria-based electrolyte, like gadolinia-doped ceria (GDC) or samarium-doped ceria (SDC), is normally used due to its improved ionic conductivity in decreased temperature range than yttria stabilized zirconia (YSZ) which is commonly utilized as electrolyte for high temperature SOFCs. But a significant problem with the lower operating temperature

is that the cathode's catalytic activity for oxygen reduction will decreased [7]. Thereby, it is crucial to find substitute materials, like perovskite cathodes, in order to guarantee the extremely stable and dependable operation of the resulting SOFCs, as well as practically acceptable performance. During past years adequate research investigation performed to ascertain appropriate material as cathode for application in SOFC that can work at intermediate temperature (500–800 ℃). Though, the electrode activity significantly declines as the operating temperature is lowered. The creation of high-performance cathode materials is essential for further enhancing fuel cell performance. Cathode is a significant part of the fuel cell which effectively determines the overall fuel cells performance. Among high performing cathodes, ABO_3 types are one of the best. The perovskite configuration (ABO_3) can be altered by exchanging A or B position positive ion by other elements. Praseodymium is one of the materials being utilized on A-site. The structural and electronic configuration of praseodymium resembles with other lanthanide elements like cerium and lanthanum [8]. Substituting lanthanum with smaller lanthanide has been reported to show better performance as cathode material [9,10]. Previous reports have shown that the exchange of La by Pr improves the conductivity and catalytic activity [11–13]. Strontium doped praseodymium cobaltite or manganites have been stated to show excellent electrical, ionic conductivity and overpotential values [14–20]. Doping cobalt by substituting iron on B-site of the ABO_3 type have been shown to exhibit effective performance as cathode material [21–24].

In this study, a new type of perovskite oxide was developed for the cathode of IT-SOFCs by doping Sr at the A site and Co at the B site of the $PrFeO_{3-\delta}$-based perovskite material. Even after doping of the elements on A and B-site in compound, it did not change its cubic structure and it remain stable even at high temperature without any impurity. The cathode materials are designed to improve the cathode performance at intermediate temperatures. PSFCo has shown promising electrical properties and low value of area specific resistance at IT-SOFCs.

2. Experimental

$Pr_{0.6}Sr_{0.4}Fe_{0.8}Co_{0.2}O_3$ powder was synthesized by glycine nitrate method reported elsewhere [25]. Analytical grade $Pr(NO_3)_3.6H_2O$ (Alfa Aesar, 99.9%), $Sr(NO_3)_2$ (Aldrich, 99%), $Fe(NO_3)_3.9H_2O$ (Samchun chemicals, 98.5%) and $Co(NO_3)_2.6H_2O$ (Alfa Aesar, 98%) were used. Glycine was used as oxidizer and fuel. The stoichiometric amounts of all the metal nitrates were mixed with DW (250 mL) in beaker. After dissolution, double mole of glycine (compare to metal nitrate) was added in the same solution. Solution was kept stirring and the hot plate temperature were increased to 200 ℃. Gradually, the viscosity of the solution increases with times which lead to combustion reaction leaving dark grey ash in beaker. The sample was collected and heated at different temperature under air to burn off carbon. The sample powder was hard-pressed into pallet and calcined at 1200 ℃ for 5 h.

To determine the crystallinity of synthesized material, X-ray diffraction (XRD, Rigaku) study was performed by Rigaku D/Max diffractometer with Cu Kα radiation. Chemical composition of PSFCo was observed by Energy Dispersive X-ray (EDX, JEOL JSM6700) spectroscopy. The study of microstructures of synthesized samples

was executed by Scanning Electron Microscopy (SEM, JEOL JSM6700) and Transmission Electron Microscopy (TEM, Hitachi H-7650). Electrical conductivity of the PSFeCo material was calculated using the standard 4 probe DC method. The $Ce_{0.8}Sm_{0.2}O_2$ (SDC) electrolyte sample was also synthesized by the same glycine nitrate method. This electrolyte powder was pressed into round pallets (15 mm in diameter) and calcined at 1450 °C for 5 h in furnace. The electrochemical properties and AC impedance were measured by impedance analyzer (VersaSTAT 4).

3. Result and discussion

The X-ray pattern of the PSFCo samples is shown in **Figure 1a** calcined at various temperatures. XRD results showed a single-phased powder with perovskite-type cubic structure (Pm-3m space group) similar to that of $Pr_{1-x}Sr_xFeO_3$, is formed [26]. As the temperature increases, the spectral peaks became sharper showing higher crystallinity without detectable impurity phases. EDX result of prepared PSFCo material was shown in **Figure 1b**. From the attained EDX outcomes, it is obvious that the produced $Pr_{0.6}Sr_{0.4}Fe_{0.8}Co_{0.2}O_{3-\delta}$ material contains only Pr, Sr, Fe, Co and O elements with no contamination. **Figure 1c,d** depicts the SEM image PSFCo cathode synthesized at 1000 °C and cross-section view of PSFCo/SDC interface. The microstructure looks to be consistent with well necked granules and high porosity (**Figure 1c**). The electrode microstructure showed uniform and uneven attachment with electrolyte. The coating of PSFCo cathode on 1mm thick SDC electrolyte seems to be intact. The electrolyte layers exhibit compressed micro-structure devoid of cracks and pinholes. The thickness of electrode on electrolyte is about 35 μm (**Figure 1d**).

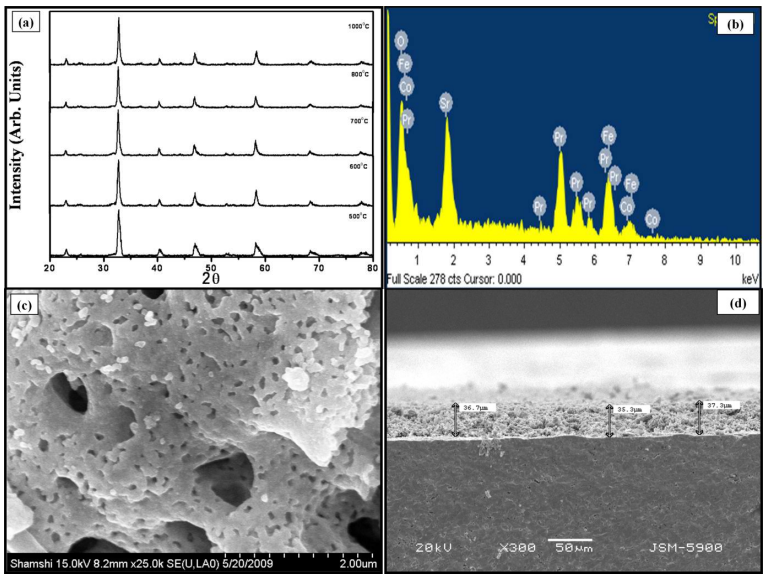

Figure 1. (a) the XRD spectra of the $Pr_{0.6}Sr_{0.4}Fe_{0.8}Co_{0.2}O_{3-\delta}$ samples at 500, 600, 700, 800 and 1000 °C; **(b)** EDX spectrum; **(c)** SEM images of $Pr_{0.6}Sr_{0.4}Fe_{0.8}Co_{0.2}O_{3-\delta}$ powder synthesized at 1000 °C; and **(d)** cross-section view of SDC-PSFCo interface.

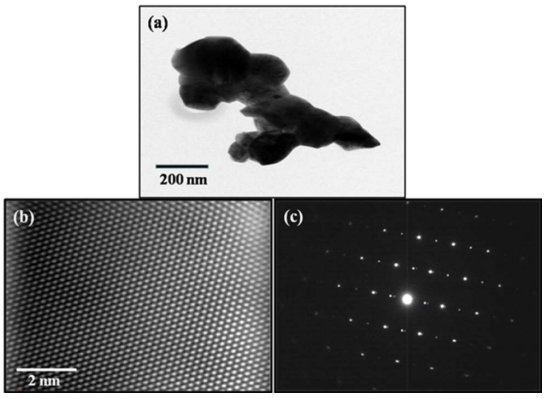

Figure 2. (a) TEM; **(b)** HR-TEM; and **(c)** SAED pattern of $Pr_{0.6}Sr_{0.4}Fe_{0.8}Co_{0.2}O_{3-\delta}$ particle.

Figure 2a,b demonstrates the TEM and HRTEM of the primed material whereas **Figure 2c** characterizes the selected area electron diffraction pattern (SAED). The TEM result showed the agglomerated particles showing size in between 100 to 200 nm. HR-TEM reveals the high crystallinity of the material, the atomic planes are parallel and have regular arrangement of atoms. Additionally, the SAED pattern reveals high standard of crystallinity. Lattice planes have no disorders or defects revealing high crystallinity of material.

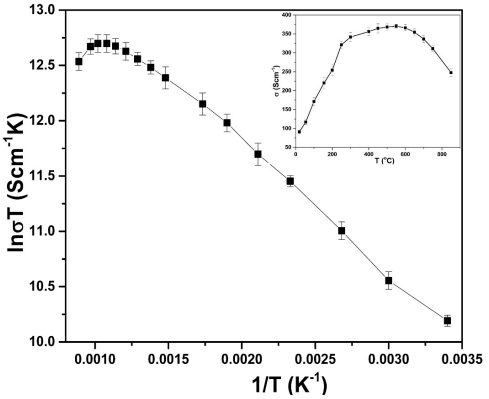

Figure 3. Arrhenius plot of DC conductivity (lnσT) vs. 1/T. Inset shows the electrical conductivity for $Pr_{0.6}Sr_{0.4}Fe_{0.8}Co_{0.2}O_{3-\delta}$. pallet measured from room temperature to 850 ℃.

Electrical conductivity of the cathode pellet was measured as function of inverse temperature in **Figure 3**. The simultaneous presence of oxygen vacancies and electron holes in perovskite-type materials results in both ionic and electronic conductivities; nevertheless, the ionic conductivity of the material is far less than the electronic conductivity. Synthesized sample showed the semiconducting behavior, as the electrical conductivity increase with increase in temperature through a maximum, then declined at elevated temperature representing that a dissimilar mechanism of conduction takes place at diverse temperature. The sample displayed maximum conductivity of 370 Scm^{-1} at around 550–600 and it remain more than 200 Scm^{-1} even at 850 ℃ (**Figure 3**). After linear fitting from graph, the estimate of activation energy was calculated as 8.6 $KJmol^{-1}$. The high value of conductivity is owing to the increase

in concentration of B^{+4} cations (Fe^{+4}or Co^{+4}). The conductivity decrease at high temperature can be ascribe to appearance of oxygen vacancies along with reduction of B^{+4} to B^{+3} (Fe^{+3} or Co^{+3}) which leads to decrease in charge carrier concentration. Furthermore, a reduction in iron ions impacts the electron transport between Fe–O–Fe bonds, resulting in a decline in electronic conductivity. This decline has the greatest influence on the total electrical conductivity [27].

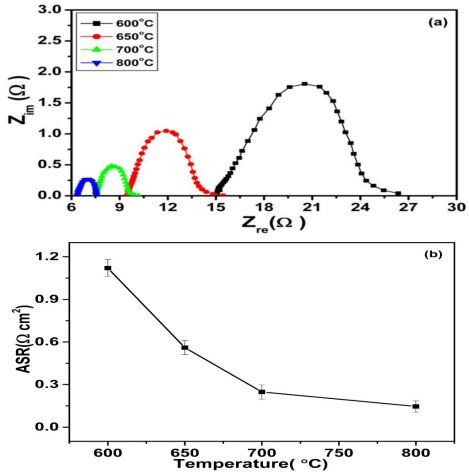

Figure 4. (a) impedance spectra for $Pr_{0.6}Sr_{0.4}Fe_{0.8}Co_{0.2}O_{3-\delta}$ cathode in air at various temperature; **(b)** area specific resistance (ASR) of the PSFC measured at different temperature.

The typical impedance for symmetrical cells PSFCo/SDC/PSFCo at various temperatures (600, 650, 700 and 800 °C) are revealed in **Figure 4**. Herein, it is noticed that electrode polarization resistance (P_R) of PSFCo cathode on SDC electrolyte increased with temperature (**Figure 4a**). This phenomena possibly attributed to increase in number of oxygen ion vacancy on the cathode surface which helps in oxygen molecule $O_{2(ad)}$ dissociation to oxygen atom $O_{(ad)}$ [28]. The value of ASR (Ωcm^2) as a parameter of temperature for PSFCo cathode in air is shown in inset in **Figure 4b**. The ASR decreases as temperature increases from 1.21 Ωcm^2 at 600 °C, 0.56 Ωcm^2 at 650 °C, 0.248 Ωcm^2 at 700 °C to 0.146 Ωcm^2 at 800 °C. ASR signifies the overall cathodic features assigned to oxygen reduction, oxygen surface/bulk diffusion and gas-phase oxygen diffusion [29]. This indicates that PSFCo cathode has elevated electrocatalytic performance for oxygen reduction reactions at reduced temperatures. Thus, we can say that PSFCo cathode can be a promising and good material for application in IT-SOFC.

4. Conclusion

$Pr_{0.6}Sr_{0.4}Fe_{0.8}Co_{0.2}O_{3-\delta}$ cathode was successfully prepared by glycine nitrate method and characterized by physico-chemical properties. It's electrical and electrochemical properties was also investigated for potential usage as cathode material for IT-SOFC. The sample features cubic structure with 100–200 nm sized particle. XRD results showed a single-phased powder with perovskite-type cubic structure. The sample displayed the semiconductor to metal conduction transition with maximum conductivity of 370 Scm^{-1} at around 550–600 °C. Therefore, they may be

use as a potential cathode in IT-SOFC. The ASR value of symmetrical PSFC cathode in air were 1.21 Ωcm^2, 0.56 Ωcm^2, 0.248 Ωcm^2 and 0.146 Ωcm^2 at 600 ℃, 650 ℃, 700 ℃ and 800 ℃ respectively. The PSFCo cathode has demonstrated promising catalytic activity for oxygen reduction. Hence, we can conclude that PSFCo can be a cheap, efficient, stable, and promising material to use as cathode at intermediate temperature in SOFC. Further investigation is required to evaluate the long-term stability and chemical compatibility on this material.

Conflict of interest: The author declares no conflict of interest.

References

1. Richter J, Holtappels P, Graule T, et al. Materials design for perovskite SOFC cathodes. Monatshefte für Chemie—Chemical Monthly. 2009; 140(9): 985-999. doi: 10.1007/s00706-009-0153-3
2. Choudhury R, Das UJ, Ceruti A, et al. Visco-elastic effects on the three dimensional hydrodynamic flow past a vertical porous plate. Int. Inf. Eng. Technol. Assoc. 2013; 31: 1-8.
3. Ashrafi H, Pourmahmoud N, Mirzaee I, et al. Performance improvement of proton-exchange membrane fuel cells through different gas injection channel geometries. International Journal of Energy Research. 2022; 46(7): 8781-8792. doi: 10.1002/er.7755
4. Gao Y, Zhang M, Fu M, et al. A comprehensive review of recent progresses in cathode materials for Proton-conducting SOFCs. Energy Reviews. 2023; 2(3): 100038. doi: 10.1016/j.enrev.2023.100038
5. Cigolotti V, Genovese M, Fragiacomo P. Comprehensive Review on Fuel Cell Technology for Stationary Applications as Sustainable and Efficient Poly-Generation Energy Systems. Energies. 2021; 14(16): 4963. doi: 10.3390/en14164963
6. Li H, Wang Y, Liu H, et al. Interaction between SOFCs interconnect Cr-free multicomponent spinel coating materials and chromia. International Journal of Hydrogen Energy. 2023; 48(81): 31700-31707. doi: 10.1016/j.ijhydene.2023.04.324
7. Colomer MT, Steele BCH, Kilner JA. Structural and electrochemical properties of the $Sr_{0.8}Ce_{0.1}Fe_{0.7}Co_{0.3}O_{3-\delta}$ perovskite as cathode material for ITSOFCs. Solid State Ionics. 2002; 147(1-2): 41-48.
8. Ran R, Wu X, Quan C, et al. Effect of strontium and cerium doping on the structural and catalytic properties of PrMnO oxides. Solid State Ionics. 2005; 176(9-10): 965-971. doi: 10.1016/j.ssi.2004.11.018
9. Riza F, Ftikos C, Tietz F, Fischer W. Preparation and Characterization of $Ln_{0.8}Sr_{0.2}Fe_{0.8}Co_{0.2}O_3$−x(Ln= La, Pr, Nd, Sm, Eu, Gd). Journal of the European Ceramic Society. 2001; 21: 1769-1773.
10. Qiu L, Ichikawa T, Hirano A, et al. Ln1−xSrxCo1−yFeyO3−δ (Ln = Pr, Nd, Gd; x = 0.2, 0.3) for the electrodes of solid oxide fuel cells. Solid State Ionics. 2003; 158: 55-65.
11. Ishihara T, Kudo T, Matsuda H, et al. Doped PrMnO3 Perovskite Oxide as a New Cathode of Solid Oxide Fuel Cells for Low Temperature Operation. Journal of The Electrochemical Society. 1995; 142(5): 1519-1524. doi: 10.1149/1.2048606
12. Ishihara T, Honda M, Shibayama T, et al. Intermediate Temperature Solid Oxide Fuel Cells Using a New LaGaO3 Based Oxide Ion Conductor: I. Doped as a New Cathode Material. Journal of The Electrochemical Society. 1998; 145(9): 3177-3183. doi: 10.1149/1.1838783
13. Kostogloudis GC, Vasilakos N, Ftikos C. Crystal structure, thermal and electrical properties of Pr1−xSrxCoO3−δ (x = 0, 0.15, 0.3, 0.4, 0.5) perovskite oxides. Solid State Ionics. 1998; 106: 207-218.
14. Steele BC, Bae JM. Properties of $La_{0.6}Sr_{0.4}Co_{0.2}Fe_{0.8}O_{3-x}$ (LSCF) double layer cathodes on gadolinium-doped cerium oxide (CGO) electrolytes: II. Role of oxygen exchange and diffusion. Solid State Ionics. 1998; 106: 255-261.
15. Xia C, Rauch W, Chen F, Liu M. $Sm_{0.5}Sr_{0.5}CoO_3$ cathodes for low-temperature SOFCs. Solid State Ionics. 2002; 149: 11-19.
16. Al Daroukh M, Vashook V, Ullmann H, et al. Oxides of the AMO3 and A2MO4-type: structural stability, electrical conductivity and thermal expansion. Solid State Ionics. 2003; 158: 141-150.
17. Wang Y, Wang S, Wang Z, et al. Performance of Ba0.5Sr0.5Co0.8Fe0.2O3−δ-CGO-Ag cathode for IT-SOFCs. Journal of Alloys and Compounds. 2007; 428(1-2): 286-289. doi: 10.1016/j.jallcom.2006.02.071
18. Chen W, Wen T, Nie H, Zheng R. Study of Ln0.6Sr0.4Co0.8Mn0.2O3-δ (Ln = La, Gd, Sm or Nd) as the cathode materials for intermediate temperature SOFC. Materials research bulletin. 2003; 38: 1319-1328.
19. Rossignol C, Ralph J, Bae JM, Vaughey J. Ln1−xSrxCoO3 (Ln = Gd, Pr) as a cathode for intermediate-temperature solid

oxide fuel cells. Solid State Ionics. 2004; 175: 59-61.
20. Kim JH, Baek SW, Lee C, et al. Performance analysis of cobalt-based cathode materials for solid oxide fuel cell. Solid State Ionics. 2008; 179(27-32): 1490-1496. doi: 10.1016/j.ssi.2008.01.086
21. Tai LW, Nasrallah M, Anderson H, et al. Structure and electrical properties of La1−xSrxCo1−yFeyO3. Part 1. The system La0.8Sr0.2Co1−yFeyO3. Solid State Ionics. 1995; 76: 259-271.
22. Chen X, Wu N, Ignatiev A. Structure and conducting properties of La1-xSrxCoO3-δ films. Journal of the European Ceramic Society. 1999; 19: 819-822. doi: 10.1016/S0955-2219(98)00323-9
23. Chen X, Wu NJ, Smith L, et al. Thin-film heterostructure solid oxide fuel cells. Applied Physics Letters. 2004; 84(14): 2700-2702. doi: 10.1063/1.1697623
24. Pederson LR, Singh P, Zhou XD. Application of vacuum deposition methods to solid oxide fuel cells. Vacuum. 2006; 80(10): 1066-1083. doi: 10.1016/j.vacuum.2006.01.072
25. Zamani F, Taghvaei AH. Characterization and magnetic properties of nanocrystalline Mg1-CdFe2O4 (x= 0.0–0.8) ferrites synthesized by glycine-nitrate autocombustion method. Ceramics International. 2018; 44(14): 17209-17217. doi: 10.1016/j.ceramint.2018.06.178
26. Piao J, Sun K, Zhang N, et al. Preparation and characterization of Pr1−xSrxFeO3 cathode material for intermediate temperature solid oxide fuel cells. Journal of Power Sources. 2007; 172(2): 633-640. doi: 10.1016/j.jpowsour.2007.05.023
27. Gou Y, Li G, Ren R, et al. Pr-Doping Motivating the Phase Transformation of the BaFeO3-δ Perovskite as a High-Performance Solid Oxide Fuel Cell Cathode. ACS Applied Materials & Interfaces. 2021; 13(17): 20174-20184. doi: 10.1021/acsami.1c03514
28. Steele BC. Survey of materials selection for ceramic fuel cells II. Cathodes and anodes. Solid State Ionics. 1996; 86: 1223-1234.
29. Aysal HE, Kılıç F, Çakmak G, et al. Thermal plasma synthesis of (La,Sr)CoO3-(La,Sr)2CoO4 composite cathodes for intermediate temperature solid oxide fuel cells (IT-SOFC). International Journal of Hydrogen Energy. 2024; 51: 1477-1486. doi: 10.1016/j.ijhydene.2023.07.031

Materials Technology Reports 2024, 2(1), 1603.
https://doi.org/10.59400/mtr.v2i1.1603

Article

Performance assessment of particle board developed from organic wastes using polymer matrix

Joseph Abutu[1,*], Tsotsi Rikwen Tsoji[1], Areo Stephen[2], Aliyuda Dedan Araye[1], Sunday Albert Lawal[3], Ayuba Kitaka Rimamtaatang[1]

[1] Department of Mechanical Engineering, Taraba State University, Jalingo 660213, Nigeria
[2] National Examination Council, Minna 920101, Nigeria
[3] Department of Mechanical Engineering, Federal University of Technology, Minna 920101, Nigeria
*** Corresponding author:** Joseph Abutu, abutu.joseph@tsuniversity.edu.ng

CITATION

Abutu J, Tsoji TR, Stephen A, et al. Performance assessment of particle board from organic wastes using polymer matrix. Materials Technology Reports. 2024; 2(1): 1603.
https://doi.org/10.59400/mtr.v2i1.1603

ARTICLE INFO

Received: 14 April 2024
Accepted: 27 May 2024
Available online: 15 June 2024

Abstract: In this work, sugarcane bagasse and rice husk were used as filler material for the production of agro-based particle board along with low-density polyethylene and coconut shell, with the aim of investigating the effects of varying compositions of constituents on the performance of the developed composite using constant process parameters of moulding pressure (10 MPa), moulding temperature (140 °C), curing time (10 min) and heat treatment time (1 h). Experimental design was conducted using box-Behnken design (L1533) while multi-response optimization was carried out using grey relational analysis (GRA). The experimental results revealed that changes in percentage composition affect the performance of the composite, and the multi-response optimal performance of the developed bagasse-based particle board (BPB) and rice husk-based particle board (RPB) can be achieved with bagasse or rice husk (30 wt%), coconut shell (30 wt%), and low-density polyethylene (40 wt%). The results of the analysis of variance showed that the performance of the two particle boards is most influenced by the presence of low-density polyethylene (LDPE). Finally, compared to rice husk, bagasse can effectively serve as a preferred substitute for wood in the production of particle board.

Keywords: bagasse; rice husk; coconut shell; LDPE; GRA; particle board

1. Introduction

Particle boards are often regarded as boards produced from lingo-cellulosic materials such as wood and bonded together by resins or other adhesives [1]. These composites are often utilised in structural applications such as furniture, partitioning, ceiling boards, wall bracing, cladding, and flooring. Most of these particle boards in existence are produced from wasted wood materials, thereby conserving our natural resources [2]. Saeed et al. [3] have revealed that lignocellulosic materials, derived from agro-wastes, are vital resources comprising cellulose, lignin, and hemicellulose, which can be classified into non-wood and wood. Non-wood consists of sugarcane bagasse, coconut shells [4], rice husks [3], and pineapple leaves [5], while wood consists of softwood and hardwood [6]. Though, most recently, non-wood materials are gaining dominance as a result of global fibre demand and scarcity of trees. This is attributed to their ease of processing and short growth cycles [7]. However, with an increase in the global population and advances in technology, the demand for wood in the forest industry has grown over the years, thereby leading to an increase in deforestation, which negatively affects global climate change [8,9]. Ganaie et al. [10] have revealed that global population growth is increasing the demand for wood for

construction and increasing its price. This massive demand has resulted in the application of wood in new areas and has similarly led to a significant pressure on the existing forest resources [11,12]. Though the need to reduce the overdependence on forest resources and wood coupled with the demand for an improved particle board using agro-wastes has prompted a huge interest in the utilization of agricultural wastes and residues for the production of particle board [13]. These alternative materials can play a growing tendency and major role in providing alternatives for particle board industries. Several authors have ultilised different agro-waste materials with the aim of finding a suitable replacement for wood products and obtaining particle board with desirable properties such as high density, better mechanical properties, abrasion resistance, high durability, low water absorption, and thickness swell rate [3,14].

Auriga et al. [15] investigated the effect of the addition Tetra Pak waste material in the core layer on the performance of particle board. The authors revealed that Tetra Pak does not significantly affect the modulus of elasticity and static bending strength of the particleboard but significantly decreases tensile strength. Acda and Cabangon [16] investigated the mechanical and physical properties as well as termite resistance of particleboard developed from a mixture of wood particles and waste tobacco stalk. It was found that the presence of residual nicotine is responsible for termite resistance of particleboard containing tobacco stalk. Hence, authors revealed that tobacco stalk can be used as an alternative material for wood particles in the manufacture of particleboard. Atoyebi et al. [17] developed particle boards from coconut shell, palm kernel shell, and coconut husk in different compositions of urea formaldehyde binder varying from 25%, 30%, 35%, 40%, and 50%. The authors revealed that particle boards composed of 25% palm kernel shell, 50% coconut shell, and 25% coconut husk have the most preferable properties. Kenaf fibers have also been used by Xu et al. [18], Paridah et al. [19], and Juliana et al. [20] for the production of particle board using similar experimental design techniques (trial and error). The results provided by the different authors provided evidence that combining kenaf fiber particles with other materials leads to better mechanical and physical properties of particle boards. Also, bagasse and timber mixture from industrial waste [21], Roselle tree stem [22], Jatropha Curcas wood waste [23], hazelnut husk [24], and pepper stalks [25] are some of the agro-wastes that have been used for the production of particle boards.

Over the years, natural fibers such as bagasse have been under-utilized and their disposal has posed a major environmental concern for Africans, especially people leaving in the northern parts of Nigeria [26]. Akshaya et al. [27] have revealed that bagasse is a lingo-cellulosic material providing an abundant and renewable energy source and consists of approximately 50% cellulose and 25% each of hemicellulose and lignin. Also, Salmah [28] reported that coconut shell (lignocellulosic filler) exhibits better properties compared to mineral fillers (kaolin, mica, $CaCO_3$ and talc). Some of the outstanding properties reported by Salmah [28] include minimal health hazards, a high specific strength-to-weight ratio, low cost, biodegradability, being environmentally friendly, and renewability. In addition, rice husk (RH) is known to be an inexpensive byproduct of rice processing. Many researchers have revealed that rice husk can be utilized as filler material in rice husk-filled polymeric composites. Therefore, in this study, bagasse, coconut shells, and rice husk were used as filler materials in the production of particle board composites using low-density

polyethylene (empty water sachet) wastes as binder and adopting box Behnken design (BBD) and Julong's grey relational analysis (GRA) as experimental design and multi-response optimization technique, respectively.

2. Materials and methods

2.1. Materials

Bagasse (**Figure 1a**), coconut shells (**Figure 1b),** and rice husk (**Figure 1c**) were utilized separately as filler materials, while low-density polyethylene (empty water sachet) wastes (**Figure 2**) were used as binder. Bagasse was locally sourced from Savanna Sugar Company, Numan, Nigeria; coconut shells were sourced from a coconut trader in Jalingo, Nigeria; and rice husk was obtained from a local rice milling factory in Jalingo, Nigeria. Also, the empty water sachet wastes were picked from the main campus of Taraba State University, Jalingo, Taraba State.

(a) **(b)** **(c)**

Figure 1. Filler materials: **(a)** sugarcane bagasses; **(b)** coconut shells; **(c)** rice husk.

Figure 2. Low density polyethylene (sachet water) wastes.

2.2. Methods

This research was carried out in three stages; the first stage involved the preparation of the locally sourced bagasse, coconut shells, and rice husk using distilled water and sodium hydroxide. The second stage involved the production and characterization of particle boards developed separately from bagasse and rice husk using low-density polyethylene binder and coconut shells via box Behnken design (BBD), and the final stage involved the analysis of the experimental data using a single response (signal to noise ratios) and multi-response (grey relational analysis) optimization technique.

2.2.1. Material preparation

The locally sourced rice husk and bagasses were immersed in sodium chloride (NaCl) solution for treatment and thereafter dried under the sun for 5 days to remove the moisture content. The dried sugarcane bagasses were then crushed using a blender to produce short, needle-like fibers. Also, the preparation of the coconut shells involved washing of shells with soap (sodium sulfonate) and cleaning using dried cloth, drying in a hot air oven (150 °C), followed by crushing using a pestle and mortar as well as grinding with a grinding machine. The blended bagasse, coconut shell powder, and rice husks were then sieved using a sieve size 425 µm. In addition, the empty water sachet wastes made of low-density polyethylene (LDPE) were also picked, sorted, and washed thoroughly to remove debris and dirt that may stand as impurities. The sachet water wastes were then dried under the sun for 5 days to remove retained moisture on the sachet. Thereafter, the dried sachets were cut into smaller pieces for easy compounding and then measured accordingly. The methods of preparation of the different materials are presented in **Figure 3**.

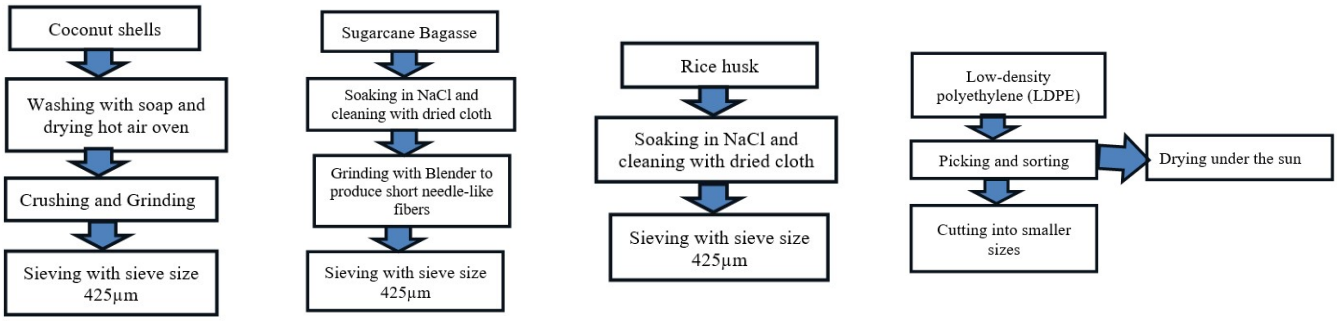

Figure 3. Methods of preparation of **(a)** coconut shells; **(b)** sugarcane bagasse; **(c)** rice husk; **(d)** LDPE.

2.2.2. Experimental design

Experimental design was carried out in accordance with box Behnken-response surface methodology $L_{15}(3)^3$ design using Minitab 19 statistical software. A varying composition (control factors) of reinforcement (bagasse or rice husk), LDPE, and a constant coconut shell powder was used to investigate the effects of composition on the performance of the developed composite. Constant process parameters of moulding pressure (10 MPa), moulding temperature (140 °C), curing time (10 min), and heat treatment time (1 h) were also used in this study. The factor levels of the control factors utilised in the work are shown in **Table 1**, while the box Behnken's design (BBD) matrix consisting of the coded and experimental matrix was obtained using Minitab 19 statistical software and shown in **Table 2**. The factor levels presented in **Table 1** are selected based on the volume size of the mould and recommendations by other authors stipulated in literature [17,29]. Also, Lekshmi et al. [30] recommended equal composition for binder (low density polyethylene) and reinforcement (rice husk and bagasse). Hence, similar factor levels (150 = 350 g) were adopted for the two control factors in this study. In addition, the mass of the coconut shells was held constant throughout. The total weight utilized was 150 g, as adopted by Suleiman et al. [31].

Table 1. Factor levels of control factors.

Control factors	Unit	Level 1	Level 2	Level 3
Low density polyethylene	Gram	150	250	350
Reinforcement (*R*)	Gram	150	250	350
Coconut shell (CCS)	Gram	150	150	150

Table 2. Coded and experimental design matrix.

Sample number	Coded matrix			Experimental matrix (grams)			Experimental matrix (%)		
	R	**CCS**	**LDPE**	**Ba/Rh**	**CCS**	**LPD**	***R***	**CCS**	**LDPE**
1	−1	−1	0	150	150	150	33.3	33.3	33.3
2	1	−1	0	350	150	150	53.8	23.1	23.1
3	−1	1	0	150	150	150	33.3	33.3	33.3
4	1	1	0	350	150	150	53.8	23.1	23.1
5	−1	0	−1	150	150	100	37.5	37.5	25.0
6	1	0	−1	350	150	100	58.3	25.0	16.7
7	−1	0	1	150	150	200	30.0	30.0	40.0
8	1	0	1	350	150	200	50.0	21.4	28.6
9	0	−1	−1	250	150	100	50.0	30.0	20.0
10	0	1	−1	250	150	100	50.0	30.0	20.0
11	0	−1	1	250	150	200	41.7	25.0	33.3
12	0	1	1	250	150	200	41.7	25.0	33.3
13	0	0	0	250	150	150	45.5	27.3	27.3
14	0	0	0	250	150	150	45.5	27.3	27.3
15	0	0	0	250	150	150	45.5	27.3	27.3

2.2.3. Production processes

Two sets of particle boards were produced using bagasse and rice husk separately as reinforcement materials, and coconut shell was used as filler particles. The sieved bagasse, or rice husk, coconut shell, as well as the LDPE, was measured as specified for each composition presented in **Table 2**. For each run, a two-roll mill situated at the polymer workshop of the Nigerian Institute for Leather and Science Technology (NILEST), Samaru, Zaria-Nigeria, was used to blend the mixture in order to form the composite. The compounded mixture was thereafter removed and placed in a square mould of dimensions 150 × 100 × 30 mm for hot pressing in order to increase its compatibility. The hot-pressing process was carried out using a compression moulding machine (Model: 0577-86365889, Wenzhou Zhiguang Shoe Machine Co. Ltd.) situated at the polymer workshop of the Nigerian Institute for Leather and Science Technology (NILEST), Samaru, Zaria, Nigeria. and constant coconut shell powder and process parameters (moulding pressure—10 MPa, moulding temperature—140 °C, and curing time—10 min) were used throughout the compression moulding process. At the end of the compression moulding cycle, the boards were removed and subjected to heat treatment for 1 h using a hot air oven operating at a temperature of 120 °C. The same procedure was used for the production of the other fourteen (14) samples. The developed bagasse and rice husk-based reinforced particle boards are

presented in **Figures 4** and **5**, respectively. Samples 1–4 and samples 13–15 shown in **Figures 4** and **5** contain 150 g of LDPE, while samples 10–15 constitute 250 g of sugarcane bagasse (**Figure 4**) and rice husk (**Figure 5**). Other samples shown in **Figures 4** and **5** contain 150 g of coconut shall and were produced in accordance with the experimental design matrix presented in **Table 2**.

Figure 4. Bagasse-based reinforced particle board.

Figure 5. Rice husk-based reinforced particle board.

2.2.4. Sample characterization

The developed particle board samples were characterized by investigating the performance (tensile strength, impact energy, hardness, thickness swell, and water absorption). The tensile strength, impact energy, and hardness of the board were studied using standard testing procedures specified by ASTM D638, ASTM E23-04, and ASTM E384, respectively, while thickness swell and water absorption were studied using standard testing procedures specified by ASTM D570. Hardness test samples were prepared to 40 × 40 × 20 mm dimension, and the test was carried out using a Vicker's hardness tester (Model: MV1-PC, Serial No: 07/2012-1329) with a load of 0.3 kg by setting the machine to a maximum and minimum limit of 120 and 020 HV. As recommended by ASTM E384, hardness tests were conducted using a loading force of 0.3 kg, and the hardness was determined by the penetration depth of the indenter under the applied load. At least three readings of each measured point

were taken. Also, specimens for the tensile test were prepared in accordance with standard ASTM D638 (ASTM International 2004-Dumbell shape) for each sample using a universal testing machine (INSTRON; 6800 series, Max: 50 kN) and executed at room temperature. Three specimens from each sample were prepared in accordance with the specified ASTM standards, and the average value of the results was thereafter recorded. In addition, the specimen for the impact test was prepared to 20 × 20 × 10 mm in accordance with ASTM E23-04 guidelines. This procedure involved placing the V-notched specimen across the parallel jaws of the impact testing machine in the Charpy mode, after which the pointer was set to an initial energy of 0 J and thereafter, releasing the pendulum hammer downward towards the specimen. The energy absorbed, which causes the fractured surfaces, was then recorded. Three test specimens prepared from each sample were tested and the average values recorded. Also, specimens for the water absorption and thickness swell test were prepared in accordance with the procedure outlined by ASTM D570, which stipulates a specimen size of 20 × 20 × 3 mm prepared from each sample. Ten specimens of each sample were prepared and dried in an oven for 24 h at 50 ℃. The samples were thereafter removed and allowed to cool. Specimens for thickness swell and water absorption tests were afterward immersed in distilled water for 3 days. The water absorption and thickness swell of each sample will be calculated using Equations (1) and (2), respectively [32].

$$\text{Water absorption (Wa)} = \frac{W_1 - W_0}{W_0} \times 100 \quad (1)$$

$$\text{Thickness swell (Ts)} = \frac{T_1 - T_0}{T_0} \times 100 \quad (2)$$

W_1 and W_0 = weight of specimen after and before immersion in distilled water; T_1 and T_0 = Thickness of specimen after and before immersion in distilled water; Theoretically, ultimate tensile strength and impact strength can be calculated using Equations (3) and (4) respectively [33].

$$\text{Ultimate tensile strength (UTS)} = \frac{P_{\max}}{A_0} \quad (3)$$

where P_{max} = maximum load, A_0 = original cross sectional area.

$$\text{Impact strength (Ie)} = \frac{\text{Impactenergy}}{A} \quad (4)$$

where; A = area under the notch.

2.2.5. Analysis of experimental results

In order to achieve optimization and investigate the percentage contribution of individual control factors on the performance of the developed particle board, experimental results obtained from performance examination (tensile, impact energy, hardness, thickness swell, and water absorption) were analyzed using the signal-to-noise (SN) ratio and analysis of variance (ANOVA), respectively. SN ratio values for tensile strength, impact energy, and hardness were calculated using larger-the-better quality characteristics (Equation (5)), while those of thickness swell and water absorption were calculated using smaller-the-better quality characteristics (Equation (6)). All analysis was carried out using a confidence level of 95% and a significance level of 5%.

Larger-the better:

$$S/N = -10\log\frac{1}{n}\left(\sum_{i-1}^{n}\frac{1}{y_i^2}\right) \quad (5)$$

Smaller-the better:

$$S/N = -10\log\frac{1}{n}\left(\sum_{i-1}^{n}y_i^2\right) \quad (6)$$

where, n = number of experimental samples and y = responses of given factor level combination.

2.2.6. Microstructural examination

Fractured surfaces of the optimised tensile test specimen produced using optimal values of composition obtained from GRA were observed using a scanning electron microscope (JEOL, Model No: JSM-7600F, USA) operating at an accelerating voltage of 10 kV after gold sputter coating. Images of the fractured sample were obtained using a magnification of 100× by scanning the test specimens with a focused beam of electrons, which provides information about the surface topography and composition of the sample.

2.2.7. Proposed methods with recently published related works

The methods adopted in this study compared with recently published work are presented in **Table 3**. It can be observed that the experimental technique used in most studies is trial-and-error. However, this study adopted Box-Behnken's design technique. Thereby, reducing the number of experiments, ensuring appropriate data collection and analysis, and also ensuring that conclusions from this study are valid. Also, compared to other recent studies, agro-wastes were utilized along with waste sachet LDPE. Hence, reducing the cost of production and nuisance posed by these wastes to the environment.

Table 3. Proposed methods with recently published related works.

Parameters	Present work	Yang et al. [34]	Chandran et al. [35]	Krumins et al. [36]
Reinforcement materials	Rice husk and Bagasse (used separately)	ACQ-treated wood and rainscreen bar-treated wood	Rice husk and coconut fiber	Conifer bark
Binder used	LDPE (waste water sachet)	urea–melamine formaldehyde resin	unsaturated polyester resin	Bio-adhesives
Experimental Design technique	Box-Behnken's Design Technique	Trial and error method	Trial and error method	Trial and error method
Number of samples produced	Fifteen	Five	three	Three
Properties investigated	Tensile strength, impact energy, hardness, water absorption, thickness swell and microstructure	Density and moisture content, thickness swelling, water absorption, bending strength and Internal bond strength	Water absorption, thickness swelling, modulus of elasticity and modulus of rupture.	Density, bending strength and modulus of rupture
Production parameters used	Moulding pressure—10 MPa, moulding temperature—140 °C and curing time—10 min	Moulding temperature (200 °C), moulding pressure (100 kgf/cm^3) and curing time (15 min)	Moulding temperature (65 °C) and curing time (2 h)	Moulding temperature (40–160 °C), moulding pressure (1–5 MPa)

3. Results and discussion

3.1. Experimental results

The summary of the experimental results for properties of the developed particle boards along with their corresponding signal-to-noise (SN) ratio values for bagasse-based particle board (BPB) and rice husk-based particle board (RPB) are shown in **Tables 3** and **4**, respectively. The results for BPB in **Table 3** showed ultimate tensile strength (UTS), impact energy (Ie), hardness (Ha), water absorption (Wa), and thickness swell (Ts) fall within 9.19 ± 6.08 MPa, 1.771 ± 1.097 J/mm^2, 68 ± 47 HV, 1.924% ± 1.191%, and 1.577 ± 0.977, respectively, while the results for RPB presented in **Table 4** revealed that ultimate tensile strength (UTS), impact energy (Ie), hardness (Ha), water absorption (Wa), and thickness swell (Ts) fall within 7.33 ± 4.54 MPa, 1.322 ± 0.819 J/mm^2, 61 ± 42 HV, 5.011% ± 2.723%, and 3.929 ± 2.053, respectively. The bagasse-based particle board (BPB) showed better performance compared to the rice husk-based particle board (RPB). This may be attributed to the higher dendrite size and formation of coarse grain structure in the composite [37]. In addition, the SN ratio measures how the response varies relative to the target value under different noise conditions. Anugraha et al. [38] have revealed higher values of the SN ratios identify control factor settings that minimize the effects of the noise factors. Hence, the values in **Tables 4** and **5** indicate the signal levels (response value) for tensile strength, hardness, and impact energy are greater than the experimental noise level, while those of water absorption and thickness swell showed more influence of experimental noise, which slightly tends to affect the response or signal values. However, samples with higher SN values showed better signal quality (response value).

Table 4. Experimental results and SN ratio values for BPB.

Run	Experimental results					Signal-to noise ratios (dB)				
	UTS (Mpa)	Ie (J/mm^2)	Ha (HV)	Ts (%)	Wa (%)	UTS	Ie	Ha	Ts	Wa
1	9.19	1.659	65	1.265	1.037	19.266	4.397	36.253	−2.042	−0.316
2	6.73	1.479	53	1.606	1.317	16.560	3.399	34.426	−4.115	−2.392
3	7.28	1.477	47	1.603	1.315	17.243	3.388	33.449	−4.099	−2.379
4	6.19	1.675	48	1.819	1.491	15.834	4.480	33.654	−5.197	−3.470
5	9.02	1.116	59	1.477	1.212	19.104	0.953	35.470	−3.388	−1.670
6	6.46	1.166	62	1.800	1.476	16.205	1.334	35.792	−5.105	−3.382
7	9.82	1.627	68	1.191	0.977	19.842	4.228	36.691	−1.518	0.202
8	9.29	1.361	55	1.212	0.994	19.360	2.677	34.788	−1.670	0.052
9	6.59	1.097	52	1.766	1.448	16.378	0.804	34.240	−4.940	−3.215
10	6.08	1.214	48	1.924	1.577	15.678	1.684	33.654	−5.684	−3.957
11	8.20	1.400	64	1.425	1.168	18.276	2.923	36.102	−3.076	−1.349
12	8.19	1.771	59	1.317	1.080	18.266	4.964	35.470	−2.392	−0.668
13	7.54	1.383	60	1.501	1.231	17.547	2.816	35.632	−3.528	−1.805
14	7.60	1.324	59	1.483	1.215	17.616	2.438	35.470	−3.423	−1.692
15	7.66	1.371	58	1.488	1.220	17.685	2.741	35.304	−3.452	−1.727

Table 5. Experimental results and SN ratio values for RPB.

Run	Experimental results					Signal-to noise ratios (dB)				
	UTS (Mpa)	Ie (J/mm^2)	Ha (HV)	Wa (%)	Ts (%)	UTS	Ie	Ha	Wa	Ts
1	6.86	1.238	58	2.952	2.241	16.726	1.854	35.269	−9.402	−7.009
2	5.02	1.104	47	4.018	3.115	14.014	0.859	33.442	−12.080	−9.869
3	5.43	1.102	42	4.01	3.108	14.696	0.844	32.465	−12.063	−9.850
4	4.62	1.25	43	4.683	3.66	13.293	1.938	32.669	−13.410	−11.270
5	6.73	0.833	53	3.617	2.786	16.560	−1.587	34.486	−11.167	−8.900
6	4.82	0.87	55	4.625	3.613	13.661	−1.210	34.807	−13.302	−11.157
7	7.33	1.214	61	2.723	2.053	17.302	1.684	35.707	−8.701	−6.248
8	6.93	1.016	49	2.788	2.106	16.815	0.138	33.804	−8.906	−6.469
9	4.92	0.819	46	4.519	3.525	13.839	−1.734	33.255	−13.101	−10.943
10	4.54	0.906	43	5.011	3.929	13.141	−0.857	32.669	−13.998	−11.886
11	6.12	1.045	57	3.453	2.651	15.735	0.382	35.117	−10.764	−8.468
12	6.11	1.322	53	3.116	2.375	15.721	2.425	34.486	−9.872	−7.513
13	5.63	1.032	54	3.69	2.846	15.010	0.274	34.648	−11.341	−9.085
14	5.67	0.988	53	3.634	2.798	15.072	−0.105	34.486	−11.208	−8.937
15	5.72	1.023	52	3.649	2.813	15.148	0.198	34.320	−11.243	−8.983

3.2. Analysis of variance

The results of the analysis of variance (ANOVA) conducted using a confidence level of 95% and significant levels of 5% are shown in **Tables 6–9**. The notations DOF, SS, MS, *F*, and *P* were used to represent degree of freedom, sum of squares, *f*-value, and percentage contributions, respectively. Coconut shell was not included in this analysis because all factor levels have the same values; hence, the impact of the materials on the performance of the developed particle board at all levels is considered insignificant. Based on the results obtained, it can be found that the performance of the developed particle board is most influenced by the presence of low density polyethylene (LDPE), with a percentage contribution of 49.7% (UTS), 77.7% (impact energy), 51.3% (hardness), 69.6% (thickness swell), and 69.61% (water absorption) for BPB and a percentage contribution of 50.23% (UTS), 76.1% (impact energy), 51.4% (hardness), 68.5% (thickness swell), and 69.8% (water absorption) for RPB. The effects of all the factors on the performance of the developed particle boards are significant since their *p*-values are greater than 0.010 (1%). However, a percentage error of less than 5% obtained indicates experiments were performed with minimal noise effects [39].

Table 6. ANOVA for mechanical properties of BPB.

Factor	DOF	UTS				Impact energy				Hardness			
		SS	MS	*F*	*P* (%)	SS	MS	*F*	*P* (%)	SS	MS	*F*	*P* (%)
Bagasse	2	9.21	4.60	45.94	45.4	0.13	0.064	78.66	20.9	262.8	131.4	46.2	43.9
LDPE	2	10.09	5.04	50.34	49.7	0.48	0.238	292.2	77.7	307.0	153.5	54.0	51.3
Error	8	1.00	0.10		4.94	0.01	0.001		1.3	28.5	2.8		4.8
Total	14	20.30	1.45		100	0.61	0.044		100.0	598.3	42.7		100

Table 7. ANOVA for physical properties of BPB.

Factor	DOF	Thickness swell				Water absorption			
		SS	MS	*F*	*P* (%)	SS	MS	*F*	*P* (%)
Bagasse	2	0.21	0.10	64.6	28.2	0.14	0.07	59.60	28.04
LDPE	2	0.51	0.25	159.5	69.6	0.34	0.17	148.00	69.61
Error	8	0.02	0.00		2.2	0.01	0.00		2.35
Total	14	0.73	0.05		100.0	0.49	0.03		100.00

Table 8. ANOVA for mechanical properties of RPB.

Factor	DOF	UTS				Impact energy				Hardness			
		SS	MS	*F*	*P* (%)	SS	MS	*F*	*P* (%)	SS	MS	*F*	*P* (%)
Rice husk	2	5.19	2.60	59.93	45.94	0.07	0.033	20.60	19.3	210.1	105.0	48.8	44.0
LDPE	2	5.67	2.84	65.52	50.23	0.26	0.130	81.39	76.1	245.3	122.7	57.0	51.4
Error	8	0.43	0.04		3.83	0.02	0.002		4.7	21.5	2.2		4.50
Total	14	11.30	0.81		100.00	0.34	0.024		100.0	476.9	34.1		100.0

Table 9. ANOVA for physical properties of RPB.

Factor	DOF	Thickness swell				Water absorption			
		SS	MS	*F*	*P* (%)	SS	MS	*F*	*P* (%)
Rice husk	2	1.9	0.96	30.9	27.1	1.36	0.68	79.44	28.4
LDPE	2	4.9	2.44	78.3	68.5	3.34	1.67	195.60	69.8
Error	8	0.3	0.03		4.4	0.09	0.01		1.80
Total	14	7.1	0.51		100.0	4.78	0.34		100.0

3.3. Grey relational analysis

Multi-response optimization of experimental data was carried out using grey relational analysis (GRA). As suggested by Abutu et al. [29], the GRA procedure involved utilizing SN ratio values presented in **Tables 3** and **4** to calculate the grey relational generation (GRG) using larger-the-better attributes shown in Equation (7) for mechanical properties (UTS, impact energy, and hardness) and smaller-the-better attributes shown in Equation (8) for physical properties (thickness swell and water absorption). The calculation of GRG was followed by grey relation coefficient (GRC) calculation using Equation (9) and thereafter, grey relational grade (GR-grade) using Equation (10). The final process of GRA is the determination of optimal conditions for the single response.

$$\text{Larger} - \text{thebetterattributes}\ (y_{ij}) = \frac{p_{ij} - \underline{p_i}}{\overline{p_i} - p_j} \tag{7}$$

$$\text{Smaller} - \text{thebetterattributes}\ (x_{ij}) = \frac{\overline{p_j} - p_{ij}}{\overline{p_j} - \underline{p_j}} \tag{8}$$

(i = 1, 2, 3, 4, …, u and j = 1, 2, 3, 4, …, v).

where, $p_i = p_{i1}, p_{i2}, ..., p_{ij}, \ldots, p_{in}$), p_{ij} = the performance value of attribute j of alternative i and $\overline{p_i} = \max\{p_{ij}, i = 1, 2, ..., u\}$ and $\underline{p_i} = \min\{p_{ij}, i = 1, 2, ..., v\}$.

$$GRC(GRC_{oj}, GRC_{ij}) = \frac{\tau_{\min} + E\tau_{\max}}{\tau_{ij} + E\tau_{\max}} \quad (9)$$

where, E is the distinguishing coefficient. Kuo et al. [40] and Abutu et al. [29] reported that 0.5 is the widely accepted value of E.

$\tau_{ij} = p_{oj} - p_{ij}$, $\tau\Delta_{\min} = \min(\tau_{ij}, i = 1, 2, ..., u; j = 1, 2, ..., v)$ and $\tau_{\max} = \max(\Delta_{ij}, i = 1, 2, ..., u; j = 1, 2, ..., v)$.

$$\text{GR} - \text{grade} = \frac{\text{Individual GRC}}{\text{Number of experimental responses}} \quad (10)$$

Tables 10 and **11** show the values of the calculated grey relational generation, grey relational coefficient (GRC), and grey relational grade (GRG) for BPB and RPB, respectively, while the resulting factor effects of the process parameters for BPB and RPB are presented in **Tables 12** and **13**, respectively. The values in bold indicate the optimal level for each process parameter. The main effect plots obtained using the values in **Tables 11** and **12** are shown in **Figures 6** and **7**, respectively.

Table 10. GRG, GRC and GR-grades for BPB.

	GRG					**GRC**					**GR-grade**
Sn	**UTS**	**Ie**	**Ha**	**Ts**	**Wa**	**UTS**	**Ie**	**Ha**	**Ts**	**Wa**	
X_o	1.000	1.000	1.000	1.000	1.000						
1	0.862	0.864	0.865	0.126	0.088	0.783	0.786	0.787	0.364	0.354	0.615
2	0.212	0.624	0.301	0.623	0.441	0.388	0.571	0.417	0.570	0.472	0.484
3	0.376	0.621	0.000	0.620	0.438	0.445	0.569	0.333	0.568	0.471	0.477
4	0.037	0.884	0.063	0.883	0.624	0.342	0.811	0.348	0.811	0.571	0.576
5	0.823	0.036	0.623	0.449	0.318	0.738	0.341	0.570	0.476	0.423	0.510
6	0.127	0.127	0.723	0.861	0.609	0.364	0.364	0.643	0.782	0.561	0.543
7	1.000	0.823	1.000	0.000	0.000	1.000	0.739	1.000	0.333	0.333	0.681
8	0.884	0.450	0.413	0.036	0.025	0.812	0.476	0.460	0.342	0.339	0.486
9	0.168	0.000	0.244	0.821	0.581	0.375	0.333	0.398	0.737	0.544	0.477
10	0.000	0.212	0.063	1.000	0.707	0.333	0.388	0.348	1.000	0.630	0.540
11	0.624	0.509	0.818	0.374	0.264	0.571	0.505	0.733	0.444	0.404	0.531
12	0.622	1.000	0.623	0.210	0.148	0.569	1.000	0.570	0.388	0.370	0.579
13	0.449	0.484	0.673	0.482	0.341	0.476	0.492	0.605	0.491	0.431	0.499
14	0.465	0.393	0.623	0.457	0.322	0.483	0.452	0.570	0.480	0.424	0.482
15	0.482	0.466	0.572	0.464	0.328	0.491	0.483	0.539	0.483	0.427	0.485

Table 11. GRG, GRC and GR-grades for RPB.

	GRG					**GRC**					**GR-grade**
Sn	**UTS**	**Ie**	**Ha**	**Ts**	**Wa**	**UTS**	**Ie**	**Ha**	**Ts**	**Wa**	
X_o	1.000	1.000	1.000	1.000	1.000						
1	0.862	0.863	0.865	0.132	0.135	0.783	0.785	0.787	0.366	0.366	0.617
2	0.210	0.623	0.301	0.638	0.642	0.388	0.570	0.417	0.580	0.583	0.508
3	0.374	0.620	0.000	0.635	0.639	0.444	0.568	0.333	0.578	0.581	0.501
4	0.037	0.883	0.063	0.889	0.891	0.342	0.810	0.348	0.818	0.821	0.628
5	0.822	0.035	0.623	0.466	0.470	0.737	0.341	0.570	0.483	0.486	0.524

Table 11. (*Continued*).

	GRG					GRC					GR-grade
Sn	**UTS**	**Ie**	**Ha**	**Ts**	**Wa**	**UTS**	**Ie**	**Ha**	**Ts**	**Wa**	
6	0.125	0.126	0.722	0.869	0.871	0.364	0.364	0.643	0.792	0.795	0.591
7	1.000	0.822	1.000	0.000	0.000	1.000	0.737	1.000	0.333	0.333	0.681
8	0.883	0.450	0.413	0.039	0.039	0.810	0.476	0.460	0.342	0.342	0.486
9	0.168	0.000	0.244	0.831	0.833	0.375	0.333	0.398	0.747	0.749	0.521
10	0.000	0.211	0.063	1.000	1.000	0.333	0.388	0.348	1.000	1.000	0.614
11	0.623	0.509	0.818	0.389	0.394	0.570	0.504	0.733	0.450	0.452	0.542
12	0.620	1.000	0.623	0.221	0.224	0.568	1.000	0.570	0.391	0.392	0.584
13	0.449	0.483	0.673	0.498	0.503	0.476	0.492	0.605	0.499	0.502	0.515
14	0.464	0.392	0.623	0.473	0.477	0.483	0.451	0.570	0.487	0.489	0.496
15	0.482	0.465	0.572	0.480	0.485	0.491	0.483	0.539	0.490	0.493	0.499

Table 12. Resulting factor effects of process parameters (BPB).

Factor	Level 1 (−1)	Level 2 (0)	Level 3 (+1)
Bagasse	**0.5708**	0.5133	0.5223
LDPE	0.5175	0.5169	**0.5693**

Table 13. Resulting factor effects of process parameters (RPB).

Factor	Level 1 (−1)	Level 2 (0)	Level 3 (+1)
Rice husk	**0.5808**	0.5387	0.5533
LDPE	0.5625	0.5377	**0.5733**

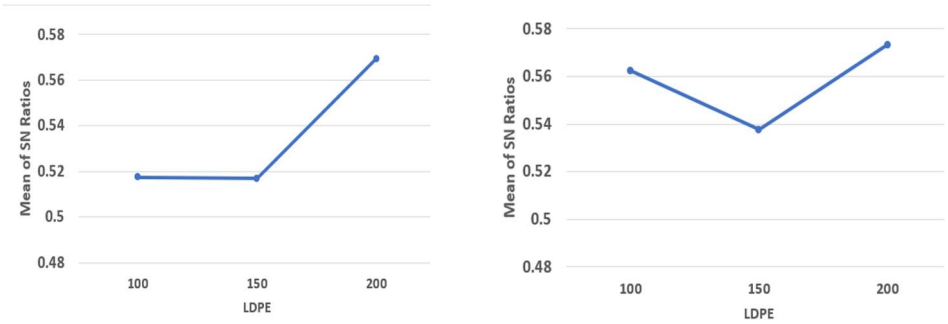

(a) **(b)**

Figure 6. Plots of factor effects for LDPE **(a)** BPB; **(b)** RPB.

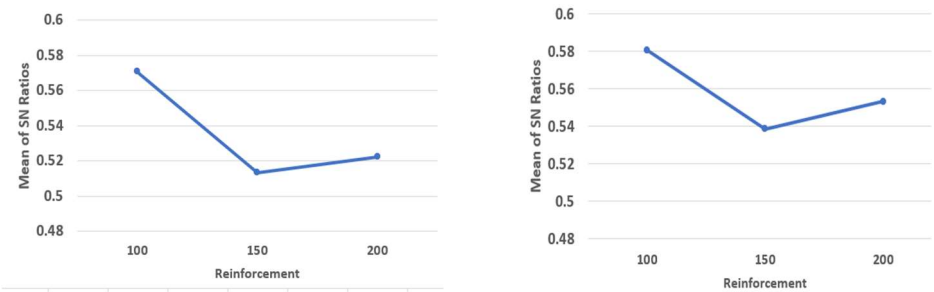

(a) **(b)**

Figure 7. Plots of factor effects for reinforcement **(a)** BPB; **(b)** RPB.

From **Figures 6** and **7**, it can be observed that the multi-response optimum performance of both bagasse and rice husk-based particle board can be obtained using 150 g, 150 g, and 200 g of coconut shells, rice husk or bagasse, and low-density polyethylene (LDPE), respectively. This result is in agreement with the work of Baharuddin et al. [41], who revealed that the quantity of polymer-based binder used in particle board production plays an important role in the quality of the composite. This was also reflected in the results obtained from the analysis of variance presented in **Tables 5–8**.

3.4. Empirical model equations

Empirical model equations for BPB and RPB are presented in Equations (11)–(20). *A*, *B*, and *C* have been used as notations for bagasse, low-density polyethylene, and rice husk, respectively. These equations were obtained with the aid of Minitab 19 statistical software by utilizing a confidence level of 95% and significant levels of 5%. As shown in Equations (11)–(20), it can be observed that the values of some of the regression coefficients (Rsq_{adj}) presented in **Table 14** fall below 80%. This may be attributed to a noise effect resulting from experimental uncertainty [39]. However, the values obtained were in close agreement with the recommended value (80%). Hence, these model equations can be utilised for prediction of the developed particle board properties.

For BPB:

$$\text{UTS (MPa)} = 19.05 - 0.0549A - 0.0724B + 0.000063A \times A + 0.000218B \times B + 0.000102A \times B \quad (11)$$

Rsq = 77.32% and $Rsq_{(adj)}$ = 64.73%.

$$\text{Ie (J/mm}^2\text{)} = -0.429 - 0.00137A + 0.02372B + 0.000007A \times A - 0.000053B \times B - 0.000016A \times B \quad (12)$$

Rsq = 69.25% and $Rsq_{(adj)}$ = 52.17%.

$$\text{Ha (HV)} = 46.8 + 0.089A - 0.045B + 0.000002A \times A + 0.00102B \times B - 0.000784A \times B \quad (13)$$

Rsq = 78.65% and $Rsq_{(adj)}$ = 59.20%.

$$\text{Wa (\%)} = 0.629 + 0.00534A + 0.00211B - 0.000005A \times A - 0.000009B \times B - 0.000012A \times B \quad (14)$$

Rsq = 76.34% and $Rsq_{(adj)}$ = 63.20%.

$$\text{Ts (\%)} = 0.760 + 0.00655A + 0.00262B - 0.000006A \times A - 0.000011B \times B - 0.000015A \times B \quad (15)$$

Rsq = 76.35% and $Rsq_{(adj)}$ = 63.22%.

For RPB:

$$\text{UTS (Mpa)} = 14.20 - 0.0409C - 0.0540B + 0.000047C \times C + 0.000163B \times B + 0.000076C \times B \quad (16)$$

Rsq = 77.26% and $Rsq_{(adj)}$ = 64.62%.

$$\text{Ie (J/mm}^2\text{)} = -0.318 - 0.00102C + 0.01767B + 0.000005C \times C - 0.000039B \times B - 0.000012C \times B \quad (17)$$

Rsq = 69.21% and $Rsq_{(adj)}$ = 52.11%.

$$\text{Ha (HV)} = 41.8 + 0.079C - 0.040B + 0.000002C \times C + 0.00091B \times B - 0.000700C \times B \quad (18)$$

Rsq = 88.65% and $Rsq_{(adj)}$ = 69.20%.

$$\text{Wa (\%)} = 0.96 + 0.0167C + 0.0066B - 0.000016C \times C - 0.000029B \times B - 0.000039C \times B \quad (19)$$

Rsq = 76.36% and $Rsq_{(adj)}$ = 63.22%.

$$\text{Ts (\%)} = 1.39 + 0.0204C + 0.0081B - 0.000020C \times C - 0.000035B \times B - 0.000047C \times B \quad (20)$$

Rsq = 76.34% and $Rsq_{(adj)}$ = 63.20%.

Table 14. Correlation coefficient (Rsq) for developed particle boards.

Response	BPB		RPB	
	Rsq (%)	**$Rsq_{(adj)}$ (%)**	**Rsq (%)**	**$Rsq_{(adj)}$ (%)**
Ultimate tensile strength (MPa)	77.32	64.73	77.26	64.62
Impact energy (J/mm^2)	69.25	52.17	69.21	52.11
Hardness (HV)	78.65	59.20	88.65	69.20
Water absorption (%)	76.34	63.20	76.36	63.22
Thickness swell (%)	76.35	63.22	76.34	63.20

3.5. Microstructure examination

The microstructures of the optimized samples of BPB and RPB obtained are presented in **Figures 8** and **9**, respectively. **Figure 8** shows basically ductile behaviour and revealed uniform distribution of bagasse fibers and coconut shell particles with patches of the LDPE in the developed particle board. Overall observation indicates that the particles of the BPB samples showed very good dispersion of the bagasse and coconut shells. Generally, there was better dispersion between the bagasse fiber, coconut shells, and LDPE matrix with little or no presence of voids in the sample. Unlike BPB, the SEM image of RBP shown in **Figure 9** revealed basically brittle behaviour with uniform distribution of rice husk and coconut shell particles having patches of the LDPE in the sample. Overall observation also indicates that the particles of the RPB samples showed good dispersion of rice husk and coconut shells, though the internal agglomeration observed in the sample may be attributed to non-homogenous particle distribution resulting from a large number of irregularities and structures that tend to collapse under pressure and heat during pressing [42]. De Barros Filho et al. [43] have argued that the amount of collapsed thin-walled particles is dependent on the level of damage caused by hot pressing, which may lead to more intimate contacts between the matrix, rice husk, and coconut shell particles. However, these collapsed thin-walled particles can result in a reduction of mechanical properties such as a reduction in modulus of rupture, tensile strength, hardness, and impact strength [44]. Suherman et al. [45] also reported that the amount of voids in a composite is dependent on the filler/resin content and processing conditions, which in turn affect its performance.

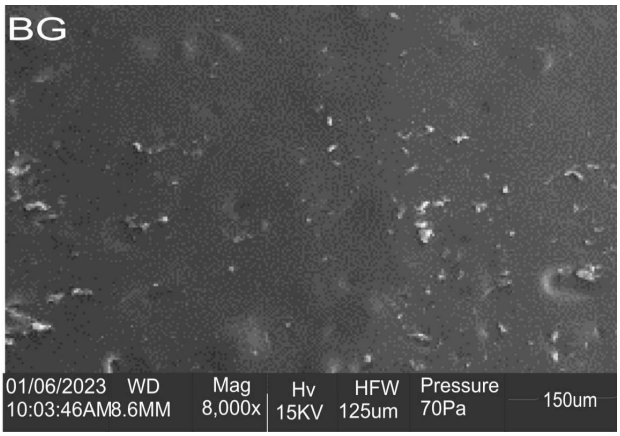

Figure 8. Microstructure of optimized BPB sample.

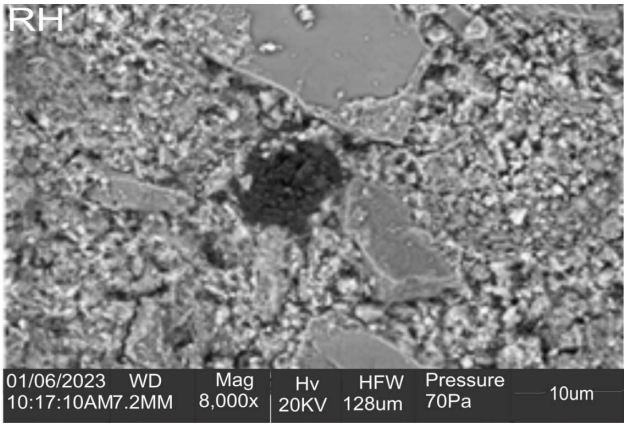

Figure 9. Microstructure of optimized RPB sample.

4. Conclusions

In this study, agro-waste (bagasse, coconut shells, and rice husk) was used as filler materials for the production of particle board. The study also utilized Box-Behnken's design to investigate the effects of composition on the performance of the developed particle board. Based on the result obtained, the following conclusions can be made:

1) Changes in percentage composition affect the performance of the composite, as all the developed particle boards possess varying performance.
2) The performance of the developed bagasse-based particle board (BPB) and rice husk-based particle board (RPB) is most influenced by the presence of low-density polyethylene (LDPE).
3) The multi-response optimum performance of BPB and RPB can be obtained using bagasse or rice husk (30 wt%), coconut shell (30 wt%), and low-density polyethylene (40 wt%).
4) There was better dispersion between the constituents of BPB, which revealed ductile behaviour with little or no presence of voids in the sample. While the microstructure of RPB revealed brittle behaviour with uniform distribution of constituent materials along with patches of LDPE in the sample.
5) Compared to rice husk, bagasse can effectively serve as a preferred substitute for wood in the production of particle board.

Author contributions: Conceptualization, JA and TRT; methodology, ADA; software, JA; validation, AS, SAL and AKR; formal analysis, JA; investigation, TRT; resources, AS; data curation, TRT; writing—original draft preparation, JA; writing—review and editing, SAL; visualization, AKR; supervision, JA; project administration, ADA; funding acquisition, TRT. All authors have read and agreed to the published version of the manuscript.

Funding: The authors are grateful to Tertiary Education Trust Fund (TETFund) for the grant (TETFUND/TSU/2023/IBR) allocated to this research.

Conflict of interest: The authors declare no conflict of interest.

References

1. Hassan BB, Awopetu OO. Production and characterization of particle boards from common agro wastes in Nigeria. International Journal of Innovative Science and Research Technology. 2019; 4(1): 637-642.
2. Rivela B, Moreira MT, Muñoz I, et al. Life cycle assessment of wood wastes: A case study of ephemeral architecture. Science of The Total Environment. 2006; 357(1-3): 1-11. doi: 10.1016/j.scitotenv.2005.04.017
3. Saeed HSS, Syamsir A, Abu Bakar MS, et al. A Review of Non-wood Lignocellulose Waste Material Reinforced Concrete for Light-weight Construction Applications. Pertanika Journal of Science and Technology. 2024; 32(3): 979-1001. doi: 10.47836/pjst.32.3.01
4. Mathura F, Maharaj R. Non-wood Plants as Sources of Cellulose for Paper and Biodegradable Composite Materials: An Updated Review. Current Materials Science. 2024; 17(4): 321-335. doi: 10.2174/2666145417666230701000240
5. Morasilp D, Sangkakool T. Process optimization and material characterization of fiberboards produced from pineapple leaf waste. Journal of Material Cycles and Waste Management. 2024; 26(3): 1480-1489. doi: 10.1007/s10163-024-01899-6
6. Nakrani D, Tiwari MK, Wani T, et al. Characterization of combustion of hardwood and softwood through experimental and computer simulations. Journal of Thermal Analysis and Calorimetry. 2023; 148(15): 7727-7745. doi: 10.1007/s10973-023-12261-7
7. Kumar S, Rawat D, Singh B, et al. Utilization of bamboo resources and their market value in the western Himalayan region of India. Advances in Bamboo Science. 2023; 3: 100019. doi: 10.1016/j.bamboo.2023.100019
8. Asamoah O, Kuittinen S, Abrefa Danquah J, et al. Assessing Wood Waste by Timber Industry as a Contributing Factor to Deforestation in Ghana. Forests. 2020; 11(9): 939. doi: 10.3390/f11090939
9. Nepal P, Johnston CMT, Ganguly I. Effects on Global Forests and Wood Product Markets of Increased Demand for Mass Timber. Sustainability. 2021; 13(24): 13943. doi: 10.3390/su132413943
10. Ganaie TA, Jamal S, Ahmad WS. Changing land use/land cover patterns and growing human population in Wular catchment of Kashmir Valley, India. GeoJournal. 2020; 86(4): 1589-1606. doi: 10.1007/s10708-020-10146-y
11. Ke S, Qiao D, Zhang X, et al. Changes of China's forestry and forest products industry over the past 40 years and challenges lying ahead. Forest Policy and Economics. 2021; 123: 102352. doi: 10.1016/j.forpol.2020.102352
12. Gonzalez-Garcia S, Ferro FS, Lopes Silva DA, et al. Cross-country comparison on environmental impacts of particleboard production in Brazil and Spain. Resources, Conservation and Recycling. 2019; 150: 104434. doi: 10.1016/j.resconrec.2019.104434
13. Ojewumi ME, Ojewumi EO, et al. Production of Particleboard from Agricultural Waste - A Sustainable Approach to Waste Management. Journal of Sustainable Materials Processing and Management. 2023; 3(2). doi: 10.30880/jsmpm.2023.03.02.007
14. Sylvani MM. Development of Particle Boards with Fillers from Various Kinds of Wood Scraps and Agricultural Residues Using Binders. PROIROFONIC. 2024; 1(1): 291-300.
15. Auriga R, Borysiuk P, Auriga A. An attempt to use „Tetra Pak" waste material in particleboard technology. Annals of WULS, Forestry and Wood Technology. 2021; 114: 70-75. doi: 10.5604/01.3001.0015.2376
16. Acda MN, Cabangon RJ. Termite resistance and physico-mechanical properties of particleboard using waste tobacco stalk and wood particles. International Biodeterioration & Biodegradation. 2013; 85: 354-358. doi: 10.1016/j.ibiod.2013.08.019
17. Atoyebi OD, Aladegboye OJ, Fatoki FO. Physico-Mechanical Properties of Particle Board made from Coconut Shell, Coconut Husk and Palm Kernel Shell. IOP Conference Series: Materials Science and Engineering. 2021; 1107(1): 012131. doi: 10.1088/1757-899x/1107/1/012131
18. Xu J, Widyorini R, Kawai S. Properties of kenaf core binderless particleboard reinforced with kenaf bast fiber-woven sheets. Journal of Wood Science. 2005; 51(4): 415-420. doi: 10.1007/s10086-004-0672-9
19. Paridah MT, Juliana AH, El-Shekeil YA, et al. Measurement of mechanical and physical properties of particleboard by hybridization of kenaf with rubberwood particles. Measurement. 2014; 56: 70-80. doi: 10.1016/j.measurement.2014.06.019
20. Juliana AH, Paridah MT, Rahim S, et al. Properties of particleboard made from kenaf (*Hibiscus cannabinus* L.) as function of particle geometry. Materials & Design. 2012; 34: 406-411. doi: 10.1016/j.matdes.2011.08.019
21. Tabarsa T. Producing Particleboard Using of Mixture of Bagasse and Industrial Wood Particles. Key Engineering Materials. 2011; 471-472: 31-36. doi: 10.4028/www.scientific.net/kem.471-472.31
22. Ghalehno MD, Nazeriasn M. Physical and mechanical properties of particleboard from roselle (*Hibiscus sabdariffa*) stalks

and eucalyptus (*Eucalyptus camaldulensis*) wood particles. Wood Material Science and Engineering. 2012; 7(1): 25-29. doi: 10.1080/17480272.2011.647070

23. Hidayat H, Keijsers ERP, Prijanto U, et al. Preparation and properties of binderless boards from *Jatropha curcas* L. seed cake. Industrial Crops and Products. 2014; 52: 245-254. doi: 10.1016/j.indcrop.2013.10.024
24. Guler C, Copur Y, Tascioglu C. The manufacture of particleboards using mixture of peanut hull (*Arachis hypoqaea* L.) and European Black pine (*Pinus nigra* Arnold) wood chips. Bioresource Technology. 2008; 99(8): 2893-2897. doi: 10.1016/j.biortech.2007.06.013
25. Guntekin E, Karakus B. Feasibility of using eggplant (*Solanum melongena*) stalks in the production of experimental particleboard. Industrial Crops and Products. 2008; 27(3): 354-358. doi: 10.1016/j.indcrop.2007.12.003
26. Parameswaran B. Biotechnology for Agro-Industrial Residues Utilisation. Springer Dordrecht; 2009.
27. Akshaya V, Akila I, Murali R, et al. Rice Straw Biomass and Agricultural Residues as Strategic Bioenergy: Effects on the Environment and Economy Path with New Directions. In: Bioenergy: Impacts on Environment and Economy. Springer Nature Singapore; 2003. pp. 139-164.
28. Salmah H, Koay S, Hakimah O. Surface modification of coconut shell powder filled polylactic acid biocomposites. Journal of Thermoplastic Composite Materials. 2012; 26(6): 809-819. doi: 10.1177/0892705711429981
29. Abutu J, Lawal SA, Ndaliman MB, et al. Effects of process parameters on the properties of brake pad developed from seashell as reinforcement material using grey relational analysis. Engineering Science and Technology, an International Journal. 2018; 21(4): 787-797. doi: 10.1016/j.jestch.2018.05.014
30. Lekshmi MS, Vishnudas S, Anil KR. Lignocellulosic materials as reinforcement and replacement for binders in masonry mortar. Construction and Building Materials. 2021; 282: 122607. doi: 10.1016/j.conbuildmat.2021.122607
31. Suleiman IY, Aigbodion VS, Shuaibu L, Shangalo M. Development of eco-friendly particleboard composites using rice husk particles and gum Arabic. Journal of Materials Science and Engineering with Advanced Technology. 2013; 7(1): 75-91.
32. Mohan-Kumar K, Naik V, Waddar SS, et al. Mechanical and Water Absorption Characterization of Mango Seed Shell/Epoxy Composite for Low Load Carrying Structures. International Journal of Polymer Science. 2023; 2023: 1-15. doi: 10.1155/2023/9976409
33. Pang JC, Li SX, Wang ZG, et al. Relations between fatigue strength and other mechanical properties of metallic materials. Fatigue & Fracture of Engineering Materials & Structures. 2014; 37(9): 958-976. doi: 10.1111/ffe.12158
34. Yang S, Galih NM, Kim J, et al. Physical and mechanical properties of particleboard mixed with waste ACQ-treated wood. Journal of Material Cycles and Waste Management. 2023; 26(1): 410-420. doi: 10.1007/s10163-023-01837-y
35. Chandran A, Ismail A, Charles B, Thejal TT. Particle board using rice husk and coconut fibre. Sustainability, Agri, Food and Environmental Research. 2024; 12(1).
36. Krumins JA, Vamza I, Dzalbs A, et al. Particle Boards from Forest Residues and Bio-Based Adhesive. Buildings. 2024; 14(2): 462. doi: 10.3390/buildings14020462
37. Moi SC, Pal PK, Bandyopadhyay A, et al. Determination of Tungsten Inert Gas Welding Input Parameters to Attain Maximum Tensile Strength of 316L Austenitic Stainless Steel. Strojnícky casopis—Journal of Mechanical Engineering. 2018; 68(3): 231-248. doi: 10.2478/scjme-2018-0037
38. Anugraha RA, Wiraditya MY, Iqbal M, et al. Application of Taguchi Method for Optimization of Parameter in Improving Soybean Cracking Process on Dry Process of tempeh Production. IOP Conference Series: Materials Science and Engineering. 2019; 528(1): 012070. doi: 10.1088/1757-899x/528/1/012070
39. Abutu J, Lawal SA, Ndaliman MB, et al. Production and characterization of brake pad developed from coconut shell reinforcement material using central composite design. SN Applied Sciences. 2019; 1(1). doi: 10.1007/s42452-018-0084-x
40. Kuo Y, Yang T, Huang GW. The use of a grey-based Taguchi method for optimizingmulti-response simulation problems. Engineering Optimization. 2008; 40(6): 517-552.
41. Baharuddin MNM, Zain NM, Harun WSW, et al. Development and performance of particleboard from various types of organic waste and adhesives: A review. International Journal of Adhesion and Adhesives. 2023; 124: 103378. doi: 10.1016/j.ijadhadh.2023.103378
42. Malaki M, Fadaei Tehrani A, Niroumand B, et al. Wettability in Metal Matrix Composites. Metals. 2021; 11(7): 1034. doi: 10.3390/met11071034
43. de Barros Filho RM, Mendes LM, Novack KM, et al. Hybrid chipboard panels based on sugarcane bagasse, urea formaldehyde and melamine formaldehyde resin. Industrial Crops and Products. 2011; 33(2): 369-373. doi:

10.1016/j.indcrop.2010.11.007

44. Pai A, Rodriguez-Millan M, Beppu M, et al. SS. Experimental techniques for performance evaluation of shielding materials and configurations subjected to Blast and Ballistic impacts: A State-of-the-Art Review. Thin-Walled Structures. 2023; 191: 111067. doi: 10.1016/j.tws.2023.111067
45. Suherman H, Dweiri R, Sulong AB, et al. Improvement of the Electrical-Mechanical Performance of Epoxy/Graphite Composites Based on the Effects of Particle Size and Curing Conditions. Polymers. 2022; 14(3): 502. doi: 10.3390/polym14030502

Materials Technology Reports 2024, 2(1), 1556.
https://doi.org/10.59400/mtr.v2i1.1556

Article

The negative differential resistance of nitrogen implanted TiO_2

Chun-Ming Liu

School of Physics, University of Electronic Science and Technology of China, Chengdu 610054, China; cmliu@uestc.edu.cn, cmliu028@163.com

CITATION

Liu CM. The negative differential resistance of nitrogen implanted TiO_2. Materials Technology Reports. 2024; 2(1): 1556. https://doi.org/10.59400/mtr.v2i1.1556

ARTICLE INFO

Received: 23 February 2024
Accepted: 9 April 2024
Available online: 25 April 2024

Abstract: The microstructure and negative differential resistance (NDR) effect of nitrogen implanted rutile TiO_2 were investigated by measuring the XPS, Raman spectra and current voltage curves. It was found that the light illumination has large influence on the NDR effect. Under the illumination of 60 mW laser light, a large NDR with a small electric field (1250 V/cm) is obtained. This electric field is about three orders smaller than that reported in literature (1×10^6 V/cm). The electric field induced tunneling is the possible mechanism of electric transport at higher field region. The NDR is thought to be related to the light and nitrogen dopant induced reaction including the destroying of water, the scavenging of electron, and the surface oxidation transform of non-stoichiometric TiO_{2-x} to stoichiometric insulating state. The results of this paper are not only useful in understanding the mechanism of NDR, but also useful in providing an effective method in manipulation NDR.

Keywords: negative differential resistance; nitrogen implanted TiO_2; light assistance

1. Introduction

More and more attention has been paid to nitrogen doped TiO_2 due to its interesting property and various potential applications including photo catalyst [1–3], diluted magnetic semiconductor [4–6], thermo-electronics [7], electron field emission [8] and electrical transport property [9,10]. It is found that oxygen vacancy can be favorably generated in nitrogen doped TiO_2 since the formation energy of oxygen vacancy in TiO_2 is largely decreased by nitrogen doping [1]. TiO_2 is changed from insulator to semiconductor since the electrical resistivity of TiO_2 was reduced by the formation of oxygen defects [7]. The band gap of TiO_2 can be effectively decreased. The photo catalyst activity under visible light can be greatly enhanced [1–3]. Magneli phase of Ti_n $(O, N)_{2n-1}$ can also be obtained [7]. Furthermore, it was found that the oxygen vacancy of nitrogen doped TiO_2 has better stability than that of pure TiO_2 [8].

It is well known that the generation and redistribution of oxygen vacancies are closely related to many interesting phenomena such as the NDR and the resistance switching (RS) of TiO_2 [11–15]. For example, the generated oxygen vacancies can migrate under bias voltage and then form conductive filaments [14]. Once two metal electrodes are connected by conductive filaments, materials are changed from high resistance state to low resistance state because current can pass through these filaments. On the other hand, due to the Joule heat or the ionic migration, filaments rupture and materials are changed into high resistance state. However, there are few reports on NDR and RS of nitrogen doped TiO_2.

The NDR and RS effect of TiO_2 have been studied intentionally as there are a lot of potential applications such as the resonant tunneling transistors, oscillators, multipliers, and resistive random-access memory [11–16]. NDR and RS of TiO_2 were thought to be related to the oxygen vacancies, phase changing and electrical

chemical reaction. For example, Kim et al. [11] indicated that NDR is the result of local surface oxidation under bias voltage. The electrical current maximum state is obtained as the oxygen vacancies are formed and subsequently ordered and ultimately leaded phase change from a nonconductive fully-oxidized phase to a conductive oxygen-deficient Magnéli phase [11]. The electrical current minimum state is obtained when the non-stoichiometric TiO_2 transforms to the stoichiometric insulating state. Zhao et al. [13] assigned the NDR to the damage of hydrogen-bonds among water molecules to break the continuous water layer. Wang et al. [12] assigned the NDR of $Pt/BiFeO_3/TiO_2/BiFeO_3/Pt$ to the polarization field in the two $BiFeO_3$ layers which causing the movement of electrons to be bound. Kamaladasa et al [16] found that the bias voltage induced reversible bipolar RS in TiO_2 is companied with the reversible formation and dissociation of shear faults. The shear faults are induced by the increasing of oxygen vacancy concentration to some extent [16].

2. Experiments

Experimentally, the single crystal TiO_2 substrates were available from Hefei Kejing Materials Technology Co.Ltd. The nitrogen implantation was performed at the energy of 60 keV in a vacuum chamber of 2×10^{-3} Pa, with the nominal dose of 1×10^{18} ions cm^{-2}. The substrate was kept at room temperature by the circulation of cooling water during ion implantation. The samples' stoichiometry was measured by a KRATOS X SAM 800 x-ray photoelectron spectroscopy (XPS). Raman spectra were obtained by a HORIBA LABRAM HR laser Raman spectrometer. The current voltage curve was measured using two terminal methods. The distance between the two electrodes is about 2 mm. The sample size for I-V measurement is about $4 \times 5 \times 0.5$ mm^3. The light illumination is using a laser with the wavelength of 405 nm. The laser beam diameter is about 2.5 mm.

3. Results and discussions

In a previous paper [4], the microstructure, light absorption, magnetism and electrical transport property of nitrogen implanted TiO_2 single crystal were investigated. It was found that the nitrogen implanted TiO_2 is with a single rutile crystal structure. The absorption in the visible light region is greatly enhanced with nitrogen implantation. Room-temperature ferromagnetism is obtained in the sample with an implanted dose of about 1×10^{18} ions/cm^2. The sample changes from insulating to semiconductor when nitrogen doping increasing to 1×10^{18} ions/cm^2. The incorporation of nitrogen is confirmed by XPS measurements.

Figure 1 shows the full-survey and high resolution XPS of the sample with an implantation dose of about 1×10^{18} ions/cm^2. Obviously seen in the full-survey spectrum, only four elements, Ti, N, O, and C, are found in this sample. The signal from carbon is mainly introduced by the surface contamination during the XPS measurement. There are no other elements being detected by XPS. The high-resolution N1s spectrum has a broad spectrum ranged from 395eV to 404eV, with the maximum located at about 401 eV. This behavior is similar as that reported in literature [3,17]. The high-resolution N1s spectrum can be fitted by two peaks

located at 399.4 and 402.0 eV, respectively. The peak near 399.4 eV was ascribed to interstitial nitrogen doping with structure of Ti–O–N [10]. The peak near 402 eV was ascribed to titanium oxynitrides [9]or to substantial nitrogen doping with structure of O–Ti–N [3]. It should be kept in mind that the nitrogen state in the doped TiO_2 varies from case to case. For example, peaks at 396–397 eV were attributed to substitutional nitrogen [9]. Peaks at higher binding energies (~400 eV) were ascribed to a generic interstitial site [1]. In the other hand, the signal at 401.3 eV was attributed substitutional nitrogen [3]. The high resolution Ti $2p_{3/2}$ spectrum can be fitted by two peaks located at 458.2 and 458.8 eV. The peak at 458.8 eV was ascribed to stoichiometry TiO_2 crystals. The peak at 458.2 eV was assigned to nitrogen doped TiO_2 structure [8]. There is a 0.6 eV shift to lower binding energy for nitrogen doped TiO_2, which indicates the increasing in electron density around Ti atoms in the nitrogen-doped TiO_2 [8]. The formation of oxygen vacancies induced by nitrogen doping was thought to be responsible for the electron density increasing by reducing the valence state of Ti^{4+} to lower states Ti^{3+} [8]. The high resolution O1s spectrum can be fitted by two peaks located at about 530.8 and 529.9 eV, respectively. The peak near 530.8 eV was assigned to TiO_2. The peak near 529.9 eV was ascribed to nitrogen doped TiO_2 structure [3].

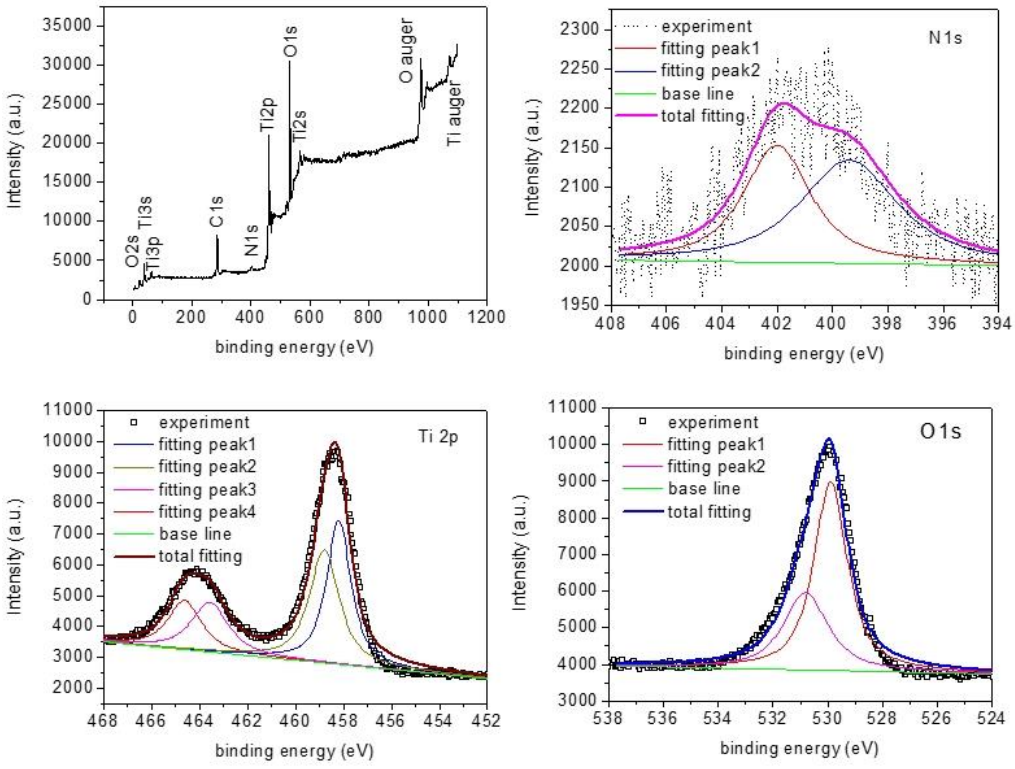

Figure 1. The full-survey and high resolution XPS of the nitrogen implanted TiO_2 sample.

Figure 2 shows the Raman spectra of nitrogen implanted TiO_2 sample. There are peaks located at about 141, 237, 445, and 611 cm^{-1} in the Raman spectra, which can be assigned to the B_{1g} (141 cm^{-1}), two phonon processes E_g(237, 448 cm^{-1}), and A_{1g} (611 cm^{-1}) Raman active modes of the rutile phase TiO_2 [10]. There are no fundamental Raman active modes from anatase phase titanium dioxide including A_{1g} (519 cm^{-1}), B_{1g} (399 cm^{-1}) and E_g (197 and 639 cm^{-1}) [18], indicating that the

sample is of pure rutile structure.

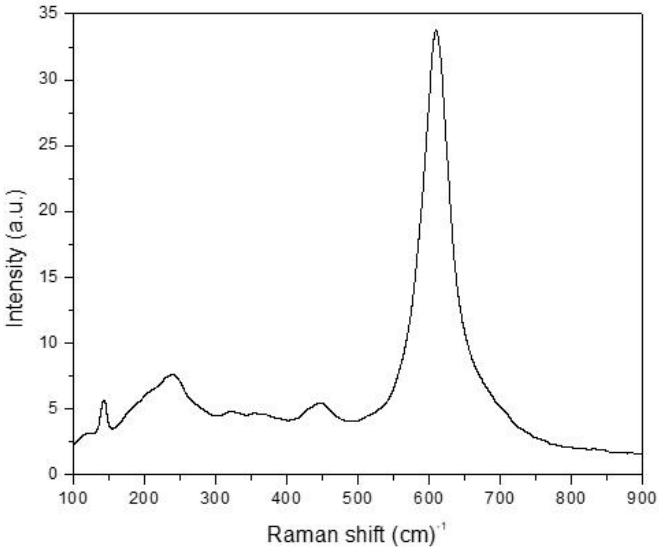

Figure 2. Raman spectra of nitrogen implanted TiO_2 sample.

The current–voltage (I-V) curve of nitrogen implanted TiO_2 sample is shown in **Figure 3a,b**. As seen in **Figure 3a,** without light illumination, there is no NDR in the bias voltage region from 0 to 350 V. The current increases no linearly with voltage increasing. There is little hysteresis between the I-V curves measured with voltage varying from 0 to 350 and then back to 0 V. This behavior indicates that there are little RS effect and NDR without light assistance. The reason should be due to that the bias voltage is not large enough [14]. When the bias voltage is small, it may only generate electronic current and little influence on the chemical or physical state of the materials, and in this situation, the I-V curves are non-hysteretic and closed. When the bias voltage is high enough, the ionic movements and/or the redox reactions are likely to initiate to alter the chemical or physical state of the materials, and in this case, the I-V curves are expected to become hysteretic and open [14]. Since NDR in TiO_2 usually appears with an electric field of about 1×10^6 V/cm [19], the bias voltage should be about 2×10^5 V to induce NDR for our sample.

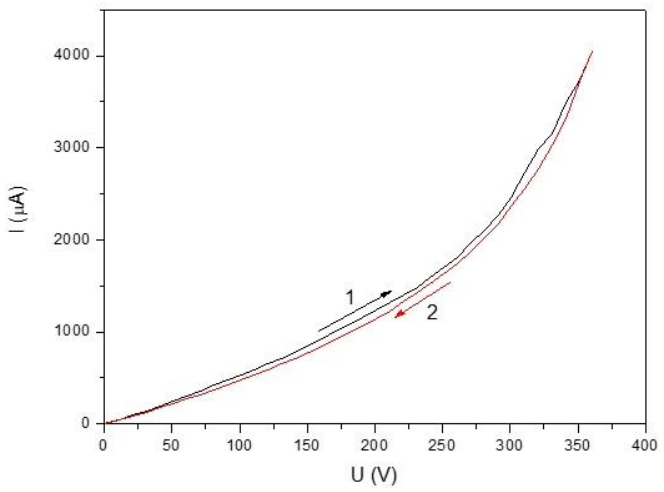

(a)

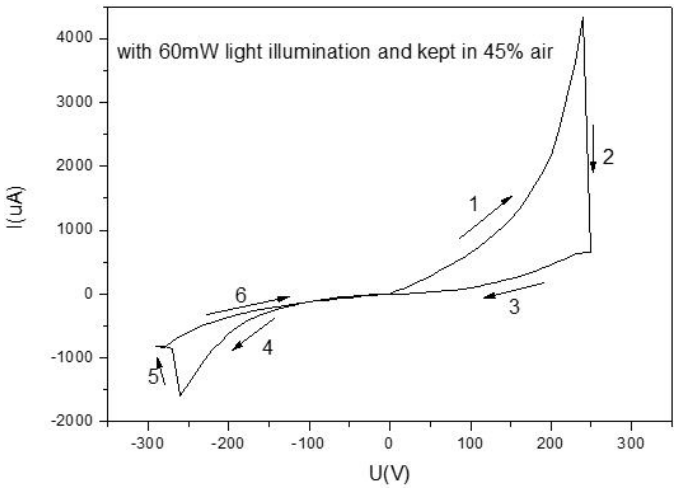

(b)

Figure 3. The current–voltage (I-V) curve of nitrogen implanted TiO_2 sample. **(a)** without light; **(b)** with light illumination. The number in **(a)** and **(b)** is the measuring sequence.

Different from **Figure 3a,b** shows that there is a large hysteresis in the I-V curve when the sample is illuminated with a 60 mW laser. The current increases from 0 to 4326 μA when the bias voltage increases from 0 to 240 V. The current then decreases from 4326 μA to 661 μA when the bias voltage further increases from 240 to 250 V. The ratio of current peak to current valley is about 7. The I-V curve in the positive bias region is different from that in the negative bias region. So, it is not symmetric. In the negative bias region, the current increases to −1590 μA when the bias voltage is ramped up to −260 V. the current then decreases to −854 μA as the voltage is further increased to −270 V. The ratio of current peak to current valley is about 2. Therefore, this NDR is not repeatable and reduces quickly. It is evidently seen that light illumination plays an important role in NDR. The large number of photo-generated charge carriers and the enhanced polarization of $BiFeO_3$ were thought to be responsible for the NDR and RS [12]. The light-enhanced NDR was also reported in MoS_2 quantum dots sample [20]. The electric field to induce NDR in our sample with the assistance of light is about 1.25×10^3 V/cm. This is about three orders smaller than that reported [19]. There is a large reduction in electric field with the assistance of light. This behavior was not reported in the previous literatures [20].

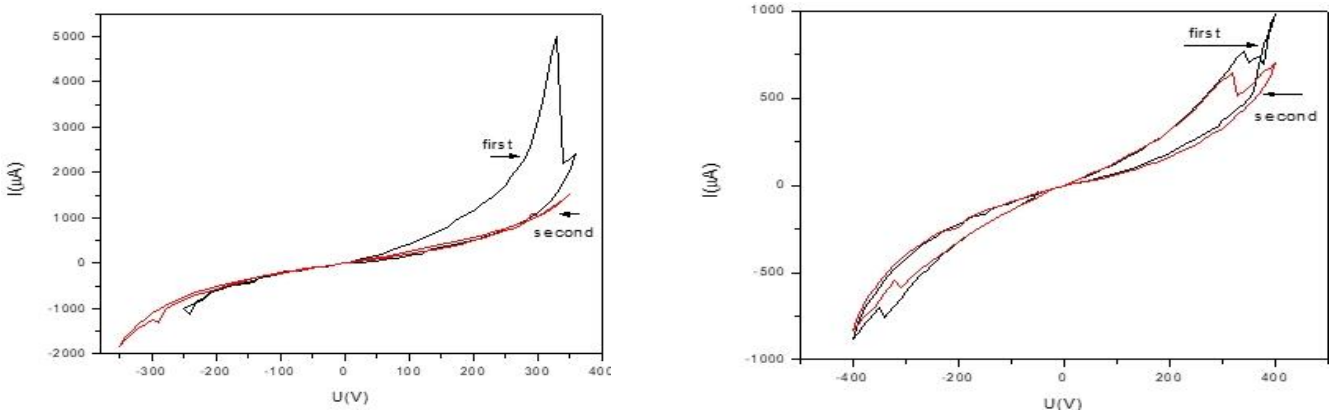

Figure 4. The NDR of sample kept at different humidity environment. **(a)** with 45% RH; **(b)** with 24% RH. The black and red curves are the first and second cycle measured I-V curves, respectively.

Figure 4 shows the NDR of sample kept at different humidity environment, respectively. As seen in **Figure 4**, the NDR in our sample is sensitive to the environment moisture. The NDR is largely recovered when the sample was kept in wet air with a humidity of 45% RH for about 5 days (**Figure 4a**). The ratio of current peak to the current valley is about 2.3. There is large hysteresis in the I-V curve obtained at the first bias voltage changing cycle (0 → 350 → 0→ −350 → 0 V). The hysteresis in the I-V curve becomes very weak in the second voltage changing cycle. In the other hand, the NDR is a little recovered when the sample was kept in dry air with a humidity of about 24% RH for 5 days. The current peak to valley ration is only about 1.3. The I-V curve in **Figure 4b** is almost similar for the two bias voltage changing cycles. The I-V curve in **Figure 4b** is almost similar for the positive bias

region and the negative bias region. In one voltage changing cycle, the bias voltage varies from 0→ 400 → 0 → −400 →0 V. The difference in I-V curve measured in different humidity means that atmosphere plays important role in NDR of nitrogen implanted TiO_2. This behavior is similar as that reported in literature [13].

Figure 5 shows the current (I) as a function of voltage (U) in the higher field region. As seen in **Figure 5**, in the higher field region, the logarithmic of I/U is proportional to the 1/U, i.e., $\ln(I/U) \propto 1/U$. This behavior is the character of metal-insulator granular films at high electric field region where the current is dominated by field induced tunneling [21]. In the case of our sample, the nonconductive fully-oxidized phase of titanium oxides (TO) plays the role of insulator. The water and conductive oxygen-deficient phase of titanium oxides (TO_x) can play the role of metal grains. It was thought that large amount of hydrogen ions can emerge from the ionization of water molecules to create electric current [13]. These conducting grains are randomly distributed and separated by insulator TO barrier. The current carriers transport by tunneling through the insulating barrier separating the conducting grains. This tunneling mechanism is hold in all cases (with light illumination or without light illumination. Before NDR or after NDR). The changing from TO_x to TO would increase the thickness of tunneling barrier and further reduce the tunneling current. On the contrary, the changing from TO to TO_x would decrease the thickness of tunneling barrier and further increase the tunneling current. The desorption (adsorption) of water would also increase (decrease) the tunneling distance and further lead the reduction (enhancement) of tunneling current.

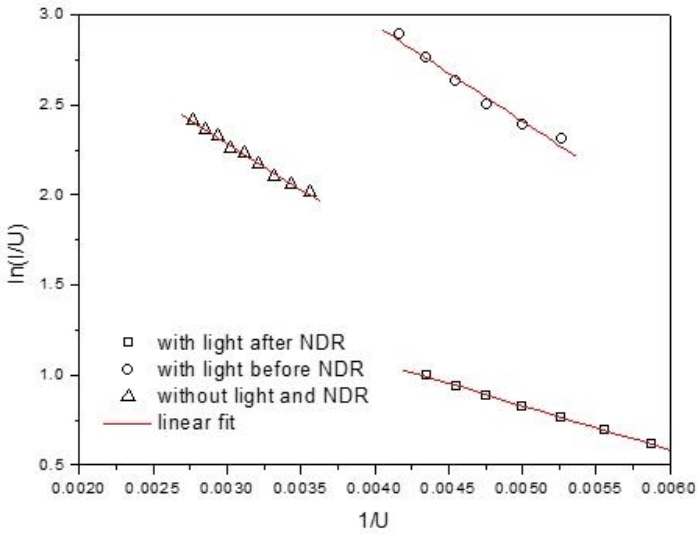

Figure 5. The dependence of Ln (I/U) on 1/U in the higher field region.

Based on the above experiments, the mechanism of NDR of nitrogen implanted TiO_2 should be partly related to the environmental moisture. Water molecular would be adsorbed in the nitrogen implanted TiO_2 sample [13]. With light illumination, a lot of electrons and holes are generated by photo. Some of the photo generated electrons and holes will migrate to the surface of sample, while others are recombined. Under the influence of electrical filed, the generated electrons and holes are further separated by large enough electric field and transport so that the current increases rapidly under a certain electrical filed. Large Joule heat will be generated in the case

of large current. The water molecular will be destroyed by Joule heat and the current is decreased [13]. Once the water is destroyed, there need a time period for water adsorption until the water is recovered again. Therefore, the I-V curve is not symmetrical and not repeatable in wet environment. In addition, the light illumination not only generates electron and hole pairs but also the photo catalyst effect. The photo catalyst can destroy water by changing water molecular into hydrogen and oxygen gas.

Besides the effect of moisture, the oxygen molecular and oxygen vacancy should also be considered. As shown in equation (1), the oxidation of lattice oxygen (O_o^x) and the formation of oxygen vacancies (V_o) in the vicinity are possible [14,22]. This reaction leaves behind two electrons and oxygen vacancy. The generated oxygen vacancies can migrate to form the conductive filaments. This further leads the increasing of electric current. In the reverse reactions, electrons and oxygen vacancy can be reduced and leading the reduction of current [22]. In the other hand, the electron can be scavenged by the adsorbed O_2 and produce adsorbed O_2^- [14]. The photo catalyst can also scavenge the current carriers by producing radicals such as H_2O•, OH•, and O_2•[17].

$$O_o^x \leftrightarrow V_o + 2e + \frac{1}{2}O_2 \tag{1}$$

With light illumination and nitrogen doping, it is advantage not only for the exciting of electron and hole, but also for the scavenging of electron [1]. Irradiation under vacuum with light selectively promotes electrons from nitrogen atom impurities to the conduction band according to the following process (2) and (3) [1].

$$N \xrightarrow{h\nu} N^+ + e \tag{2}$$

$$N^- \xrightarrow{h\nu} N + e \tag{3}$$

On the other hand, the presence of oxygen in the gas phase modifies the situation as a fraction of photo excited electrons is scavenged by O_2 producing adsorbed O_2^-(process (4) and (5)) [1].

$$N^- + O_{2(gas)} \xrightarrow{h\nu} N + O_{2(surf)}^- \tag{4}$$

$$N + O_{2(gas)} \xrightarrow{h\nu} N^+ + O_{2(surf)}^- \tag{5}$$

The nitrogen atom impurities exist either as charged centers (N^-) or as neutral centers (N) in TiO_2 [1]. Under the light irradiation with an energy of hν, electrons are promoted from the localized N-impurity states (N^- and N) to the electron scavengers like O_2 in environment ($O_{2(gas)}$). Then the O_2 in environment becomes negative charged and adsorbed on the surface ($O_{2\,(surf)}^-$). The electric current will be reduced by these electron scavengers. Furthermore, the surface adsorbed O_2^- will heal the defect sites such as oxygen vacancies and Ti^{3+} interstitials [23]. This will lead non-stoichiometric TiO_{2-x} transform to the stoichiometric insulating state, resulting in the NDR effect [11]. The surface oxidation can be reversed by local reduction [11]. The NDR due to surface oxidation should be reversible and repeatable.

4. Conclusion

In summary, with the assistance of visible light illumination, a negative differential resistance (NDR) with small electric filed (~1250 V/cm) and a large peak to valley ratio (~7) is obtained in nitrogen implanted TiO_2 single crystal. The NDR is related to the environment moisture. In higher humidity environment, the ratio of current peak to current valley is higher. However, the NDR in higher humidity is not reversible because the diffusion of water in sample is not fast enough. The possible mechanism of transport and NDR is discussed. The NDR should be related to the nitrogen dopants and the visible light induced reaction such as the destroy of the adsorption water, the scavenging of electron, and the surface oxidation transform of non-stoichiometric TiO_{2-x} to stoichiometric insulating state.

Funding: This study was supported financially by National Natural Science Foundation of China （Grant No 10904008）, the Agricultural Public Welfare Project of Sichuan Province of China (grant no.2015NZ0098), and the Fundamental Research Funds for The Central Universities (grant no.ZYGX2016J062).

Conflict of interest: The author declares no conflict of interest.

References

1. Di Valentin C, Finazzi E, Pacchioni G, et al. N-doped TiO_2: Theory and experiment. Chemical Physics. 2007; 339(1-3): 44-56. doi: 10.1016/j.chemphys.2007.07.020
2. Wang H, Lewis JP. Second-generation photocatalytic materials: anion-doped TiO_2. Journal of Physics: Condensed Matter. 2005; 18(2): 421-434. doi: 10.1088/0953-8984/18/2/006
3. Chen X, Burda C. Photoelectron Spectroscopic Investigation of Nitrogen-Doped Titania Nanoparticles. The Journal of Physical Chemistry B. 2004; 108(40): 15446-15449. doi: 10.1021/jp0469160
4. Liu CM, Xiang X, Zhang Y, et al. Magnetism of a Nitrogen-Implanted TiO_2 Single Crystal. Chinese Physics Letters. 2011; 28(12): 127201. doi: 10.1088/0256-307x/28/12/127201
5. Tao JG, Guan LX, Pan JS, et al. Density functional study on ferromagnetism in nitrogen-doped anatase TiO_2. Applied Physics Letters. 2009; 95(6). doi: 10.1063/1.3204463
6. Bao NN, Fan HM, Ding J, et al. Room temperature ferromagnetism in N-doped rutile TiO_2 films. Journal of Applied Physics. 2011; 109(7). doi: 10.1063/1.3535427
7. Mikami M, Ozaki K. Thermoelectric properties of nitrogen-doped TiO_{2-x} compounds. Journal of Physics: Conference Series. 2012; 379: 012006. doi: 10.1088/1742-6596/379/1/012006
8. Liu G, Li F, Wang DW, et al. Electron field emission of a nitrogen-doped TiO_2 nanotube array. Nanotechnology. 2007; 19(2): 025606. doi: 10.1088/0957-4484/19/02/025606
9. Yu YP, Liu W, Wu SX, et al. Impact of Nitrogen Doping on Electrical Conduction in Anatase TiO_2 Thin Films. The Journal of Physical Chemistry C. 2012; 116(37): 19625-19629. doi: 10.1021/jp300024n
10. Yen Y, Ou S, Lin K. One-Pot Synthesis of Nitrogen-doped TiO_2 Nanowires with Enhanced Photocurrent Generation. Journal of the Chinese Chemical Society. 2017; 64(12): 1392-1398. doi: 10.1002/jccs.201700226
11. Kim Y, Jang JH, Park SJ, et al. Local probing of electrochemically induced negative differential resistance in TiO_2 memristive materials. Nanotechnology. 2013; 24(8): 085702. doi: 10.1088/0957-4484/24/8/085702
12. Wang X, Wang Y, Feng M, et al. Light-induced negative differential resistance effect in a resistive switching memory device. Current Applied Physics. 2020; 20(3): 371-378. doi: 10.1016/j.cap.2019.12.008
13. Zhao X, Chen X, Ding X, et al. Humidity Sensing Properties and Negative Differential Resistance Effects of TiO_2 Nanowires. IEEE Sensors Journal. 2021; 21(17): 18477-18482. doi: 10.1109/jsen.2021.3091536
14. Lu W, Wong LM, Wang S, et al. Effects of oxygen and moisture on the I-V characteristics of TiO_2 thin films. Journal of Materiomics. 2018; 4(3): 228-237. doi: 10.1016/j.jmat.2018.01.005

15. Liu S, Liu B, Wang T, et al. High anisotropic magnetoresistance, perfect spin-filtering effect, and negative differential resistance effect of Cr-doped anatase phase TiO_2. Physica Scripta. 2022; 98(1): 015827. doi: 10.1088/1402-4896/acaa74
16. Kamaladasa RJ, Sharma AA, Lai YT, et al. In Situ TEM Imaging of Defect Dynamics under Electrical Bias in Resistive Switching Rutile-TiO_2. Microscopy and Microanalysis. 2014; 21(1): 140-153. doi: 10.1017/s1431927614013555
17. Chen X, Lou YB., Samia ACS, et al. Formation of Oxynitride as the Photocatalytic Enhancing Site in Nitrogen-Doped Titania Nanocatalysts: Comparison to a Commercial Nanopowder. Advanced Functional Materials. 2005; 15(1): 41-49. doi: 10.1002/adfm.200400184
18. Mahalingam S, Edirisinghe MJ. Novel preparation of nitrogen-doped titanium dioxide films. Journal of Physics D: Applied Physics. 2008; 41(21): 215406. doi: 10.1088/0022-3727/41/21/215406
19. Chopra KL. Avalanche-Induced Negative Resistance in Thin Oxide Films. Journal of Applied Physics. 1965; 36(1): 184-187. doi: 10.1063/1.1713870
20. Sharma S, Chen Y, Santiago SRMS, et al. Light-Enhanced Negative Differential Resistance and Multi-Level Resistive Switching in Glutamine-Functionalized MoS_2 Quantum Dots for Resistive Random-Access Memory Devices. Advanced Materials Interfaces. 2022; 10(2). doi: 10.1002/admi.202201537
21. Sheng P, Abeles B, Arie Y. Hopping Conductivity in Granular Metals. Physical Review Letters. 1973; 31(1): 44-47. doi: 10.1103/physrevlett.31.44
22. Cooper D, Baeumer C, Bernier N, et al. Anomalous Resistance Hysteresis in Oxide ReRAM: Oxygen Evolution and Reincorporation Revealed by In Situ TEM. Advanced Materials. 2017; 29(23). doi: 10.1002/adma.201700212
23. Stevanovic A, Büttner M, Zhang Z, et al. Photoluminescence of TiO_2: Effect of UV Light and Adsorbed Molecules on Surface Band Structure. Journal of the American Chemical Society. 2011; 134(1): 324-332. doi: 10.1021/ja2072737

Materials Technology Reports 2024, 2(1), 1650.
https://doi.org/10.59400/mtr.v2i1.1650

Article

Physico-mechanical characterization of compressed earth blocks reinforced with waste fibers from calamus rotang: Case of the elastic soil of western region of Cameroon

Fabien Kenmogne[1,*], Emmanuel Foadieng[2,3], Olivier Lekeufack Tiokeng[4], Roger Eno[5], Martial Nde Ngnihamye[6], Alphonse Tchoukouabe[1,5], Sorel Holsen Wafo Wafo[1], Moussa Sali[1,7], Emmanuel Yamb Bell[1], Sévérin Nguiya[5]

[1] Department of Civil Engineering, Advanced Teacher Training College of the Technical Education, The University of Douala, Douala 1872, Cameroon
[2] Department of Civil Engineering and Forestry Techniques, Higher Technical Teachers Training College (HTTTC), The University of Buea, Buea 1872, Cameroon
[3] IUT Fotso-Victor of Bandjoun, University of Dschang, Dschang 670, Cameroon
[4] Department of Physics, Faculty of Sciences, The University of Douala, Douala 24157, Cameroon
[5] Laboratory E3M, National Higher Polytechnic School of Douala, The University of Douala, Douala 2701, Cameroon
[6] Department of Civil Engineering, National Advanced School of Public Works, Yaoundé 510, Cameroon
[7] Laboratory of Mechanics and Materials, National Higher Polytechnic School of Maroua, University of Maroua, Maroua 46, Cameroon
*** Corresponding author:** Fabien Kenmogne, kenfabien@yahoo.fr

CITATION

Kenmogne F, Foadieng E, Tiokeng OL, et al. Physico-mechanical characterization of compressed earth blocks reinforced with waste fibers from calamus rotang: Case of the elastic soil of western region of Cameroon. Materials Technology Reports. 2024; 2(1): 1650. https://doi.org/10.59400/mtr.v2i1.1650

ARTICLE INFO

Received: 23 March 2024
Accepted: 20 April 2024
Available online: 1 May 2024

Abstract: In order to enhance the value of local materials and contribute to reducing construction costs in Cameroon, rattan waste is used to reinforce compressed earth blocks (CEB). This main work's objective is the study of the effect of rattan waste on the physical and mechanical properties of CEB. For this, a soil sample taken in the western region of Cameroon, more precisely in Bangangté, was analyzed, the analysis includes the granulometric analysis, the Atterberg limits, and the Proctor test. Then the CEB samples with different rattan waste contents, that is 0%, 2%, 4% and 6%, were developed for a compaction stress of 7.5 MPa. These different samples were characterized through mechanical and physical tests carried out in the laboratory. It appears that the blocks reinforced with 2% of rattan waste have better mechanical characteristics, respectively 0.70 MPa in three-point bending and 3.04 MPa in compression. On the other hand, the presence of rattan wastes has a positive effect on the mechanical behavior of the composite, by increasing its ductility compared to the fragile behavior of the control block, which is observed during crushing. Thus the mechanical properties of CEB improve with the incorporation of rattan waste, which is optimal for a content of 2%. But they increase the material's porosity, and then its sensitivity to water unlike the control CEB.

Keywords: compressed soil block; rattan waste; mechanical characteristics; absorption and porosity; ductility; brittle behaviour

1. Introduction

The current housing situation in Cameroon as presented by civil society actors is unsatisfactory and the issue is also very worrying given the qualitative and quantitative deficits in housing [1]. One of the constraints linked to this deficit in terms of housing is largely due to high construction costs [2]. This situation has pushed Cameroon to direct research towards the valorization of local materials with the target of respect for the environment and low-cost construction. Hence a growing return to raw earth construction, raw soil being one of the oldest materials in construction [3]. It is still

used today in many countries since it is estimated that 30% of housing is built with raw soil in the world [4] and more precisely 85% in poor and developing countries [5]. Indeed, since a century ago, several researchers like Doat et al in 1979 [6]; Houben et al. [7]; …etc, have carried out work aimed at improving the properties of soils in construction. The use of earth in construction has always been an obvious reality because it is available in abundance and widespread throughout the world because it comes from the degradation of rocky substrate. Its proximity, its maneuverability, and its relatively easy implementation require reduced tools, often of peasant origin [8]. It therefore has a positive economic impact because it reduces construction costs; a positive ecological issue because it reduces CO_2 emissions and a social and cultural issue because it allows us to preserve and enhance our resources. Raw soil then stands out as a serious candidate for construction. A glance at the built heritage in raw earth shows that it enjoys both a historical and cultural richness that could inspire modern construction.

All over the world, the compressed earth block (CEB) is the most used in raw earth construction. However, it tends to have a relatively limited lifespan, and it suffers from a lack of strength, from cracking systematically due to withdrawal, and comes faced with problems related to their sensitivity to water [8]. As a result, several means of stabilization have been set up to improve the physical and mechanical properties of CEBs, including the addition of hydraulic binders, namely cement, and lime [9–11]; the addition of natural fibers (raffia fiber, rattan, coconut) and artificial (the carbon fiber) [8, 12–14]. Several studies on the physical and mechanical characterization of CEBs with fibers published in recent years justify this work. For example, from the works of Taallah B in 2014, [8] on the physico-mechanical behavior of the compressed earth block with fiber, it has become evident that the presence of fibers has a positive effect on the mechanical behavior of the composite, by increasing its ductility compared to the fragile behavior of the matrix alone and the importance of the increase in compaction stress on the properties of CEBs. Similarly, authors Ntom Nkotto et al. [14], showed that the mechanical properties of CEBs with the incorporation of coconut fibers are optimal for a content varying from 5% to 8%, but they increase the porosity of the material which increases its sensitivity to water, unlike cement-stabilized CEBs. The works of Danso H et al in 2015 [15] on the Physical, mechanical, and durability properties of soil building blocks reinforced with natural fibers from agricultural waste proved that the physical, mechanical, and durability properties of the blocks were generally improved and a recommendation of 0.5% fiber content and high clayey soil is made. More recently in 2024, Abanda A et al investigated the effects of oil palm mesocarp fibers on the physical and mechanical properties of expansive soils. They showed that the reinforcement of expansive soil for road subgrade is highly discouraged [16]. From these enumerated works, it is obvious that little research has yet been done on rattan fiber as a reinforcing element for CEBs. It is in this concern for the preservation and valorization of rattan waste fibers that our work emerges. The main objective of this work is to improve the physico-mechanical properties of raw soil bricks following the addition of a rattan plant fiber in order to popularize this process in the manufacture of compressed soil blocks in order to solve the problems related to construction costs and environmental preservation.

2. Materials and methods

2.1. Presentation of the raw material

2.1.1. Raw material soil

The soil used was taken from a site near Bangangté city in the Western region of Cameroon, whose geographical coordinates are 5°08′29″ North and 10°31′18″ East, as shown in **Figure 1**.

Figure 1. Geographical location of the city of Bangangté [17].

After a descent on the site, the ground was dug to a depth of 120 cm and the operation was carried out manually using a pickaxe and a shovel. The latter was collected and stored in a woven plastic bag to be transported to the laboratory. The first step in the laboratory is the drying process, in order to remove relatively small amounts of residual water thus rendering the soil samples suitable for packaging and storage, and this was done in an oven for 24 h at 105°C. After drying, the samples, as shown in **Figure 2**, were ground into powder using a ball mill for two hours with constant energy. The powdered soil obtained served as the basic raw material in this study.

2.1.2. Calamus rotang (rattan) waste fibers

Rattans are species of spiny climbing palms belonging to the subfamily Calamoideae of Arecaceae family [18]. It is available all over the world, with varying species, particularly in Asia-Pacific and Africa [18]. The plant waste fibers used are rattan vine of its scientific name calamus, which is stripped of its leaf sheath as shown in **Figure 3**. They are pre-cut into a length of 30 mm long. The diameter of the fibers varies from 3 to 20 mm. The waste fibers obtained are presented in **Figure 4**. They come from the cumulative calamus rejects that were obtained from a technician from the calamus furniture factory in the city of Douala. The product obtained is cut into

reasonable proportions (**Figure 4**), it has been dried before any use.

Figure 2. Lateritic soil sample used.

Figure 3. Calamus stem in the form of a liana.

Figure 4. (a) Calamus cut into pieces; **(b)** waste calamus fibers.

2.2. Methods for physical and mechanical experiments

2.2.1. Water content by steaming

Water content is the determination of the amount (in percent by weight) of water in the soil material. Commonly used methods for determining soil water content are oven drying weighing, electromagnetic technique, and soil water sensor. The oven drying method is easy to implement and is used here, while 5 samples of the same soil were analyzed, taking into account the standard [19]. The operating mode and the apparatus are defined in the said standard. It is calculated according to the following equation:

$$w(\%) = \frac{(m_h - m_s)}{m_s} \times 100 \quad (1)$$

m_h and m_s represent the wet and dry masses of the sample respectively.

2.2.2. Particle size analysis by sieving

This test is applied for aggregates with a diameter greater than 125 micrometers, the handling conditions being described by the standard [20]. The soil was analyzed through the said standard in the Laboratory (**Figure 5**). The equation for calculating the refusal in percentage is as follows:

$$\text{Refusal (\%)} = \frac{\mathrm{M_i}}{\mathrm{M}} \times 100 \quad (2)$$

where M_i is the mass of the sieve rejects of number (i) and M *is* the mass obtained after drying the washed sample, while the percentage of sift is given by.

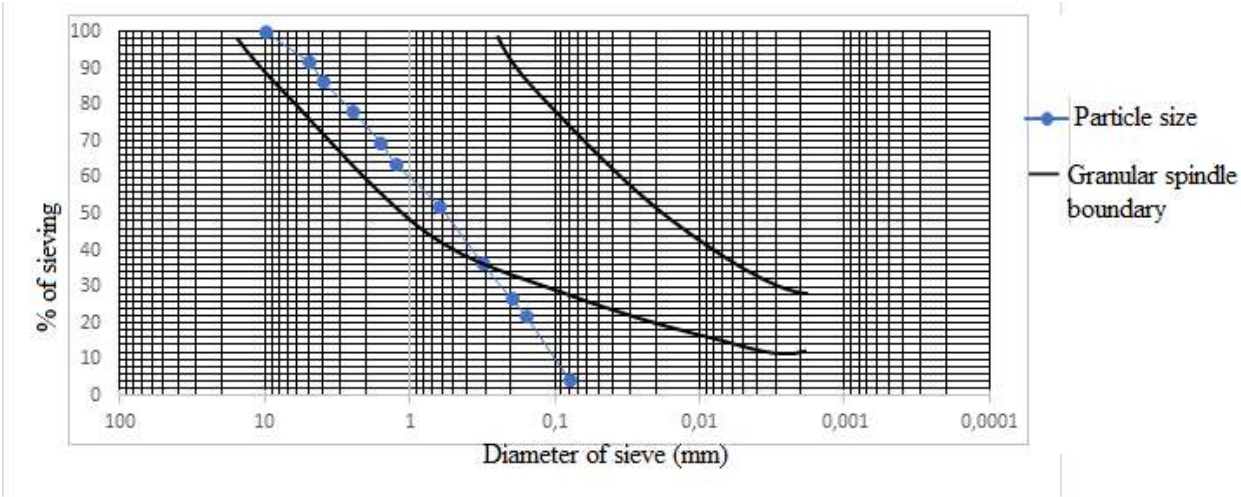

Figure 5. Results of the particle size analysis by sieving.

$$\%\text{Sift} = 100 - \%\text{Refusal} \quad (3)$$

2.2.3. Atterberg limits

Atterberg limits allow the determination of the water contents corresponding to the passage of a soil from the plastic state to the solid state in accordance with the standard [21]. This involves determining the liquidity limits (WL), plasticity limits (WP), and the plasticity index IP.

Liquidity limits (WL)

Liquidity limits allow the determination of the quantity of water required when soil passes from the liquid state to the plastic state. It gives the minimum percentage of water at which the paste can flow under its own weight.

The soil soaked in water is kneaded with a spatula on a glass plate to obtain a homogeneous paste. Let's place part of it in the cup of the Casagrande apparatus. Mix and then spread the material with a spatula to form a smooth paste 12 mm thick from the lower half of the cup,

- A groove is then drawn through the center of the mixture in the diametrical plane perpendicular to the axis of the hinge,
- With the cup placed on the base, it is subjected to 15 shocks by operating the crank of the Casagrande apparatus. Take a small amount of the paste, for the

determination of the water content, when the central groove is closed by about 1 mm.

- If the intended closure is obtained before the 15 expected shocks, repeat the operation by kneading the paste quite vigorously. The objective is to make the dough lose a little water. If, on the contrary, the closure is obtained after the 15 shocks, the dough is slightly moistened, and the operation is resumed by mixing,
- With the flow line requiring at least four points, the water content corresponding to the closure of the central groove is determined for 10, 20, 25, and 30 shocks.

Plasticity limits (WP)

The plasticity limit is used to evaluate the quantity of water for which a soil passes from the plastic state to the solid state. The procedure is as follows:

Take a portion of the mixture and make small rolls on a marble slab until a diameter of 3 mm is obtained. The roller is raised 1 or 2cm above the slab, it cracks and breaks, and the samples are taken from each piece to determine the water content which will be the WP value. The plasticity index Ip is calculated using the following equation

$$\mathrm{Ip} = \mathrm{WL} - \mathrm{WP}, \tag{4}$$

The soil results must be following **Table 1** [22]. The plasticity of the soil will preferably be entered in the zone of the plasticity diagram [22]. The limits of the recommended zones are approximate. In this regard, Cameroonian standard from 102 to 114 specifies that certain soils which do not fall within the recommended zones for the manufacture of earth blocs, still give acceptable results in practice, but that compliant soils give satisfactory results in most cases.

Table 1. Summary of Atterberg limit standards according to [20].

Sample	Liquidity limit (%)	Plastic limit (%)	Plasticity index (%)
(NF P94-051)	25–50	20–35	2–30

2.2.4. Standard proctor test

Standard proctor test allows, by compacting the material at different water contents, to determine the maximum density reached for a given compaction energy, as well as the corresponding optimum water content in accordance with the standard [23].

The operating procedure is as follows:

- The material is dried in the open air or in an oven at a maximum of 60 °C,
- The material is then pulverized to destroy the clods,
- 6 samples of 2.5 kg each are prepared,
- A percentage of wetting water is added to each sample. The water is spread like rain so as to obtain uniform humidification of the mixture,
- The material is carefully mixed to homogenize it, this mixing is done by hand in a tank,
- Introduce the material into the Proctor mold in 3 successive layers and compact it equally slowly at 25 strokes per layer,

- Remove the rise from the mold and level,
- Then weigh the whole,
- Then take 3 samples, one on top, one in the middle, and the last at the base of the mold,
- Then weigh these samples and introduce them into the oven at 105 °C and determine the water content,
- Do the same for all the other samples by varying the water content.

2.3. Mechanical characterization of the material

2.3.1. Formulation and preparation of test specimens

Once in the laboratory, the soil was first spread in a thin layer in the open air for 10 days, then it underwent manual grinding and finally sieved manually using a 1.6mm sieve.

The formulation of the material was carried out while respecting the clause stipulating that the best mixing conditions are met when the soil is dry [24]. In this case, different mixtures were developed and recorded in **Table 2**. For the stabilization of the bricks, 1450 g of soil is used and is varied according to the volume proportions of waste fibers, which are 0%, 2, 4%, and 6% of rattan waste fiber, all under the same quantity of water.

Table 2. Composition of the mixtures.

Formulation	Soil	Volume proportions of Rattan	Water (Ml)
CEBR1 0%	100%	0%	450
CEBR2 2%	98%	2%	450
CEBR3 4%	96%	4%	450
CEBR4 6%	94%	6%	450

In this study, we made blocks of dimensions $4 \times 4 \times 4$ cm^3 for the compression test specimens and $4 \times 4 \times 16$ cm^3 for the bending test specimens. To do this, we used the hydraulic compression press under a compressive stress of 2 MPa.

2.3.2. Three-point bending test

Three-point bending test made it possible to determine the tensile breaking stress by bending of the $4 \times 4 \times 4\ \mathrm{cm}^3$ test specimens. The bending strength (σ_f in MPa) is given by the following relation:

$$\sigma_f = \frac{3}{2} \times \frac{FL}{h^2} \tag{5}$$

In which *F* is the maximum load, *L is* the total length of the specimen, and *h* is its height.

2.3.3. Compression test

Compression test was used to determine the nominal resistance to simple compression of the composite material. It was carried out on the three $4 \times 4 \times 4$ cm^3 specimens resulting from each formulation. The specimens were subjected to simple

compression until crushing using a compression test press. The compressive strength of the blocks σ_c is determined by the following relationship:

$$\sigma_c = \frac{F}{S} \quad (6)$$

where *F* is the maximum breaking load in kilo Newton, and *S* the average surface area of the block test faces in cm^2.

2.3.4. Capillary absorption test

After determining their dry mass, the blocks were immersed so that they were 5mm above the water level. After a certain amount of time, the blocks were removed from the water and wiped with a damp cloth. We then weighed the wet block masses during the test in grams. Do the same while varying the immersion time of the test pieces.), this test was carried out according to the standard [25]. The water absorption rate C_b of each block is conventionally expressed by the equation:

$$Cb = \frac{100\times(m_h - m_s)}{s\sqrt{t}}, \quad (7)$$

where $(m_h - m_s)$ is the mass of water in grams, absorbed by the block during the test. *S* is the surface area of the block, the immersed face, in square centimeter; *t* is the duration of immersion of the block, in minutes.

2.3.5. Density test

The density test consists of weighing each specimen of each sample and calculating the apparent density. The apparent density in the dry state of the specimen is determined by the following equation (expressed in g/m^3):

$$\rho = \frac{M}{V} \quad (8)$$

With *M* the mass in kg and *V* the volume in m^3.

3. Results and discussion

3.1. The soil

3.1.1. Water content

Let W be the natural water content of the material. A wet mass of 450 g of soil is taken and placed in the oven, the dry mass of the soil at the exit of the oven is equal to 397.52 g. The water content is then: *W* = 13.20%.

3.1.2. The particle size analysis by sieving

The results of the particle size analysis by sieving are presented in **Table A1** (in the appendix).

The results obtained allow plotting the curve of the particle size analysis **Figure 6**:

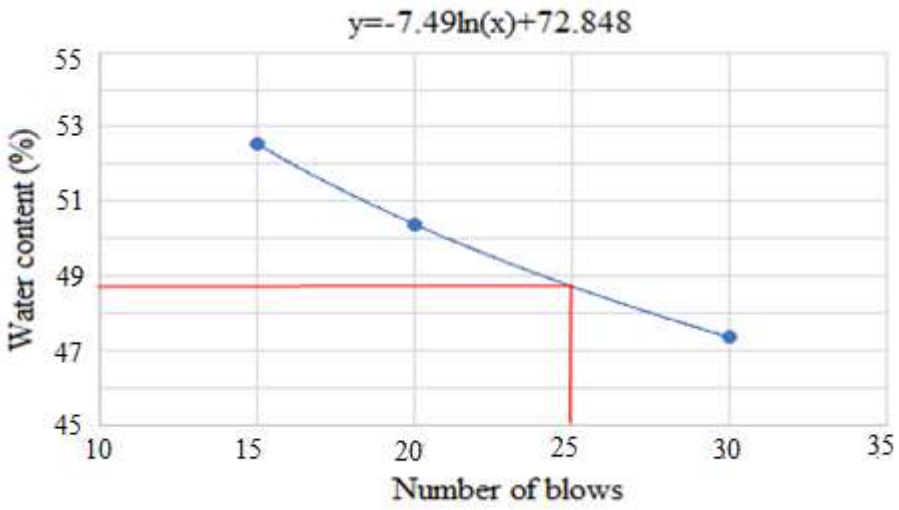

Figure 6. Water content (%) as a function of the logarithm of the number of blows, according to results of **Table A2** in the appendix, given the liquid limit.

Fineness module

It is calculated as follows:

$$M_f = \frac{1}{100}\sum \text{cumulatives refusals } (0.16; 0.315; 1.25; 2.5; 5) \quad (9)$$

which gives $M_f = 2.077$. It is obvious that: $1.8 < M_f < 2.2$, leading that the soils consist of fine grains.

Uniformity coefficient

$$C_u = \frac{D_{60}}{D_{10}} \quad (10)$$

Cu = 10 > 3 varied or spread grain size

Coefficient of curvature

$$C_c = \frac{(D_{30})^2}{D_{60} \times D_{10}} \quad (11)$$

$C_c = 0.625 < 1$ poorly graded soil

By observing the following granulometric curve one notices that a part of the curve at its base comes out of the granular zone of CRA earth and also that the proportion of fine particles is very low. So, the soil under consideration is not among those recommended for the manufacture of CEBs. This result is similar to that of Ntom Nkotto et al. [14] who worked on the characterization of blocks by adding coconut fibers and laterite-cement building materials, who also used a soil sample taken in the western region of Cameroon. To correct this and improve these characteristics, we can add fibers to our soil in order to strengthen it for the manufacture of the CEB.

The fineness modulus of the soil shows that it is made up of fine sand. Similarly, the coefficient of uniformity and curvature shows us a poorly graded soil with varied or spread granulometry explaining the absence of a large variety of diameters.

3.1.3. Atterberg limits

The results of the plasticity and liquidity tests carried out on the soil sample are summarized in **Table A2** (in the appendix). **Figure 6** illustrates the water content as a

function of the logarithm of the number of blows for determining the liquidity limit.

The liquid limit is the water content that corresponds to 25 counts on the curve. We were able to obtain the results of **Table 3** as limits.

Table 3. Values of the Atterberg limits.

Sample	Liquidity limit (%)	Plasticity limit (%)	Plasticity index (%)
Lat B	48.718	34.54	14.178

This plasticity index allows us to classify our soil as moderately plastic soils according to the unified soil classification system (USCS). And the liquid limit allows us to say that our soil is highly cohesive. These values are higher than those of the author [8] who, working on the study of the physico-mechanical behavior of the compressed earth block with fibers, obtained the respective values of 36%, 23%, and 13%. This divergence of results is explained by the fact that: the Atterberg limits make it possible to analyze the variations in consistency of fine soils according to the water content, but in this case, the water content is high given the site of soil sampling as well as the sampling period (climatic conditions). In addition, these values are well within those of the lands usable for CEB according to the standard [26] (see **Table 1**). Putting these values in the plasticity diagram according to USCS, allows us to situate the soil in the silts and slightly plastic organic soils.

3.1.4 Standard proctor test

This test is borrowed from road geotechnics. Indeed, for the construction of rammed earth walls or CEBs, the consistencies of the soils are close to those required for road bodies [27]. The results of the standard proctor test are recorded in **Tables A3–A7** in the appendix and illustrated by the curve of **Figure 7** of dry density as a function of water content.

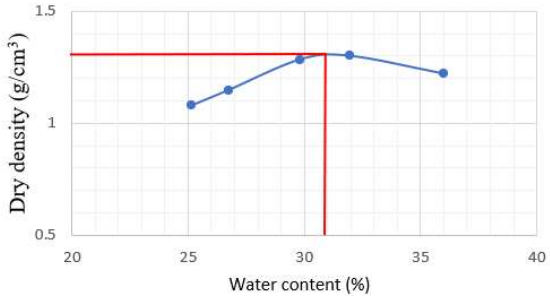

Figure 7. Dry density as a function of water content.

We note that the water content is optimal at the abscissa of the tangent point to the curve, while the dry density is optimal at the ordinate of the tangent point to the curve, i.e.: W_{opn} = 31% and ρ_{opn} = 1.31 g/cm^3.

In addition, this optimal water content is higher than the optimal value recommended for CEBs (see ref [5]) because with higher water content, there is a risk of significant shrinkage during drying and therefore of cracking. Similarly, the optimal dry density obtained is lower than that required for CEBs. However, it is therefore necessary to reinforce our soil. This is what justifies our choice to reinforce the soil with waste fiber in order to obtain better characteristics from the CEBs.

3.2. Characterization of CEB

3.2.1. Mechanical Characterization

Point bending test

The bending test was carried out on three specimens per percentage and the result obtained is the average of the three specimens. **Tables A8–A10** in the appendix provide information on the results that allowed us to plot the bending stress histogram as a function of the percentage of CEB and the Curing time (7, 14, and 28 days) as shown in **Figure 8**. From this graph we see that at 0% fiber, the resistance of the CEB increases and reaches the maximum which is 0.60 MPa after 28 days of curing. The same observation is made at 2%, 4%, and 6% of waste rattan fiber which reaches the maximum values of 0.70 MPa, 0.64 MPa and 0.62 MPa, respectively after 28 days of curing.

At 7 days, the resistance increases according to the rate of waste fiber and reaches the maximum value (0.46 MPa) at 2% and then decreases. Beyond 7 days (14, and 28 days), the same observation is observed the resistance increases and reaches the respective maximum values (0.66 MPa and 0.70 MPa) at 2% of waste fiber then decreases.

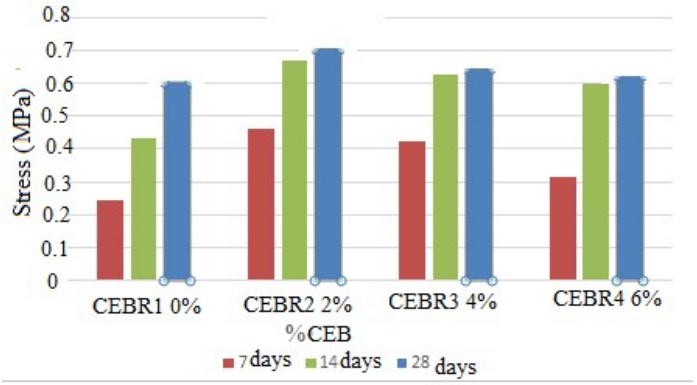

Figure 8. Bending stress at 7, 14, and 28 days.

Given the above results, we can say that the CEB with the addition of fiber which gives acceptable characteristics in bending is the CEBR2 2% with a maximum resistance in bending of 0.70 MPa and is more useful at maturity (28 days). The decrease in flexural strength after 2% fiber may mean the decrease in the fiber-CEB matrix bond because the fibers are increasingly numerous and overlap each other [14]. These flexural strength values are significantly higher than those of the author Djohore [28] which are respectively 0.1; 0.14; 0.15; 0.16; 0.16; and 0.08 MPa for respective fiber contents of 0%; 0.2%; 0.4%; 0.6%; 0.8% and 1%. This difference could be explained either by the difference in fiber used because they do not have the same characteristics, or by the difference in formulation, or by the particle size, or by the fact that this author treated his fibers with a potash solution at a concentration of 8% by mass of potash pellet because the treatment of fibers with basic solutions cleans their surface by degrading amorphous constituents such as lignins, hemicelluloses, waxes and fats [29,30]. Thus, the addition of 2% rattan fibers improves the bending strength of the CEBs.

Compression test

The compression test was carried out on the test pieces per percentage and the result obtained is the average of the three test pieces. **Tables A11–A13** in the appendix provide information on the results which allowed us to plot the compressive stress histogram as a function of the rate of CEB and the maturation time (7, 14 and 28 days) as given in **Figure 9**:

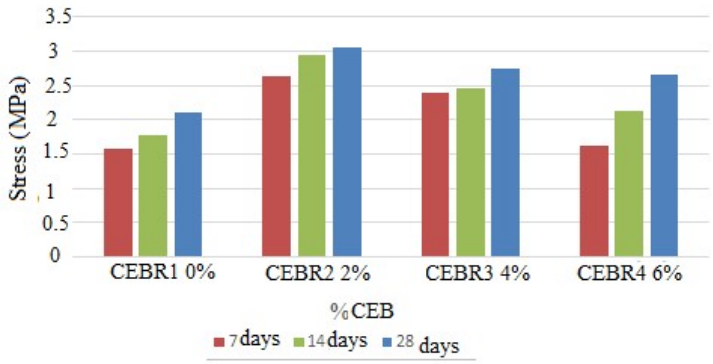

Figure 9. Compressive stress at 7, 14, and 28 days.

From the graph, we see that at 0% fiber, the resistance of CEB increases and reaches the maximum which is 2.10 MPa after 28 days of curing. The same observation is made at 2%, 4%, and 6% which reach the respective maximum values of 3.04 MPa, 2.75 MPa and 2.66 MPa after 28 days of curing.

At 7 days, the resistance increases according to the fiber rate and reaches its maximum value (2.63 MPa) at 2% fiber and then decreases. The same observation is observed at 14 and 28 days with an increasing increase in resistance according to the fiber rate and reaches its maximum value (2.93 MPa and 3.04 MPa respectively) at 2% fiber and then decreases.

Discussion

Because of the above results, we can say that the CEB with added fiber which gives acceptable characteristics in compression is the CEBR2 at 2% of fiber addition, with a maximum compressive strength of 3.04 MPa and is more useful at maturity (28 days); this is the relevant age for exploitation for the manufacture of earth blocks for construction. In addition, the results shown in [31] on the resistance to compression of standard-facing CEBs are between 2–6 MPa. So, the addition of 2% rattan fiber waste improves the compressive strength of the CEBs and meets the conditions for use in construction. It should be noted that the slightest resistance during the initial maintenance period does not limit the use of this material in terms of the construction process or operation of the building. What can limit the use of this material, its availability and the decrease in stress observed in **Figures 9** and **10** after 2%.

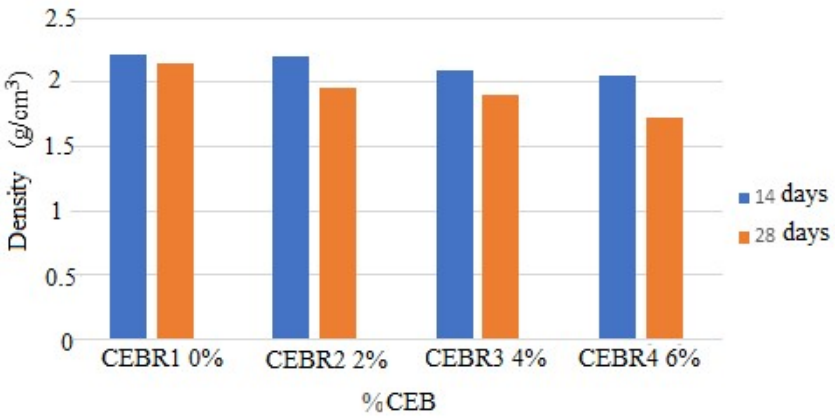

Figure 10. Density of CEB at 14 and 28 days.

Density test at 14 and 28 days

In order to know the effects of calamus fiber on the physical properties of CEBs, the densities are determined for each test piece at 14 and 28 days and we listed them in **Tables A14** and **A15**. The following histogram of **Figure 10** shows the evolution of the density according to the percentages of CEB and the maturation period.

According to this graph, we see that the density drops with the addition of fibers, this is a result of the difference in density between the fibers and the soil; therefore, the more fibers there are, the less dense the material is [32]. We also note that the density decreases with the time of curing this is explained by the fact that the more the duration of curing of the CEB increases, the quantity of water it contains decreases which thus decreases its density over time and in a decreasing way with the increase in rattan fibers. We have the highest density at 0% which is 2.21 g/cm^3 at 14 days and the lowest at 6% which is 1.71 g/cm^3 at 28 days.

3.2.2. Water absorption test by capillary action

In order to know the water absorption speed of the CEBs, we determined the masses of water absorbed by each test piece at 28 days and we listed them in **Table A16**. The curve of **Figure 11** gives the evolution of the masses of water absorbed by percentage as a function of time:

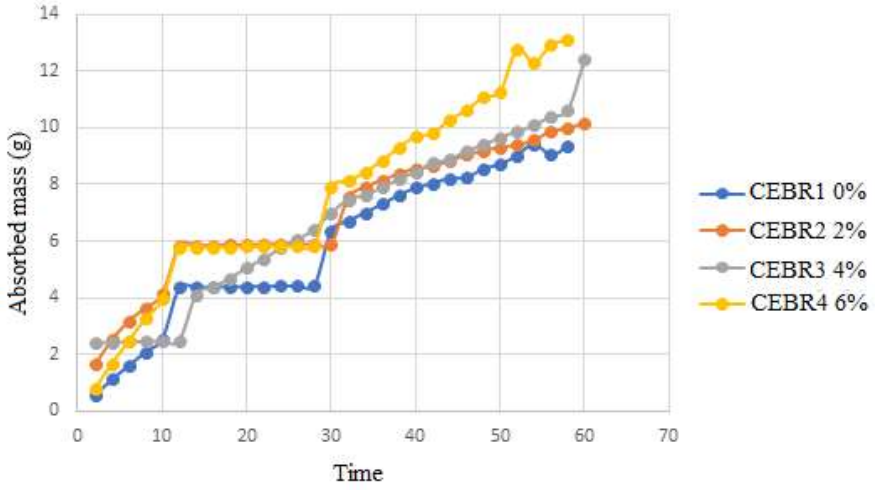

Figure 11. Mass of water absorbed as a function of time.

In view of the curve above, we note that the CEBR1 0% begins with an increasing absorption up to 12 s and then becomes constant up to 28 s with a constant value of 4.43 g and then increases to reach a maximum value of 9.58 g after 58 s. the same observation is made for CEBR2 2% which reaches the constant value of 5.9 g between 12 s and 28 s and then increases to reach a maximum value of 10.62 g after 58 s. as for CEBR3 4%, it begins with a constant absorption of water between 2 s and 12 s with a value of 2.47 g then increases to reach a maximum value of 12.4 g after 60 s. CEBR4 6%, we observe an increasing absorption up to 12 s and then becomes constant up to 28 s with a constant value of 5.9 g and then increases to reach a maximum value of 13.11 g after 58 s.

We also note that CEBR1 0% is the CEB that has the minimum mass of water absorbed after 58 s of immersion and CEBR4 6% is the CEB that has the maximum mass of water absorbed after 58 s of immersion. These results clearly show that the presence of rattan fibers in earth bricks increases the water absorption rate as the fiber percentage increases. This increase in the water absorption rate may be linked to the fact that the more fibers are added to the CEB, the more interstitial voids are created, promoting water infiltration [15,31]. According to the works of Sédan [28] which classifies CEBs according to their stress and their absorption rate, we observe that for our CEBs the maximum absorption rate (10.76%) is lower than the absorption rate of 15% for water actions by vertical penetration. Therefore, it is suitable for construction. In general, the less water absorption of a block, the better its mechanical performance [30], which is why CEBR2 2% has the best mechanical characteristics of CEBs. It is also necessary to point out here the importance of the effect of compaction stress on water absorption because soil compaction modifies its density, mechanical strength, permeability, and porosity [32].

4. Conclusion

The objective of this research was based on the characterization of the physical and mechanical properties of raw earth bricks reinforced with rattan fibers. In this research, we were interested in improving the performance (physical and mechanical) of the CEB, by exploiting local materials: earth taken from the western region of Cameroon, more precisely from the city of Bangangté, and plant fiber, particularly rattan, which constitutes one of the plant riches all over the world that is still neglected today. To achieve our objective, we first characterized the soil used (natural water content, granulometric analysis, Atterberg limits and the standard proctor test) in order to determine whether this soil is suitable for use in the manufacture of CEBs. Then, different test specimens are made with different proportions of rattan fibers. Finally, we carried out mechanical tests (flexural strength and compressive strength) and physical tests (density and water absorption rate). According to the results of the physical characterization of the soil used, the water content of the soil is determined, as well as the granulometric analysis, showing that the soil is not rich in very fine elements and has mostly grains with moderate diameters. Then the Atterberg limits, the liquidity limit, the plasticity limit and the plasticity index are found. The different results on the Atterberg limits show that the soil considered was low-plastic organic silt according to the USCS and following the values of WL, WP, and IP they fell within

the standards for CEBs. As for the mechanical characterization of CEBs, the mechanical tests showed that rattan fiber improves the flexural and compressive strengths. Both in bending and compression, the CEBs stabilized calamus fiber reach maximum resistances at the same rate of fiber. For the water absorption rate, one also notices that the more the percentage of fiber increases the more the CEBs absorb water with a maximum absorption coefficient found, which complies with the standard. According to the density, it decreases with the percentage of fibers. From these obvious results, the addition of rattan fiber in compressed earth blocks improves both the mechanical properties of earth bricks and their sensitivity to water. Thus, the presence of rattan fibers in the manufacture of compressed earth bricks is an asset if the selection criterion is its resistance.

According to the results obtained from this research and with a view to a future rational and efficient use of these materials, it would be very useful to further study in the sense of environmental safety, the hydrothermal behavior of CEBs with the addition of rattan fibers; to complete physical characteristics such as: impact resistance, capillary potential, durability. It would also be interesting to study the hydrophilic properties of the fibers or their surfaces which can be irregular and would trap water molecules, which is possible by showing the microstructure of the fibers under an electron or optical microscope. These steps constitute a perspective for future investigations

Author contributions: Conceptualization, FK, RE and OLT; methodology, FK, OLT, SHWW and EYB; software, EF, AT and SHWW; validation, FK, MS, EYB and SN; formal analysis, FK, OLT and AT; investigation, RE and SHWW; data curation, FK, OLT, EF and MNN; writing—original draft preparation, FK, RE, SHWW and MNN; writing—review and editing, FK, RE, OLT, MNN, EF, AT, SHWW, MS, EYB and SN; supervision, EF, MS, EYB and SN; project administration, FK and OLT. All authors have read and agreed to the published version of the manuscript.

Conflict of interest: The author declares no conflict of interest.

References

1. Aduwo EB, Ejale EA, Ibem EO. Contemporary Shelter in the Built Environment: A Comparative Review of Social Housing Schemes in Selected European and African Nations. IOP Conference Series: Earth and Environmental Science. 2022; 1054(1): 012027. doi: 10.1088/1755-1315/1054/1/012027
2. Hotouom LMT. Identification, analysis, evaluation and possible solutions of the problem of housing in Cameroon: Case study of Douala and Yaounde. University of Stellenbosch Business School; 2015. doi: 10.13140/RG.2.1.4203.4644
3. Banakinao S, Drovou S, Lolo K, et al. Shear Resistance of Siltous Sands Improved with Bridelia Tannins. Geomaterials. 2024; 14(01): 1-11. doi: 10.4236/gm.2024.141001
4. Boutarfa M, Belouettar R, Makradi A. Comparative Study of Cement Mortar Reinforced with Vegetable Fibers Alfa, Date Palm and Diss: Mechanical Properties and Shrinkage. Journal of Materials and Environmental Science. 2018.
5. Guillaud H, Doat P, Rollet P, et al. Technologie de construction et architecture de terre. In: Proposition de directions prioritaires de recherche pour la République de Corée: Rapport final (Volume 1/2): Analyze de l'état de l'art au niveau international et national et Proposition de directions prioritaires de recherche. Université Nationale de Mokpo; 2008.
6. Doat P, Hays A, Houben H, et al. Building with soil. Paris, Editions Parenthèses, collection An Architecture, Paris, France, 1979.
7. Houben H, Gillard H. Treatise on earth construction, 3rd ed. Marseille: Editions Parenthèses, Marseille, France; 2006.

8. Taallah B. Study of the physico-mechanical behavior of compressed soil blocks with fibers. Materialstoday Proceedings; 2022.
9. Alves De Azeredo G. Development of mechanical test procedures on soil mortars: Application to the study of their rheology [PhD thesis]. National Institute of Applied Sciences, Lyon, Germany; 2005.
10. Kouakou CH. Valorization of clays from Côte d'Ivoire: study of the cold stabilization of Dabou clay with a hydraulic binder (Portland cement) [PhD thesis]. University of Cocody, Abidjan; 2005.
11. Kouadio KC. Development and characterization of cement-stabilized clay blocks (Cimarg): Influence of the addition of degreaser on the physical and mechanical characteristics of the blocks [PhD thesis]. University of Cocody, Abidjan; 2010.
12. Ouattara S. Research of lightweight bricks: design and characterization of raw bricks based on clay and sawdust, stabilized with portland cement [PhD thesis]. University of Abidjan; 2013.
13. Swamy RHS, Ahuja BM, Krishamoorthy YS. Behavior of concrete reinforced with jute, coir, bamboo fibers. The international journal of cement composite and light weight concrete. 1984; 5: 13. doi: 10.1016/0262-5075(83)90044-1
14. Ntom Nkotto LI, Dounbissi Kamgang G, Tiewa J, et al. Characterization of blocks produced by addition of coconut fibers and cement laterite-based building materials. Afrique Science; 2020.
15. Danso H, Martinson DB, Ali M, et al. Physical, mechanical and durability properties of soil building blocks reinforced with natural fibres. Construction and Building Materials. 2015; 101: 797-809. doi: 10.1016/j.conbuildmat.2015.10.069
16. André A, Ahoudou NN, Benjamin B, et al. Effects of oil palm mesocarp fibers on the physical and mechanical properties of expansive soils. World Journal of Advanced Research and Reviews. 2024; 22(1): 794-811. doi: 10.30574/wjarr.2024.22.1.1095
17. Google earth. Availbale online: https //www…in line (accessed on 22 April 2024).
18. Nfornkah BN, Enongene K, Kaam R, et al. Spatial distribution of rattan and indigenous perspectives vis-à-vis the growth rate of economically important rattan species in Cameroon: Sustainability and policy implications. Current Research in Environmental Sustainability. 2022; 4: 100151. doi: 10.1016/j.crsust.2022.100151
19. NF (French Standard) EN ISO 17892-1. Geotechnical reconnaissance and testing—Laboratory tests on soils—Part 1: Determination of water content. OBP; 2014.
20. NF EN ISO 17892-4. Geotechnical reconnaissance and testing—Laboratory tests on soils—Part 4: Determination of particle size distribution. OBP; 2018.
21. NF EN ISO 17892-12. Geotechnical reconnaissance and testing—Part 12: Determination of liquidity and plasticity limits. OBP; 2018.
22. CN 102-114. Terminology and Classification of CEB. OBP; 2006.
23. AFNOR. NFP94-093. Soils: Recognition and testing—Determination of the compaction references of a material—Normal Protor test. Modified Protor test; 1999.
24. Michel J. Study on the stabilization and compression of soil for their use in construction, Annals of the Technical Institute of Building and Public Works. Materials Series; 1999.
25. ASTM C 20. Standard Test Methods for Apparent Porosity, Water Absorption, Apparent Specific Gravity, and Bulk Density of Burned Refractory Brick and Shapes by Boiling Water. International; 2000.
26. NFP94-051. Atterberg limits. Normes nationales et documents normatifs nationaux; 1993.
27. NC 102-114. Terminology and Classification of CEB. Normes nationales et documents normatifs nationaux; 2006.
28. Djohore CA, Djomo SA, et al. Effect of the addition of potash-treated coconut fibers on the mechanical properties of clay-cement-based construction materials, Edition. European Scientific Journal. 2018.
29. Ouedraogo KAJ. Stabilization of sustainable and ecological building materials based on raw earth by organic and/or mineral binders with low environmental impacts [PhD thesis]. Toulouse 3 Paul Sabatier University (UT3 Paul Sabatier); 2019.
30. Sédan D. Study of physicochemical interactions at hemp fiber/cement interfaces. Influence on the mechanical properties of the composite [PhD thesis]. University of Limoges, Germany; 2007.
31. LE Trode M. Characterization of physicochemical interactions in a composite material based on phyllosilicates, lime and cellulose fibers [PhD thesis]. University of Limoges, Germany; 2009.
32. Abessolo D, Biwole AB, Fokwa D. Effects of the length and content of bamboo fibers on the physic mechanical and hygroscopic properties of compressed soil blocks used in construction Abstract. Afrique Sci; 2020.

Appendix

Table A1. Granulometric analysis by sieving.

Φ Sieve mm	Partial refusals (g)	Cumulative refusals (g)	% Cumulative refusals	% Cumulative sieves
10	0	0	0.00%	100.00%
5	208.42	208.42	8.33%	91.66%
4	130.43	338.85	13.55%	86.44%
2.5	204.24	543.09	21.72%	78.27%
1.6	213.61	756.7	30.26%	69.73%
1.25	149.13	905.83	36.23%	63.76%
0.63	289.82	1195.65	47.82%	52.17%
0.315	395.06	1590.71	63.62%	36.37%
0.2	240.61	1831.32	73.25%	26.74%
0.16	115.27	1946.59	77.86%	22.13%
0.08	437.5	2384.09	95.36%	4.63%
Bottom	86	2470.09	98.80%	1.19%

Table A2. Atterberg limits.

Liquidity limit				**Plastic limit**	
Number of blows	15	20	30		
Tare number	01	02	03	01	02
Tare mass (g)	111.4	67.98	111.21	68.16	28.72
Total wet mass (g)	132.16	91.9	132.51	73.5	32.98
Total dry mass (g)	124.87	84.22	125.54	72.15	31.87
Water mass (g)	7.13	8.01	6.84	1.35	1.11
Dry soil mass	13.56	15.90	14.45	3.99	3.15
Water content W (%)	52.54	50.39	47.35	33.83	35.23
Average	50.09				

Table A3. Results of the standard proctor test at 10% water.

Water Content			**Sample**			
Tare n°	**Dry soil mass (g)**	**Water content**	**Volume (cm3)**	**Wet soil mass (g)**	**Wet density (g/cm3)**	**Dry density (g/cm3)**
1	119.51	25.65	942.14	1270	1.348	1.0729
2	119.63	25.43	942.14	1270	1.348	1.0748
3	120.67	24.38	942.14	1270	1.348	1.0839
Average water content = 25.15 %			Average dry density = 1.0772g/cm3			

Table A4. Results of the standard proctor test at 12% water.

Water Content				**Sample**		
Tare n°	**Water mass (g)**	**Dry soil mass (g)**	**Water content**	**Wet soil mass (g)**	**Wet density (g/cm3)**	**Dry density (g/cm3)**
1	31.44	118.79	26.46	1370	1.454	1.1499
2	31.51	118.63	26.56	1370	1.454	1.1491
3	32.15	117.93	27.26	1370	1.454	1.1428
Average water content = 26.76%				Average dry density = 1.1473g/cm3		

Table A5. Results of the standard proctor test at 14% water.

Water Content				**Sample**		
Taren°	**Water mass (g)**	**Dry soil mass (g)**	**Water content**	**Wet soil mass (g)**	**Wet density (g/cm3)**	**Dry density (g/cm3)**
1	34.11	115.97	29.41	1570	1.666	1.2878
2	35.05	115.06	30.46	1570	1.666	1.2775
3	34.3	115.93	29.58	1570	1.666	1.2861
Average water content = 29.82%				Average dry density = 1.2838g/cm3		

Table A6. Results of the standard proctor test at 16% water.

Water Content				**Sample**		
Tare n°	**Water mass (g)**	**Dry soil mass (g)**	**Water content**	**Wet soil mass (g)**	**Wet density (g/cm3)**	**Dry density (g/cm3)**
1	35.81	114.41	31.29	1695	1.799	1.3704
2	36.27	113.97	31.82	1695	1.799	1.3649
3	37.05	113.12	32.75	1695	1.799	1.3554
Average water content = 31.95%				Average dry density = 1.3636/cm3		

Table A7. Results of the standard proctor test at 18% water.

Water Content				**Sample**		
Tare n°	**Water mass (g)**	**Dry soil mass (g)**	**Water content**	**Wet soil mass (g)**	**Wet density (g/cm3)**	**Dry density (g/cm3)**
1	37.38	112.64	36.19	1530	1.62	1.2224
2	36.48	113.54	36.13	1530	1.62	1.2351
3	37.19	112.84	36.30	1530	1.62	1.2236
Average water content = 36.20%				Average dry density = 1.2270/cm3		

Table A8. Summaries of bending forces and stresses at 7 days.

%	**F1**	**F2**	**F3**	**Average**	**CONTRAINT**
CEBR1 0%	115.236	86.887	110.218	104.1137	0.244016
CEBR2 2%	196.447	234.666	120.571	183.8947	0.461003
CEBR3 4%	354.654	73.644	114.342	180.88	0.423938
CEBR4 6%	100.425	186.639	113.456	133.5067	0.312906

Table A9. Summary of bending forces and stresses at 14 days.

%	F1	F2	F3	Average	CONTRAINT
CEBR1 0%	116.603	213.503	226.100	185.402	0.434536
CEBR2 2%	155.363	305.235	393.414	284.6707	0.667197
CEBR3 4%	252.909	197.03	353.685	267.8747	0.627821
CEBR4 6%	208.981	233.852	322.354	255.0623	0.597802

Table A10. Summary of bending forces and stresses at 28 days.

%	F1	F2	F3	Average	CONTRAINT
CEBR1 0%	253.878	276.488	241.604	257.3233	0.603102
CEBR2 2%	372.742	369.189	160.854	300.9283	0.705301
CEBR3 4%	215.118	214.149	370.481	266.5827	0.644803
CEBR4 6%	269.059	356.269	172.159	265.829	0.623037

Table A11. Summaries of compressive forces and stresses at 7 days.

%	F1	F2	F3	Average	CONTRAINT
CEBR1 0%	3040.065	2859.913	1711.444	2537.141	1.5857129
CEBR2 2%	4143.496	3467.926	3467.926	4218.559	2.6365995
CEBR3 4%	4323.648	2949.989	4211.053	3828.23	2.3926437
CEBR4 6%	2251.9	1959.153	3558.002	2589.685	1.6185531

Table A12. Summaries of compressive forces and stresses at 14 days.

%	F1	F2	F3	Average	Stress
CEBR1 0%	3985.863	2338.268	2210.570	2844.9	1.778063
CEBR2 2%	5697.307	4616.395	3783.192	4698.965	2.936853
CEBR3 4%	3332.812	3625.559	4683.952	3880.774	2.455484
CEBR4 6%	1598.849	3400.369	5156.851	3385.356	2.115848

Table A13. Summary of compressive forces and stresses at 28 days.

%	F1	F2	F3	Average	Stress
CEBR1 0%	3152.66	4661.433	2274.419	3362.837	2.101773
CEBR2 2%	4323.648	5134.332	5179.37	4879.117	3.049448
CEBR3 4%	5382.041	3940.825	3895.787	4406.218	2.753886
CEBR4 6%	4120.977	3895.787	4774.028	4263.597	2.664748

Table A14. 14-day density summaries.

% CEB	Mass (g)	Volume (cm3)	Density (g/cm3)
CEBR1 0%	567.17	256	2.215507813
CEBR2 2%	563.66	256	2.201796875
CEBR3 4%	536.98	256	2.097578125
CEBR4 6%	525.08	256	2.05109375

Table A15. 28-day density summaries.

% CEB	Mass (g)	Volume (cm3)	Density (g/cm3)
CEBR1 0%	548.26	256	2.141640625
CEBR2 2%	499.97	256	1.953007813
CEBR3 4%	485.28	256	1.895625
CEBR4 6%	440.06	256	1.718984375

Table A16. Summary of the different masses of water absorbed at 28 days.

	Dry mass (g)			
	257.56	**285.61**	**254.21**	**304.13**
	Mass of water absorbed (g)			
Time (s)	**0%**	**2%**	**4%**	**6%**
2	0.54	1.63	2.41	0.79
4	1.11	2.5	2.41	1.66
6	1.59	3.17	2.44	2.47
8	2.09	3.64	2.45	3.27
10	2.55	4.12	2.46	3.96
12	4.35	5.84	2.47	5.76
14	4.36	5.85	4.11	5.77
16	4.38	5.85	4.38	5.78
18	4.38	5.86	4.68	5.79
20	4.39	5.87	5.07	5.8
22	4.4	5.88	5.36	5.81
24	4.41	5.89	5.77	5.81
26	4.42	5.89	6.06	5.82
28	4.43	5.9	6.42	5.83
30	6.37	5.91	6.99	7.92
32	6.71	7.54	7.47	8.13
34	7.01	7.9	7.62	8.44
36	7.3	8.16	7.89	8.83
38	7.62	8.38	8.18	9.31
40	7.88	8.57	8.45	9.69
42	8.04	8.64	8.75	9.81
44	8.22	8.83	8.88	10.29
46	8.24	9.04	9.19	10.61
48	8.56	9.2	9.39	11.09
50	8.71	9.32	9.67	11.28
52	9.02	9.39	9.86	12.77
54	9.44	9.58	10.09	12.31
56	9.04	9.87	10.4	12.92
58	9.34	9.98	10.62	13.11

Materials Technology Reports 2024, 2(1), 1654.
https://doi.org/10.59400/mtr.v2i1.1654

Article

Comparative study of fibers extracted from the stems and roots of the Cameroonian pennissetum purpureum for their applications in compressed earth brick reinforcement and textile engineering

Fabien Kenmogne[1,*], Roger Eno[2], Adoum Danao Adile[3], Blaise Ngwem Bayiha[1], Gilbert Tchemou[1], Martial Nde Ngnihamye[4], Olivier Lekeufack Tiokeng[5], Steven Kevin Donfang Nobisse[1], Emmanuel Yamb Bell[1]

[1] Department of Civil Engineering, Advanced Teacher Training College of the Technical Education, University of Douala, Douala 1872, Cameroon
[2] Laboratory E3M, National higher polytechnic School of Douala, The University of Douala, Douala 2701, Cameroon
[3] Department of Industrial Engineering and Maintenance, Polytechnic University of Mongo, Mongo 4377, Chad
[4] Department of Civil Engineering, National Advanced School of Public Works, Yaoundé 510, Cameroon
[5] Department of Physics, Faculty of Sciences, University of Douala, Douala 24157, Cameroon
*** Corresponding author:** Fabien Kenmogne, kenfabien@yahoo.fr

CITATION

Kenmogne F, Eno R, Adile AD, et al. Comparative study of fibers extracted from the stems and roots of the Cameroonian pennissetum purpureum for their applications in compressed earth brick reinforcement and textile engineerings. Materials Technology Reports. 2024; 2(1): 1654. https://doi.org/10.59400/mtr.v2i1.1654

ARTICLE INFO

Received: 26 April 2024
Accepted: 30 June 2024
Available online: 14 June 2024

Abstract: This work focuses on the extraction and experimental characterization of pennisetum purpureum fibers extracted from stems and roots, harvested in the Batié Kingdom, in the West Region of Cameroon. After extracting fibers using the boiling water technique, they are chemically treated to improve their properties and performance and to facilitate their incorporation into various composite materials. For the physical characterizations, it is measured: the absolute and apparent densities, the linear mass, the water absorption rate, and the diameter via the microscope. The mean values of the diameters and the measure of their frequency distributions are calculated, followed by the statistical analysis using the maximum entropy principle, in order to find the most probable diameter necessary for technological applications. For the mechanical properties, only the tensile tests are performed, with the determination of the young modulus of both the stems and roots. The results thus obtained showed that the fibers of the stems have an absolute density of (1.35 g/cm^3), a linear mass of (54.6 tex), an apparent density of (0.45 g/cm^3), a water content of (12.73%), an absorption rate of (142.46%), a porosity of (65.91%), a mean diameter of (7 mm), an elastic modulus of (3.98 GPa), a tensile strength of value of (1186.59 MPa) and an elongation of 16.17%, while the root fibers have an absolute density of (1.34 g/cm^3), a linear mass (16.76 tex), an apparent density of (0.37845 g/cm^3), a water content of (12.25%), an absorption rate of (193.16%), a porosity of (71.92%), a diameter of (4 mm), an elastic modulus of (1.55 GPa), a tensile strength of a value of (1960.35 MPa) and an elongation of 60.6%. Thus, the fibers of the stems have good mechanical properties, which make them an appropriate material in several applications, such as the reinforcement of composite materials.

Keywords: pennisetum purpureum; stem and root fiber; boiling water extraction; physical and mechanical characterization

1. Introduction

The rise of green technologies and the growing need for sustainable materials in the construction sector have sparked significant interest in harnessing renewable and eco-friendly resources [1]. Among these resources, natural fibers are emerging as a promising alternative to traditional synthetic materials because they have many advantages, such as biodegradability, renewability, wide availability, low density

and low cost which provide greater opportunities to develop a new class of lightweight and eco-friendly natural fiber composites [2]. There are a wide variety of natural fibers that can be applied as reinforcements. The most used are linen, hemp, jute, kenaf and sisal, due to their properties and availability [3]. Some recent scientific works have shown the possibility of using other natural fibers as reinforcement for composite materials. Thus, Pennisetum purpureum (PP) commonly known as Napier grass or elephant grass, as we shall see further, presents itself as an ideal candidate due to its rapid growth, its adaptation to varied climatic conditions and its availability. PP is a monocotyledonous flowering plant belonging to the Poaceae family (the grass family) and the Pennisetum genus [4]. Pennisetum is a very diverse genus composed of a heterogeneous group of approximately 140 species [5]. It is used for the control of soil erosion [6]; resistance to a broad spectrum of pests and diseases [7]; and suitability for cellulosic biofuel production. It can then be used to make fences, as windbreaks, to demarcate boundaries between neighboring farmers, and the dried materials can be used as a fuel source [8]. In cropland management systems, it is used as a mulch to control weed infestation and soil erosion and as a trap plant in the push-pull strategy, a pest control practice that uses repellent plants and an attractive plant trap for insect pest control in Africa, particularly against the corn borer [9]. PP plants are also used to remove pollutants, such as heavy metals, and have been used in phytoremediation strategies, for example to clean up cadmium-affected soils, reducing the concentration of cadmium to a depth of 15 cm in the soil [10]. The only technique used until now to extract fibers from this plant was cold water retting. This is a technique that allows the fibers to be extracted after two weeks of soaking [11]. This technique is time consuming and there is a risk of air pollution due to the strong odor released, which can cause illness. Some authors have used an alternative extraction technique for other plant species using boiling water [12]. The studies of these authors showed that the boiling water technique allows rapid extraction of fibers without weakening their properties. In this present study the fibers are extracted from the stems and roots of the PP plant by the boiling water extraction method.

The characterization of fibers is an essential process that allows defining their physical and mechanical properties. These fibers, such as those extracted from plants such as PP, have been studied because of their potential to replace or complement synthetic fibers. The characterization of these fibers is therefore a step towards their successful integration into existing and new applications, allowing optimal exploitation of their unique properties. The physical characterization includes density, porosity, water content, water absorption rate and linear mass, allowing us to understand their behavior in various applications. At the same time, the mechanical characterization, including tensile strength, modulus of elasticity and elongation at break, provides valuable information on the capacity of these fibers to improve the properties of composites, particularly in terms of resistance to cracking and ductility. A few studies have been carried out by some researchers on the characterization of fibers derived from plant sources such as banana, sugarcane bagasse, Brazilian sponge gourd, Shwetark stem and raffia palm [13–20]. Such studies are being conducted worldwide to substantiate their potential for use in construction, packaging, sporting goods, furniture and lightweight applications.

The industrial use of fibers derived from natural plants as reinforcements in materials began in the early 20th century with the manufacture of large quantities of sheet metal, tubes and pipes for electronic purposes. One also has the seats, fuel tanks, the interior equipment and exteriors of automobiles [21,22], the manufacturing of fabrics, packaging, the manufacturing of high-strength paper or cardboard, the manufacturing of panels, the creation of art objects due to their excellent characteristics. To our knowledge, fibers from PP stems and roots have not yet been used in such applications. Thus, the major problem solved is to determine which of the stem and root fibers of PP have favorable properties for the creation of durable, profitable and environmentally friendly material. Let us remember that in [23] the fiber from the PP studied is extracted only from the stems, while in the present work, both fibers from the stems and roots are studied and compared. Moreover, it is the pioneering work for the Cameroonian PP, which is new since the properties of plants can vary according to geographic location and climate change. In addition, we use the statistical approach, usually used in energetic physics to evaluate the most probable fiber diameter to find the more realistic wind speed, which is new in the context of natural fibers. To address this theme, we seek to provide elements of answers to the following research questions:

- Do PP fibers have favorable physical and mechanical properties for reinforcing compressed earth bricks (CEBs)?
- Do the fibers extracted from different parts of the PP have different mechanical properties, thus influencing their performance in the CEBs?
- What would be the economic, environmental, and structural advantages of using PP fibers compared to other reinforcing materials in the construction of CEBs? The specific objectives of our work are:
- Determine the physico-mechanical properties of fibers from PP stems and roots.
- Identify the most efficient extraction method for obtaining PP fibers.
- Compare the costs and environmental benefits linked to the use of PP fibers compared to other methods of reinforcing CEBs.

2. Materials and methods

Mastery of the materials and techniques used to properly carry out the study on the extraction and physico-mechanical characterization of fibers from PP stems and roots is of capital importance. This section describes all the methods and techniques used as part of our study as well as the materials and means implemented. After the extraction of the fibers and the collection of the different samples to be studied, we proceeded in turn to the physical characterization, to the mechanical characterization of the treated samples then to the presentation of the different tests carried out.

2.1. Origin of the material used and extraction site

2.1.1. Origin of the material used

PP is native to Africa, but has spread to many tropical and subtropical regions of the world. It is a perennial herb that can reach an impressive size of up to 3–4 m in height [24]. It is distinguished by its long, narrow leaves and feather-shaped purple

or light brown inflorescences. **Figure 1** shows the distribution of this material across the world.

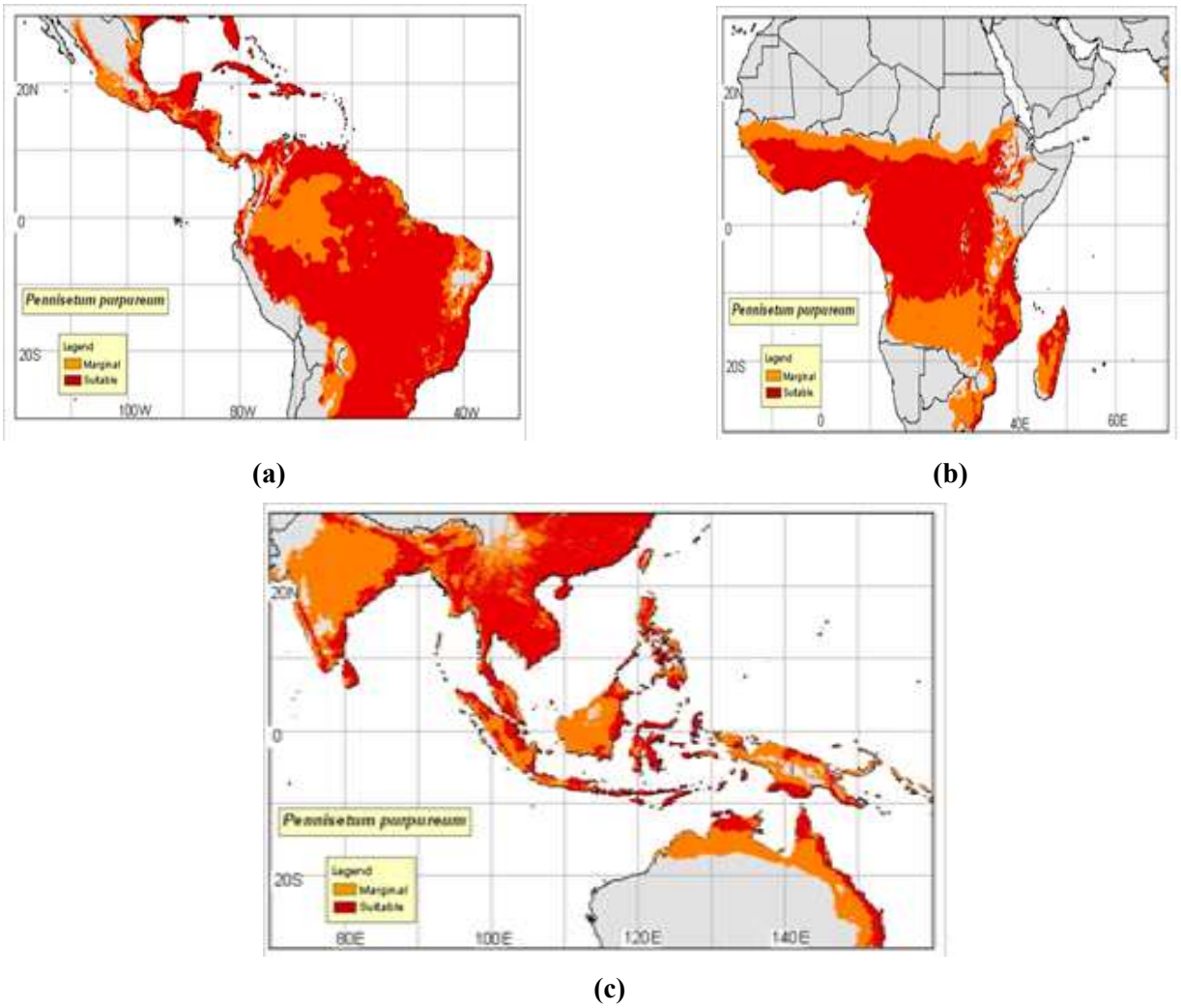

Figure 1. Distribution of PP in the world [24]. **(a)** Distribution in Caribbean, Central and Southern America; **(b)** distribution in Africa; **(c)** distribution in Melanesia, Southeast Asia and Surrounding regions.

2.1.2. Extraction site

The PP samples used come from the western region of Cameroon, more precisely in the Batié kingdom, in the Femgoum district. This Batié kingdom as shown in **Figure 2** is part of the large geographical area commonly called “the highlands of western Cameroon”. It is one of the traditional chiefdoms of the western Cameroon region located on the national road No 2 to 210 km from Douala and 30 km from Bafoussam, the capital of the region. It is chosen based on its availability and abundance in the region.

Figure 2. Location of the study area in Batié.

2.2. PP fiber extraction process and chemical treatment

2.2.1. PP fiber extraction process

In the present work, we study two elements: the stems and roots of the PP plant. **Figure 3** illustrates the plant under consideration.

Figure 3. PP plants showing their stem and root.

For this study, we opted for the chemical extraction method, as shown in **Figures 4** and **5**, because the execution time is relatively short and the process is hygienic. Firstly the stems are cut to the same lengths as well as the roots, ridding them of any impurities (**Figure 4**) and then introducing them in turn into a metal container and bringing them to a boil at a temperature of 100 °C for 1 h 30 min.

After this duration, one observes that the stems and roots have become soft and the fibers have been isolated from the stems and roots. The separated fibers were carefully washed under running tap water to remove any impurities (See **Figure 5**).

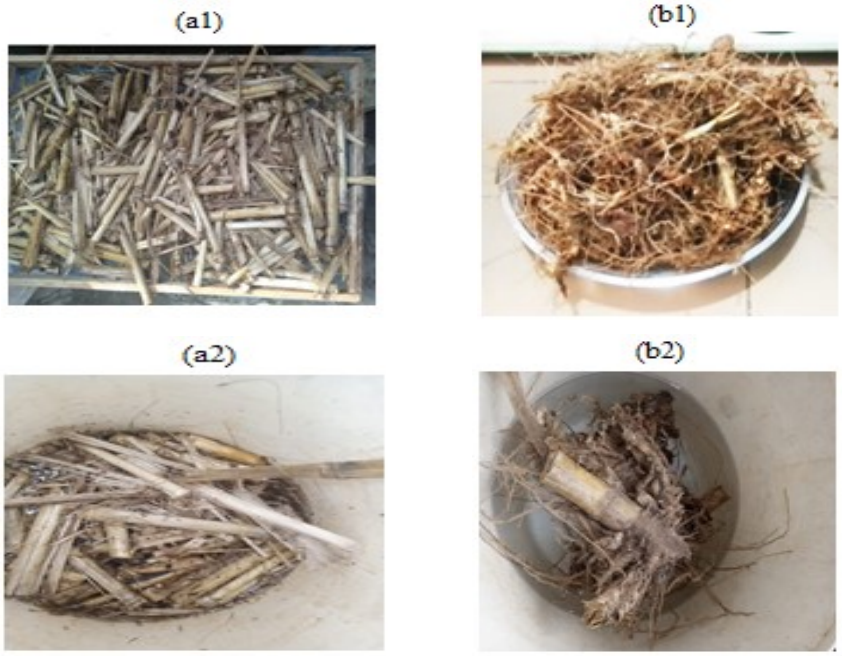

Figure 4. Cleaning stems and roots. **(a1)** and **(b1)** Stems and roots before any treatment; **(a2)** and **(b2)** Stems and roots cleaned.

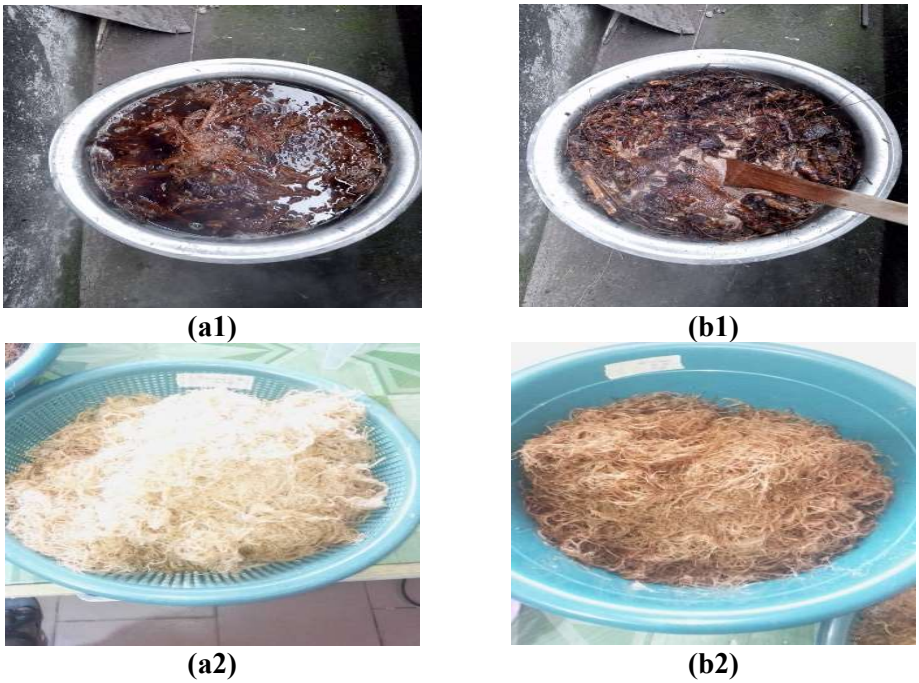

Figure 5. Fiber extractions. **(a1)** and **(b1)** cooking of the stems and roots; **(a2)** and **(b2)** Fibers obtained for the stems and roots.

2.2.2. Chemical treatment of fibers

It is a process that is generally carried out to improve the properties and performance of fibers as well as to facilitate their incorporation into various composite materials. The PP fibers were treated with sodium hydroxide (NaOH) solution. They are dehydrated in an oven at 60 °C for 24 h, and then weighed on a 0.001 g precision balance. Then they were immersed in distilled water and a 10% concentration of NaOH for one hour at a temperature of 105 °C. Then, the fibers were neutralized using a 0.001% acetic acid solution to obtain a PH = 7 (neutral) followed by water, and then the fibers were dried at 100 °C for 24 h. Finally, the fibers were dried in the open air for 24 h. Then stored in an oven for 24 h at 105ºC to ensure maximum moisture removal.

2.3. Determination of physical properties

2.3.1. Absolute density

The test aims to determine the natural density of a material. This test provides information on the internal structure of the fibers. The density of the fibers was carried out by the pycnometric method using ethanol ($\rho_{\text{eth}} = 0.789\text{g/cm}^3$ in a room with a temperature of 27.4 °C) as immersion liquid, in accordance with standard NF EN 1097-6. Before the measurements, 03 fiber samples were dehumidified in an oven at a temperature of 105 °C for a minimum of 6 h. Measurements were made using a balance with a sensitivity of 0.1 mg and the following equation was applied to calculate the density ρ.

$$\rho_{abs} = \frac{m_0 \times \rho_{eth}}{m_0 + m_1 - m_2} \quad (1)$$

where

- m_0 (g) is the mass of the anhydrous sample;
- m_1 (g) is the mass of the pycnometer + ethanol assembly;
- m_2 (g) is the mass of the pycnometer + ethanol + sample assembly

2.3.2. Linear mass

Also called a measurement of the title (in tex) or the fineness of the fibers, this test aims to determine the mass per unit length of PP samples.

The linear mass of our fibers was determined gravimetrically according to the ISO 1973 2021 edition standard in a room with a temperature of 27 °C. To prepare the samples, they are first dehydrated in a ventilated oven at 105 °C for 24 h. Then five 5 mm samples are taken using a chisel and a ruler, and conditioned for 24 h in a desiccator whose hygrometry is 65% relative humidity. After 24 h of conditioning, the samples are taken and weighed on a 1 mg precision balance. The following equation was used to calculate the linear mass.

$$M_L(tex) = \frac{m(\text{g})}{L(\text{Km})} \quad (2)$$

where m (g) is the mass of the wire of length 1 m; L (km) is the length of the wire in km; $M_L(tex)$ is the calculated linear mass.

2.3.3. Apparent density

The purpose of this test is, to determine the compactness and porosity of our fibers. The apparent density of our fibers was determined according to standard NF EN 1097-3 (August 1998 Edition) in a room with a temperature of 27 °C. To obtain 03 samples, they are first dehydrated in a ventilated oven at 105 °C for 24 h. Then we carry out four successive weighings:

- The mass of the anhydrous sample m_0 (g);
- The mass of the assembly (pycnometer + distilled water) m_1 (g);
- The mass of the assembly (pycnometer + distilled water + fiber) after saturation m_2 (g);
- The mass of the saturated fiber with dry surface m_3 (g);
- The apparent density of the fiber is obtained from the formulas below:

$$\rho_{app} = \frac{m_0 \times \rho_{\text{water}}}{m3 + m1 - m2} \tag{3}$$

2.3.4. Water content

The purpose of the humidity level is to determine the quantity of water contained in our fibers; it is expressed as a percentage of the mass of the wet product. Three fiber samples with an initial dryness mass of $m_1 = 1 \pm 0.1$ g were weighed using a balance with a sensitivity of 0.001 g, and then dried in a ventilated oven for 24 h at a temperature of 105 °C. After drying, the mass m_2 was recorded using the balance, and the following equation was used to determine the humidity level according to the ISO 3344:1997 standard (room temperature: 27.6 °C).

$$W(\%) = \frac{(m_1 - m_2)}{m_1} \times 100 \tag{4}$$

where m_1 is the initial mass of the sample (g); m_2 the final mass of the sample (g).

2.3.5. Water absorption rate

The purpose of the current test is to determine how much water the fibers can absorb.

The test was carried out according to standard NF EN 1097-6 (room temperature: 27.4 °C). The samples were dried in an oven at 105 °C temperature, for a minimum of 6 h to make them anhydrous. Then, the fibers were weighed using a balance with a sensitivity of 1 mg to obtain their different initial masses. Finally, these samples (m_0) are introduced into pycnometers which are then filled with water up to 0 of the meniscus. After 24 h, the samples are extracted from the pycnometers, and the surface water is taken using a device to filter and extract the surface water. The saturated fibers at the dry surface are therefore weighed to obtain the mass mf. The following equation was used to determine the water absorption rate:

$$\text{Ab}(\%) = \frac{(m_f - m_0)}{m_0} \times 100 \tag{5}$$

2.3.6. Diameter under the microscope

$$\emptyset_{\text{moy}} = \frac{\sum_{i=1}^{5} \emptyset_i}{5}, \tag{6}$$

where $\emptyset_{\text{moy}}$: Average diameter; $\emptyset_i$: Diameter at point 'i'. Since we are dealing with natural samples, we will observe a variation in diameter for each sample of these fibers (See **Figure 6**). In order to determine the most probable diameter of our fibers we will proceed as follows:

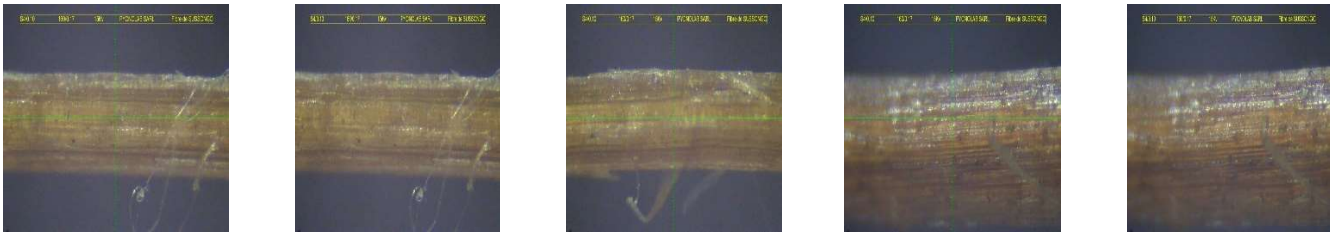

(a) **(b)** **(c)** **(d)** **(e)**

Figure 6. Measurement of fiber diameters. **(a)** Sample 1; **(b)** Sample 2; **(c)** Sample 3; **(d)** Sample 4; **(e)** Sample 5.

Determining the average

To do this, we will draw the diagram of the diameters of these fibers according to the different samples then average the 25 samples of each fiber in order to obtain the average value of the diameter of these fibers.

$$\phi_{\text{moy}} = \frac{\sum \phi_i}{N} \tag{7}$$

ϕ_i is the unit diameter; N: is the total number of measurements.

Determining the median

To do this we will first group together in a table the different modal classes of fiber diameter and for each class we will determine its frequency of appearance. Finally, using the linear interpolation method, we will determine the median which will in this case be the value of the diameter.

$$F(\%) = \frac{M}{MT};\ Me = Xa + (Xt - X'a)\frac{Xb - Xa}{X'b - X'a} \tag{8}$$

From where F(%) is the frequency; M: modality; Mt: total modality; Me: the median; Xb−Xa: the modal class; $X'b - X'a$: increasing cumulative frequency; Xt: the total modality.

Statistical analysis using the maximum entropy principle

In order to study the principle of maximum entropy we took as a reference the work carried out by [25]. This study will allow us to determine the probability of appearance of our fibers depending on the diameter of the different samples obtained from our two fibers of the stems and roots. To do this, the probability density function of diameters has been introduced in the following form:

$$f(\phi) = \exp\left(\sum_{j=0}^{N} \alpha_j \phi^j\right) = \exp(\alpha_0 + \alpha_1\phi + \alpha_2\phi^2 + \alpha_3\phi^3 + \cdots) \quad (9)$$

where α_j are the Lagrangian multipliers, while N is the number of the low order moments used, and where P is the irradiance distribution. This density function is obtained by minimizing Shannon's entropy, following the well-known Carla et al principles [26], suggesting the following constraints:

$$\int_0^{\max(\phi)} f(\phi)d\phi = 1, \int_0^{\max(\phi)} \phi f(\phi)d\phi = \bar{\phi} \quad (10)$$

$\bar{\phi}$ being the m-low statistical orders, obtained empirically (as in [26] and references therein).

$$\bar{\phi} = \frac{1}{N}\sum_{j=0}^{N} \phi^j \quad (11)$$

The set of Equations (10) and (11) will be solved numerically, and the parameters α_j substituted into Equation (9) and plotted in the next section to give the probability distribution.

2.4. Determination of mechanical properties: Tensile test

The tensile test measures the maximum tensile strength of a fiber, indicating its ability to support a load without breaking. This information is crucial for assessing the strength and durability of fibers. By analyzing the traction curve, we can evaluate the elastic behavior of the fiber, that is to say its ability to return to its initial shape after being subjected to stress. This provides insight into the flexibility and deformation of the fibers.

The determination of Young's modulus, from strain to fiber breakage was carried out on 25 samples for each fiber, using a universal testing machine at a speed of 2 mm/mi. The fibers were previously dried in an oven at 105 °C for 24 h, then cut to a length of 50 mm, before being placed on a glass slide and measured using an electron microscope. The diameter of the fibers being obtained under a microscope, the fibers are subsequently mounted on cardboard supports, and numbered according to the order of the diameter measurements. Before mounting the samples on the traction device, they are conditioned in a desiccator formulated at 65% relative humidity. After 24 h, the fibers are successively installed on the jaws of the universal testing machine, where an installation tension is applied to them before starting the test. During the test, the Test Master software draws the curves and calculates all the test parameters. The following equations were used to determine Young's modulus, maximum tensile strength, and strain at break:

$$\sigma_{\max} = \frac{F\max}{S}, \varepsilon_{\text{rupt}} = \frac{A_r}{Lo}; E = \frac{\sigma 2 - \sigma 1}{\varepsilon 2 - \varepsilon 1}, \quad (12)$$

where

- Fmax (*N*) is the maximum tensile force;

- S (mm^2) is the section of the specimen;
- A_r (mm) is the elongation at break;
- Lo (mm) is the useful length of the test piece (here 20 mm);
- E (MPa) is the young module;
- σ_{max} (MPa) is the maximum tensile strength;
- ε_{rupt} is the strain at breakage of the specimen.

3. Results and discussion

In this section, it will be a question of presenting the results of all the tests carried out and interpreting them in turn in order to have a clear vision of the properties of these fibers and their abilities to be used in various applications. These results correspond to the average of the different data obtained from each.

3.1. Appearance of fibers extracted and processed from PP stems and roots

According to our observation, it turns out that the fibers obtained after extraction retained their color after treatment with a 10% sodium hydroxide (NaOH) solution, which improved the mechanical properties of our fibers compared to others. However, we encountered difficulties during the process of extracting our fibers. In fact, the fibers harvested fresh, posed a problem during cleaning and segmentation into several batches because of their high density and their water content which was, however, relatively high. We therefore proceed to dry our materials in order to facilitate the process of extracting our fibers at room temperature. This result is in the same direction as that presented in [17] which showed that the treatment of Lemba leaf fibers with 10% NaOH improved thermal stability and tensile mechanical properties [27]. On the other hand, the study carried out in [23] shows that the alkaline treatment at 10%, 12% and 15% reduced the mechanical properties of the fibers studied, that is an elastic modulus with a value of 1.00 ± 0.17 GPa and a tensile strength of 50 MPa. This variation in results may be due to the nature and origin of the fibers studied and the extraction and treatment process used for each fiber. Thus, it is obvious that the extraction and treatment process used in our study are of high quality.

3.2. Absolute density

Table 1 presents the value of absolute densities obtained from the fibers of the stems and roots and calculated according to Equation (1). These results allowed us to draw **Figure 7**.

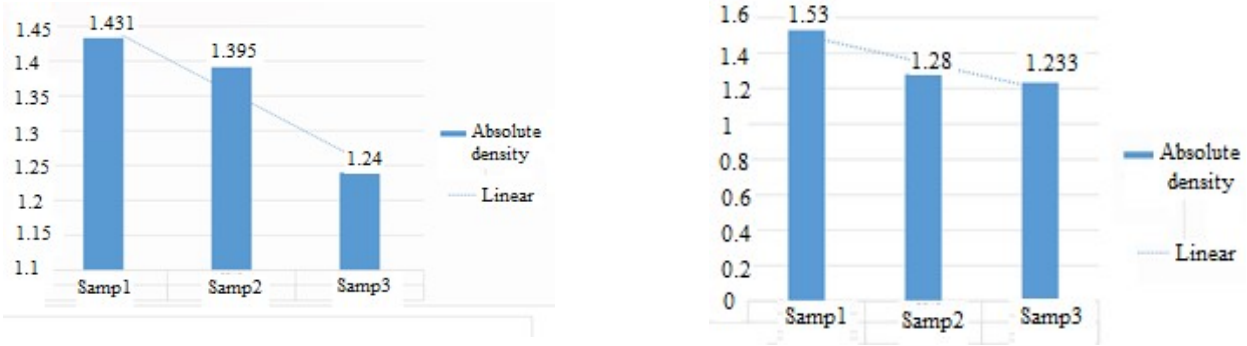

(a) **(b)**

Figure 7. Variation of the absolute density (ρ_{abs}) of fibers. **(a)** stems; **(b)** roots.

Table 1. Absolute density of stem fibers and root fibers.

	Sample 1		**Sample 2**		**Sample 3**	
	stem	**root**	**stem**	**root**	**stem**	**root**
m_0 (g)	1.034	1.006	1.049	1.008	1.011	1.013
m_1 (g)	62.638	62.641	62.409	62.121	62.758	62.228
m_2 (g)	63.103	63.131	62.863	62.509	62.153	62.593
ρ_{abs}	1.431	1.53	1.395	1.28	1.24	1.233

We have on average an absolute density of $1.35\ g/cm^3$ for stem fibers and $1.34\ g/cm^3$ for root fibers. It appears that the stem fibers are slightly denser than the root fibers. These results are identical to those of banana fibers ($1.35\ g/cm^3$) w. Compared to other plants, these fibers have a density higher than that of date fibers ($0.99\ g/cm^3$), coconut fibers ($1.15\ g/cm^3$) and lower than that of sisal fibers ($1.45\ g/cm^3$), flax ($1.53\ g/cm^3$), [28]. Due to their lightweight, stem and root fibers can be used in composite and textile applications.

3.3. The linear mass

Table 2 presents the different values of the linear mass obtained from the stem and root fibers and calculated using Equation (2). These results allowed us to draw **Figure 8**. We have on average a linear mass of $0.0546\ g/cm$ or 54.6 tex for the stem fibers and around $0.01676\ g/cm$ or 16.76 tex for the root fibers. Stem fibers have a higher linear mass than root fibers.

Table 2. Linear mass of stem and root fibers, for the length L = 5 cm.

fibers		**Sample 1**	**Sample 2**	**Sample 3**	**Sample 4**	**Sample 5**
Stem	ml (g)	0.246	0.289	0.254	0.287	0.289
	M_L (tex)	0.0492	0.0578	0.0504	0.0574	0.0578
Root	ml (g)	0.079	0.09	0.105	0.065	0.08
	M_L (tex)	0.0158	0.018	0.021	0.013	0.016

Compared to other plants, these fibers have a higher linear mass than the fibers of sida rhombifolia (SR) (11.23 tex ± 1.1–13.57 tex ±0.95) [11], to that of pineapple

leaf (8.0–8.4 tex) [15]. This variation may be due to the treatment process of our fibers [11] so we can say that our fibers are of good quality.

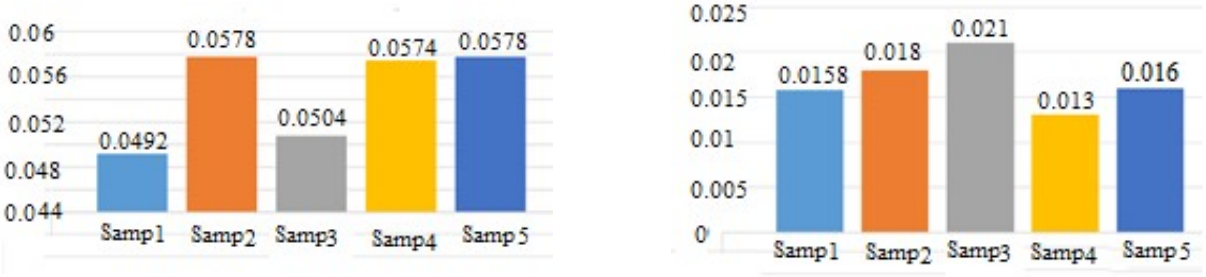

(a) **(b)**

Figure 8. Variation of the linear mass of the fibers. **(a)** Stems; **(b)** Roots.

3.4. Apparent density

Table 3 presents the different values of the apparent density obtained from the stem and root fibers, and calculated according to Equation (3). These results allowed us to draw **Figure 9**. We have on average an apparent density of 0.45 g/cm^3 for stem fibers and 0.37 g/cm^3 for root fibers. Stem fibers have a higher apparent density than root fibers, which means that stem fibers have fewer empty spaces. Compared to other plants, these fibers have a higher apparent density than that of hemp fibers (164.5 kg/m^3), sunflower fibers (20 kg/m^3), esparto fibers (99.4 g/cm^3) [29] and lower than that of amioca fibers (235 to 750 g/cm^3). Leading to the conclusion that the fibers in the stems are of high quality, having implications for the durability and longevity of the end products made from these fibers.

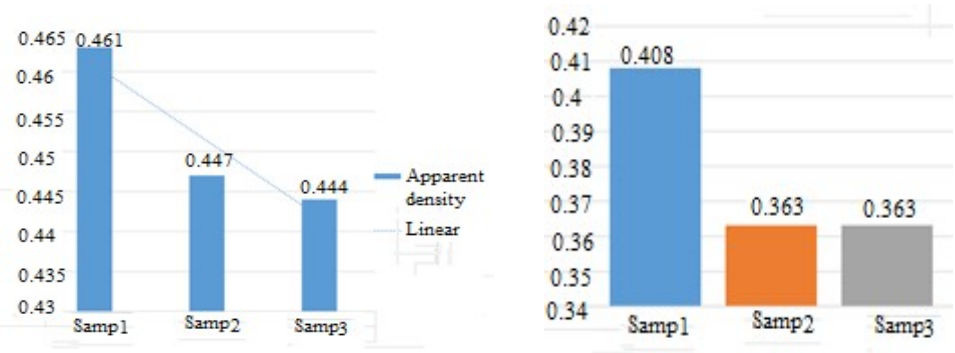

(a) **(b)**

Figure 9. Variation in apparent density of fibers. **(a)** Stems; **(b)** Roots.

Table 3. Apparent mass of stem and root fibers.

	Sample 1		**Sample 2**		**Sample 3**	
	stem	**root**	**stem**	**root**	**stem**	**root**
m_0 (g)	1.012	1.005	1.003	1.01	1.002	1.01
m_1 (g)	373.249	366.628	376.882	364.49	375.279	367.43
m_2 (g)	373.504	367.01	377.076	364.718	375.466	367.669

Table 3. (*Continued*).

	Sample 1		Sample 2		Sample 3	
	stem	**root**	**stem**	**root**	**stem**	**root**
m_3 (g)	2.44	2.4841	2.433	3.01	2.442	3.018
ρ_{app}	0.461	0.408	0.447	0.363	0.444	0.363

3.5. Water content

Table 4 presents the water content values obtained from stem and root fibers using Equation (4). These results allowed us to draw **Figure 10**.

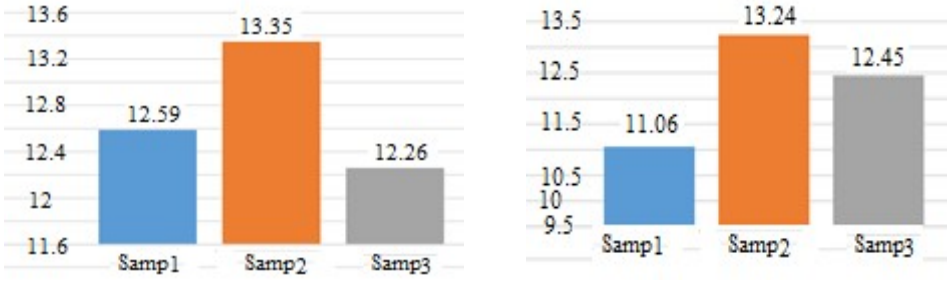

(a) **(b)**

Figure 10. Variation in moisture content of fibers. **(a)** stems; **(b)** roots.

Table 4. Moisture content of stem and root fibers.

	Sample 1		Sample 2		Sample 3	
	stem	**root**	**stem**	**root**	**stem**	**root**
m_h(g)	1.008	1.004	1.011	1.009	1.003	1.002
m_s(g)	0.881	0.904	0.876	0.891	0.88	0.891
W(%)	12.59	11.06	13.35	13.24	12.26	12.45

We have on average a humidity rate of 12.73% for stem fibers and 12.25% for root fibers. Stem fibers have a higher water content than root fibers, which implies the rigidity of our stem fibers because they are responsible for maintaining and transporting water to the leaves. Compared to other plants, these fibers have a higher humidity level than that of flax fibers (10%); Hemp (10.8%); of bagasse (8.8%) [30] and lower than that of Abaca fibers (15%); Sida rhombifolia fibers extracted with boiling water (13.28%) [11]. This variation can be attributed to the different harvest sites.

3.6. Water absorption rate

Table 4 is also used to calculate, via Equation (5), the water content obtained from stem and root fibers. These results allowed us to draw **Figure 11**. We have on average an absorption rate of around 142.46%, with a porosity of 65.91% for stem fibers and of around 193.16% with a porosity of 71.92% for root fibers. Root fibers have a higher absorption rate and porosity than stem fibers, which means that root fibers have more empty spaces in their pores. This factor can therefore influence the durability and longevity of this fiber, most often leading to cracks and a reduction in stiffness in final products such as composite materials [31]. Compared to other

plants, stem fibers have a higher absorption rate than Triumfeta Pentandra fibers (183.31%) [32]; Pineapple Comosus (188.64%) [15], and lower than that of SR fibers extracted by hot water retting [29] (225.12 ± 15.67%) [11]; Neuropeltis Acuminata (276.16%) [16].

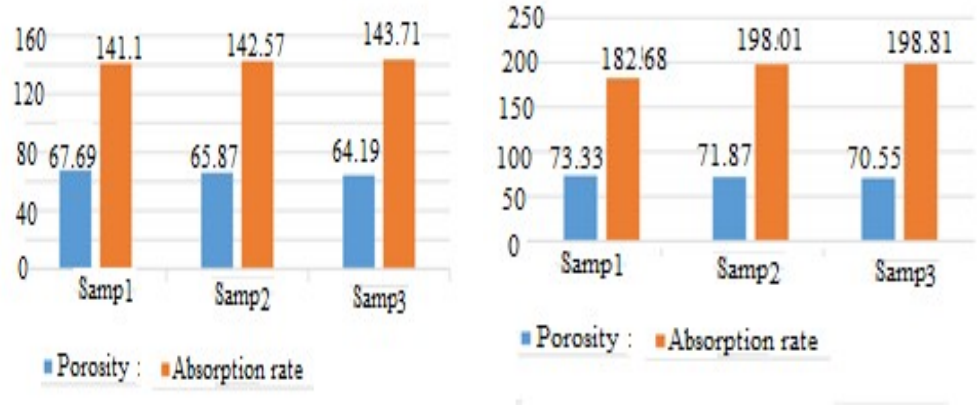

(a) **(b)**

Figure 11. Variation in fiber absorption rate. **(a)** Stems; **(b)** Roots.

3.7. Diameter under the microscope

3.7.1 Diameter and frequency distribution

Table 5 and **Table 6** present the different values of the diameter obtained from the stem and root fibers, allowing to draw the curves in **Figure 12**. We have on average a diameter of 7.20 mm for stem fibers and 4.69 mm for root fibers. **Tables 7** and **8** present the different values of the appearance frequencies depending on the diameter, which allowed us to draw the curves in **Figure 13**. Thus, we obtain a diameter of 3.81 mm for the root fibers and 6.69 mm for the stem fibers.

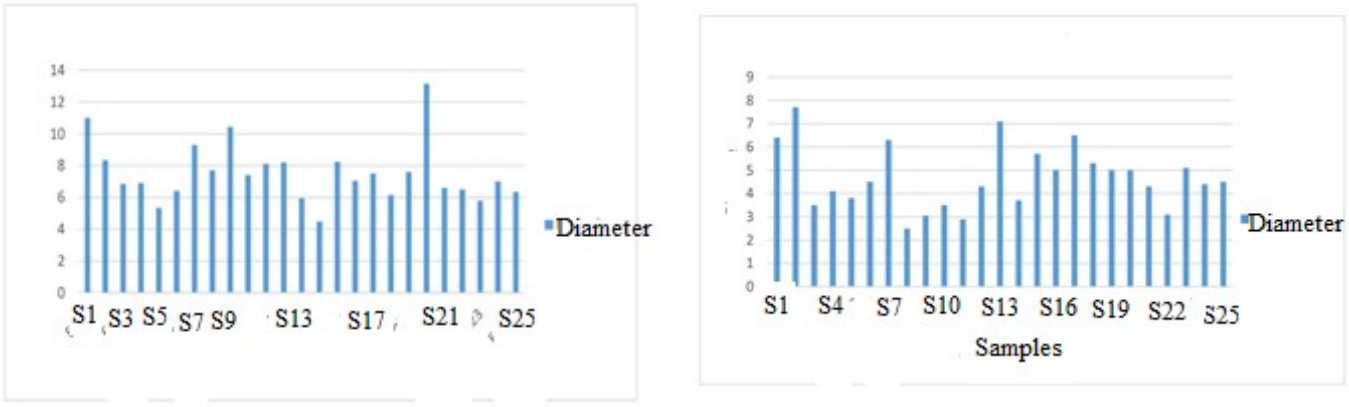

(a) **(b)**

Figure 12. Variation in fiber diameter. **(a)** Stems; **(b)** roots depending on the samples.

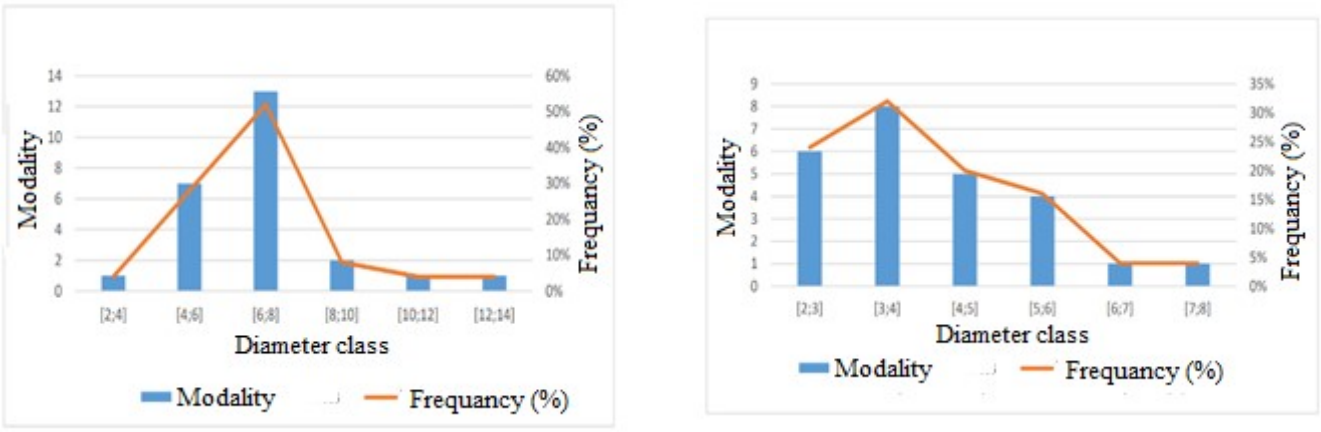

(a) **(b)**

Figure 13. Variation in the frequencies of fibers. **(a)** Stems and; **(b)** Roots as a function of diameter.

Table 5. Diameter of stem fibers under the microscope.

Samples	ϕ_1	ϕ_2	ϕ_{moy}	ϕ_{moy}(mm)	**Section** (mm^2)
S1	11	11	11	0.44	0.151976
S2	8.2	8.5	8.35	0.334	0.08757176
S3	7.1	6.6	6.85	0.274	0.05893466
S4	6.8	7.0	6.9	0.276	0.05979816
S5	5.3	5.4	5.35	0.214	0.03594986
S6	6.4	6.4	6.4	0.256	0.05144576
S7	9.8	8.8	9.3	0.372	0.10863144
S8	7.4	8.0	7.7	0.308	0.07446824
S9	10.5	10.4	10.45	0.418	0.13715834
S10	8.2	6.6	7.4	0.296	0.06877856
S11	7.6	8.6	8.1	0.324	0.08240616
S12	8.4	8.0	8.2	0.328	0.08445344
S13	5.8	6.1	5.95	0.238	0.04446554
S14	4.5	4.5	4.5	0.18	0.025434
S15	8.4	8.1	8.25	0.33	0.0854865
S16	7.1	7	7.05	0.282	0.06242634
S17	7.5	7.5	7.5	0.3	0.07065
S18	5.9	6.4	6.15	0.246	0.04750506
S19	7.8	7.4	7.6	0.304	0.07254656
S20	12	14.6	13.15	0.526	0.21719066
S21	7.2	6.0	6.6	0.264	0.05471136
S22	5.8	7.2	6.5	0.26	0.053066
S23	6.4	5.2	5.8	0.232	0.04225184
S24	7.2	6.8	7	0.28	0.061544
S25	7.0	5.7	6.35	0.254	0.05064506

Table 6. Root fiber diameter under the microscope.

Samples	ϕ_1	ϕ_2	ϕ_{moy}	$\phi_{moy}(mm)$	Section (mm^2)
S1	7.4	5.4	6.4	0.256	0.05144576
S2	7.6	7.8	7.7	0.308	0.07446824
S3	3.2	3.8	3.5	0.14	0.015386
S4	4.0	4.2	4.1	0.164	0.02111336
S5	4.6	3.0	3.8	0.152	0.01813664
S6	6.0	3.0	4.5	0.18	0.025434
S7	6.8	5.8	5.3	0.252	0.04985064
S8	2.2	2.8	2.5	0.1	0.00785
S9	1.6	4.5	3.05	0.122	0.01168394
S10	2.2	4.8	3.5	0.14	0.015386
S11	2.8	3.0	2.9	0.116	0.01056296
S12	5.2	3.4	4.3	0.172	0.02322344
S13	7.0	7.2	7.1	0.284	0.06331496
S14	4.2	3.2	3.7	0.148	0.01719464
S15	4.6	6.8	5.7	0.228	0.04080744
S16	4.8	5.2	5.0	0.2	0.0314
S17	6.2	6.8	6.5	0.26	0.053066
S18	6.0	4.6	5.3	0.212	0.3528104
S19	5.2	4.8	5.0	0.2	0.0314
S20	4.6	5.4	5.0	0.2	0.0314
S21	4.6	4.0	4.3	0.172	0.02322344
S22	3.4	2.8	3.1	0.124	0.01207016
S23	5.6	4.6	5.1	0.204	0.03266856
S24	3.8	5.0	4.4	0.176	0.02431616
S25	4.6	4.4	4.5	0.18	0.025434

3.7.2. Probability distribution

The graphs of **Figure 14** present the probabilities of the appearance of fibers from PP stems and roots as a function of diameter by the method of statistical analysis using the maximum entropy principle. The peaks observed on these graphs designate the probable value of the diameter of our fibers. Thus, we obtain a value of 4 mm for the root fibers and 7 mm for the stem fibers.

In short, it is clear that the value of the fiber diameter obtained through these different diagrams and methods is approximately the same. Thus, we can conclude that this is due to the reliability and consistency of the results obtained, as well as to the quality of the fiber processing.

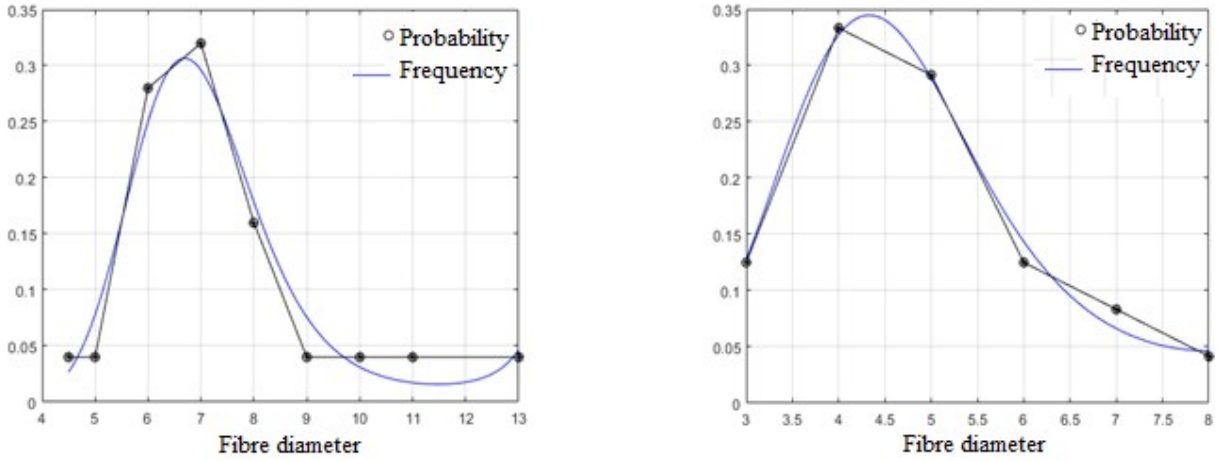

(a) **(b)**

Figure 14. Probabilities of appearance of fibers. **(a)** stems; **(b)** roots as a function of diameter.

Table 7. Frequencies of appearance of stem fibers.

Class of different diameters	Modes of appearance	Frequency (%)
[2;3]	6	24%
[3;4]	8	32%
[4;5]	5	20%
[5;6]	4	16%
[6;7]	1	4%
[7;8]	1	4%

Table 8. Frequencies of appearance of root fibers.

Class of different diameters	**Modes of appearance**	**Frequency (%)**
[2;4]	1	4%
[4;6]	7	28%
[6;8]	13	52%
[8;10]	2	8%
[10;12]	1	4%
[12;14]	1	4%

3.8. Mechanical properties

3.8.1. Tensile strength

Stress strain curves

Figure 15 shows the tensile results of the PP stem, while **Figure 16** shows that of the PP root fibers according to results shown in **Table 9**. The fibers of the stems have an average elasticity modulus higher than that of the fibers of the roots (1559 MPa or 1.556 GPa) or a value of 3982.506 MPa or 3.982 GPa. Compared to other plants, stem fibers have a higher elasticity modulus than that of spine fibers (2.31 GPa), date palm fibers (2.5 GPa) [33]. Furthermore, the root fibers have a higher tensile strength than the stem fibers (1186.59 MPa), that is an average value of

1960.35 MPa. Compared to other plants, this fiber has a higher tensile strength than hemp fibers (70 MPa); ramie fibers (400-938 MPa); kenaf fibers (930 MPa) [34].

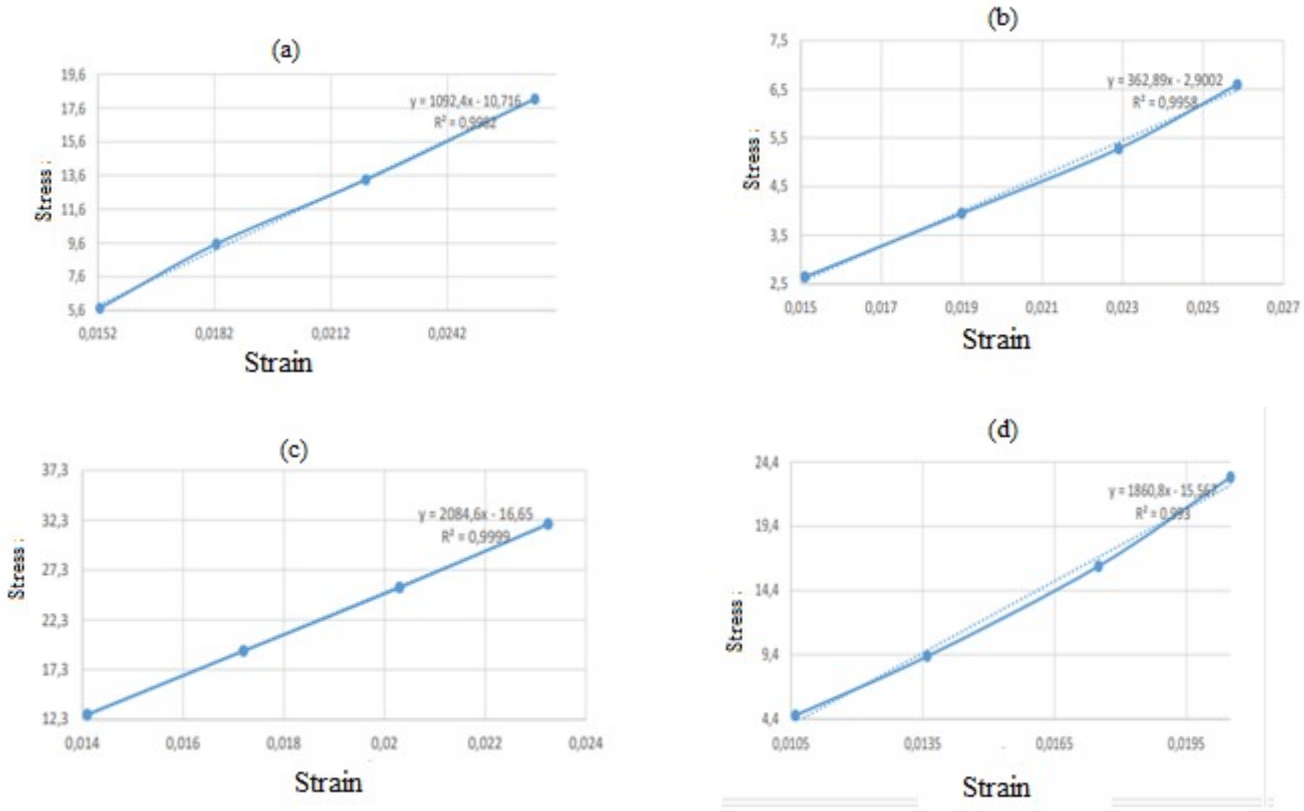

Figure 15. Curves of stress as a function of strain of the stem fibers. **(a)** Sample 1; **(b)** Sample 2; **(c)** Sample 3; **(d)** Sample 4.

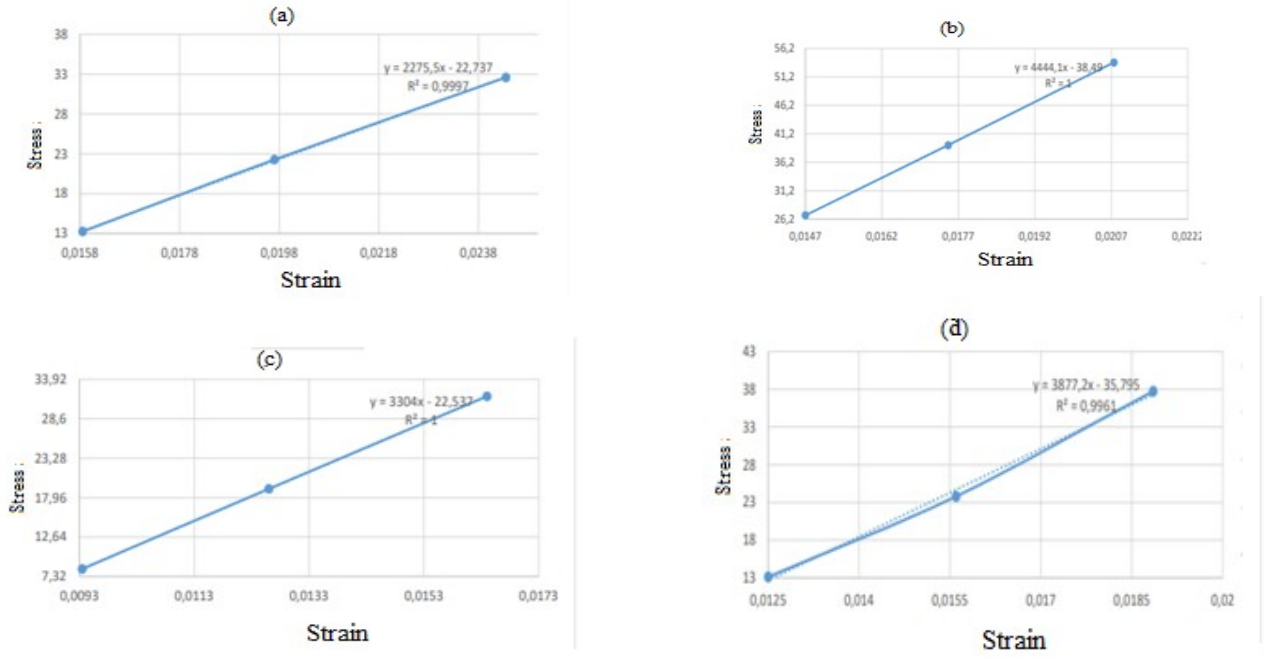

Figure 16. Curves of stress as a function of deformation of the root fibers. **(a)** Sample 1; **(b)** Sample 2; **(c)** Sample 3; **(d)** Sample 4.

Table 9. Mechanical properties of stem and root fibers.

Samples	Elongation (mm)		Stress (MPa)		E (MPa)	
	Stem	Root	Stem	Root	Stem	Root
S1	0.4355	1.1383	490.781	545.3874	2275.5	1092.4
S2	0.96435	1.76475	2212.9459	217.3954	4444.1	362.89
S3	0.2064	1.2692	181.4381	889.6399	3304	2084.6
S4	1.1384	6.335	2462.54	4104.817	3877.2	1860.8
S5	0.4015	4.6257	1005.3991	3340.078	7452.2	1720.8
S6	0.6398	5.7101	2132.2245	2215.853	7149.6	1416.3
S7	0.20255	3.2855	33.9491	2182.022	6447.9	1517.5
S8	0.7569	3.8625	1589.6046	2980.127	3031.5	2020.9
S9	0.37285	1.5984	449.4077	1280.64	1922.6	1111.8
S10	0.4281	8.27145	530.542	4624.984	285.2	2005.6
S11	0.5677	0.8346	1099.092	664.299	3532.2	1525.6
S12	0.7553	1.296	1400.4883	1651.854	3798.8	2412.7
S13	0.8566	3.3486	2182.5235	1705.646	6926.1	1200
S14	0.2295	4.07215	428.0883	1788.427	6417.6	1693
S15	1.0565	1.5333	1612.7337	766.9272	3104.9	1084.2
S16	0.6598	3.7796	985.8985	5444.299	2910.5	3470
S17	0.8153	2.6014	117.7384	1551.822	1862	1306.3
S18	1.2495	2.2255	1975.0753	1430.602	2961.7	1210
S19	0.39955	2.6358	221.2801	1352.834	955.29	1399.9
S20	0.74665	2.6615	1415.1948	1276.497	1925.4	472.41
S21	0.2805	1.7229	313.3079	1453.344	3525.5	2087.9
S22	0.8881	1.0687	4102.5471	1239.934	8761.7	1086.9
S23	1.35235	1.3147	167.9833	947.4119	1024	1971.9
S24	0.17665	6.98055	399.92	4227.628	7526.3	1433
S25	0.92685	1.7909	800.2079	1126.327	2074.06	1448.7

Elongation at break

On average, we obtained an elongation of around 16.17% for the stem fibers, which indicates a lower capacity to deform before breaking. Compared to other plants, stem fibers have a higher elongation than sugar cane bagasse fibers (5.5%), and pineapple fibers (14.5%) [35]. On the other hand, the fibers of the roots have an elongation of an average value of 60.6%; this value is higher than that of the fibers of the stems, which means that they are more ductile and can deform more before breaking up. This can be advantageous in certain applications such as textiles. Compared to other plants, root fibers have a higher elongation than coconut fibers (15–40%), date palm fibers (2–19%).

4. Conclusion

In this work, we examined the extraction and physico-mechanical characterization of fibers from the stems and roots of the PP plant with the aim of

evaluating the possibility of using them as stabilizers in compressed earth bricks. This plant with ecological, economic and social virtues opens the way to new and very interesting applications. Based on the literature and the work carried out on this plant, our plant was harvested in West Cameroon, more precisely in Batié in the high plateau division. We first presented the different materials and methods used during the works, so we extracted the fibers using the boiling water method. This extraction method was used because of the advantages it provides, such as the relatively short time required for the extraction; there is no risk of pollution or infection and the process is hygienic. Once the fibers were extracted, they were treated with a 10% sodium hydroxide (NaOH) solution. Then the physico-mechanical characterization of the fibers was subsequently carried out from the stems and roots of the PP through, among which the determination of the absolute density according to the NF EN 1097-6 standard, the linear mass according to the ISO 1973 standard 2021 editions, the apparent density according to the NF EN 1097-3 standard, August 1998 edition, the water content according to the ISO 3344: 1997 standard, the water absorption rate according to the NF EN 1097-6 standard, the diameter under the microscope according to the ISO 137 standard and finally the determination of their mechanical properties (Young's modulus, tensile strength, etc.).

As results, the fibers of the stems have an absolute density of 1.35 g/cm^3, a linear mass of 54.6 tex, an apparent density of 0.451 g/cm^3, a content of water of 12.73%, an absorption rate of 142.46%, to determine the diameter of these fibers we proceeded by three steps. We first took the average of all our samples and obtained a value of 7.20 mm, secondly, we determined the frequency of appearance for each sample based on the diameter of our fibers and obtained a diameter of 6.69 mm, and thirdly we proceeded by the method of statistical analysis using the principle of maximum entropy thus obtaining a value of 7 mm. Finally, we obtained an elastic modulus of 3.98 GPa, a tensile strength of a value of 1186.59 MPa and an elongation of 16.17%.

While for the root fibers we obtained an absolute density of 1.34 g/cm^3, a linear mass of 16.76 tex, an apparent density of 0.378 g/cm^3, a water content of 12.25%, a absorption rate of 193.16%, a diameter of 4.69 mm by the average, 3.91 mm by the probability of appearing of each sample, and 4 mm, using the statistical analysis method via the maximum entropy principle. At the end we obtained an elastic modulus with a value of 1.55 GPa, a tensile strength with a value of 1960.35 MPa, and an elongation of 60.6%. From this study we can conclude that the fibers from stems are more suitable for industrial applications, since they have the greatest elastic modulus, and thus they are more resistant and thus suitable for compressed earth brick manufaturing. However, root fibers are lighter and are therefore more important for applications not requiring significant mass change, such as in the textile industries.

These fibers can also be used for several purposes, including the manufacture of absorbent materials such as sanitary paper and napkins, the manufacture of composite materials.

For future works, it would be interesting to:

- Determine the chemical and thermal properties of PP fibers, to have more information on this fiber.
- Incorporate the stem fibers with well-determined proportions into the CEBs with the aim of determining their behavior as a reinforcing material.

Author contributions: Conceptualization, FK, SKDN and EYB; methodology, FK, RE, ADA, BNB, GT and MNN; software, OLT and SKDN; validation, GT and EYB; formal analysis, FK, RE and SKDN; investigation, RE, ADA, OLT and SKDN; data curation, FK, BNB, GT and SKDN; writing—original draft preparation, FK, RE and SKDN; writing—review and editing, FK; visualization, FK; supervision, GT and EYB. All authors have read and agreed to the published version of the manuscript.

Conflict of interest: The authors declare no conflict of interest.

References

1. Chen L, Hu L, Wang, R, et al. Green building practices to integrate renewable energy in the construction sector: A review. Environmental Chemistry Letters. 2024; 22: 751–784.
2. Sanjay MR, Madhu P, Jawaid M, et al. Characterization and properties of natural fiber polymer composites: A comprehensive review. Journal of Cleaner Production. 2018; 172: 566–581.
3. Elfaleh I, Abbassi F, Habibi M. et al. A comprehensive review of natural fibers and their composites: An eco-friendly alternative to conventional materials, Results in Engineering. 2023; 19: 101271.
4. Sandhu JS, Kumar D., Yadav VK, et al. A Recent trends in breeding of tropical grass and forage species. In: Proceedings of the 23rd International Grassland Congress 2015-Keynote Lectures; 20–24 November 2015; New Delhi, India. pp. 337–348.
5. Donadio S, Giussani LM, Kellogg EA, et al. A preliminary molecular phylogeny of Pennisetum and Cenchrus (Poaceae-Paniceae) based on the trnL-F, rpl16 chloroplast markers. Taxon. 2009; 58(2): 392–404.
6. Magcale-Macandog D, Prédo C, Menz K, Predo A. Napier grass strips and livestock: a bioeconomic analysis. Agroforestry Systems. 2013; 40(1): 41–58.
7. Van den Berg J, Van Hamburg H. Trap cropping with Napier grass, Pennisetum purpureum (Schumach), decreases damage by maize stem borers. International Journal of Pest Management. 2015; 61(1): 73–79.
8. Orodho, AB. The Role and Importance of Napier Grass in the Smallholder Dairy Industry in Kenya. Available online: http://www.fao.org/ag/AGP/AGPC/doc/Newpub/napier/napier_kenya.htm%0Ahttp://www.fao.org/ag/agp/agpc/doc/newpub/napier/napier_kenya.htm (accessed on 2 April 2024).
9. Khan ZR, Midega CAO, Wadhams, LJ, et al. Evaluation of Napier grass (Pennisetum purpureum) varieties for use as trap plants for the management of African stemborer (Busseola fusca) in a push-pull strategy. Entomologia Experimentalis et Applicata. 2007; 124: 201–211.
10. Khan, ZR, Midega CAO, Hutter NJ, et al. Assessment of the potential of Napier grass (Pennisetum purpureum) varieties as trap plants for management of Chilo partellus. Entomologia Experimentalis et Applicata. 2006; 119(1):15–22.
11. Ngoup T, Efeze ND, Kanaa T, Mbang JPE. et al. Physical, Chemical and Mechanical Characterization of Sida Rhombifolia Fibers from the Center Region of Cameroon for their potential use in textiles and composites. Journal of Natural Fibers. 2024; 21(1): 2294478.
12. Libog L, Biyeme F, Betené ADO, Biwolé B, et al. Influence of the Extraction Location on the Physical and Mechanical Properties of the Pseudo-Trunk Banana Fibers. Journal of Natural Fibers. 2023; 20(2).
13. Anafack S M, Harzallah O, Nkemaja D. et al. Effects of extraction techniques on textile properties of William banana peduncle fibers. Industrial Crops and Products. 2023; 201: 116912.
14. Joseph S, Sreekala MS, Oommen Z. et al. A comparison of the mechanical properties of phenol formaldehyde composites reinforced with banana fibers and glass fibers. Composites Science and Technology. 2016; 62(14): 1857–1868.
15. Asim MK, Abdan M, Jawaid M. et al. A Review on Pineapple Leaves Fiber and Its Composites, International Journal of Polymer Science. 2015; 1–16.

16. Betene ADO, Betene FE, Martoïa F, et al. Physico-Chemical and Thermal Characterization of Some Lignocellulosic Fibers: Ananas comosus (AC), Neuropeltis acuminatas (NA) and Rhecktophyllum camerunense (RC), Journal of Minerals and Materials Characterization and Engineering. 2020; 8: 205–222.
17. Jawaid M, Khalilb HPSA, Hassana A. et al. Effect of jute fiber loading on tensile and dynamic mechanical properties of oil palm epoxy composites. Compos. Part B Eng. 2013; 45: 619–624.
18. Mwaikambo LA, Ansell MP. Mechanical properties of alkali-treated plant fibers and their potential as reinforcing materials. I. Hemp fibers. Journal of Materials Science. 2006; 41(8): 2483–2496.
19. Preethi P, Balakrishna G. Physical and Chemical Properties of Banana Fiber Extracted from Commercial Banana Cultivars Grown in Tamilnadu State. Agrotechnology. 2013; 1(11): 10–12.
20. Syrille B, Nicodème R, Omar H, et al. Effect of alkali and silane treatments on the surface energy and mechanical performances of Raphia vinifera fibers. Industrial Crops and Products. 2022; 190
21. Monteiro SN, Perissé F, Lopes D et al. Natural Lignocellulosic Fibers as Engineering Materials-An Overview. Metallurgical and Materials Transactions A. 2016; 42A: 2963-29297.
22. John MJ, Anandjiwala RD. Recent developments in chemical modification and characterization of natural fiber-reinforced composites. Polymer Composites. 2008; 29(2): 187–207.
23. Ridzuan MJM, Majid MSA, Afendi M, Khasri A. The Effects of the Alkaline Treatment's Soaking Exposure on the Tensile Strength of Napier Fiber. Procedia Manufacturing. 2015; 2: 353–358.
24. Alemayeh TN, Abel T, Alok K, et al. Opportunities for Napier Grass (Pennisetum purpureum) Improvement Using Molecular Genetics. Agronomy. 2017; 7: 28.
25. Ali RA, Mahamat KN, Marinette JG. et al. Mathematical Prediction of Electrical Solar Energy Based on Solar Data for Two Main Cities of Chad: Mongo in the Centre and Pala in the South of Chad, Journal of Energy, Environmental & Chemical Engineering. 2024; 9(1): 33–45.
26. Kenmogne F. Statistical estimation of mean wind energy available in western Region, of Cameroon: case of the Bafoussam's city. Journal of Harmonized Research in Engineering. 2017; 5(1): 15–27.
27. Nur AF, Mat Nasir J, Zainudin Z. The Effect of Alkaline Treatment onto Physical, Thermal,Mechanical and Chemical Properties of Lemba Leaves Fibersas New Resources of Biomass. Pertanika Journal of Science and Technology. 2020; 28(24): 1531–1547.
28. Bledzki AK, Gassan J. Composites reinforced with cellulose based fibers, Composites reinforced with cellulose based fibers, Progress in Polymer Science. 1999; 24(2): 221–274.
29. Camille M. Contribution to the Formulation and Characterization of an eco-Building Material Based on Agro Resources, Toulouse III [PhD thesis]. University-Paul Sabatier; 2010.
30. Bledzki AK, Segovia C, Sperber VE, Faruk O. Natural and Wood Fiber Reinforcement in Polymers. Smithers Rapra Publishing; 2002.
31. Mewoli AE, Segovia CFB, Ebanda FB. et al. 2020. Physical-Chemical and Mechanical Characterization of the Bast Fibers of Triumfetta cordifolia A. Rich. from the Equatorial Region of Cameroon. Journal of Minerals and Materials Characterization and Engineering. 2020; 8(4).
32. Nkapleweh, AD, Tendo JF, Ebanda FB. et al. Physico-Chemical and Mechanical Characterization of Triumfetta Pentandra Bast Fiber from the Equatorial Region of Cameroon as a Potential Reinforcement of Polymer Composites. Journal of natural fibers. 2022; 19(16): 13106–13119.
33. Sathishkumar T, Navaneethakrishnan P, Shankar S. et al. Characterization of natural fiber and composites—A review. Journal of Reinforced Plastics and Composites. 2013; 32(19): 1457-1476.
34. John MJ, Thomas S. Royal Society of Chemistry Cambridge. United Kingdom. Natural Polymers. 2012; 2: 21.
35. Teboho M, Mtibe A, Mokhothu TH, Sadiku F. Recent progress on natural fiber hybrid composites for advanced applications: A review. eXPRESS Polymer Letters. 2018; 13(2): 159–198.

Materials Technology Reports 2024, 2(1), 1721.
https://doi.org/10.59400/mtr.v2i1.1721

Article

Evaluating eggshells as sustainable weighting agents in water-based drilling muds: A novel approach for enhanced efficiency and environmental consciousness

Anas Elhederi*, Mansoor Zoveidavianpoor

Department of Petroleum Engineering, University of Technology Malaysia, 81310, Malaysia
*** Corresponding author:** Anas Elhederi, anaselhoderi@gmail.com

CITATION

Elhederi A, Zoveidavianpoor M. Evaluating eggshells as sustainable weighting agents in water-based drilling muds: A novel approach for enhanced efficiency and environmental consciousness. Materials Technology Reports. 2024; 2(1): 1721. https://doi.org/10.59400/mtr.v2i1.1721

ARTICLE INFO

Received: 12 April 2024
Accepted: 12 June 2024
Available online: 25 June 2024

Abstract: This study investigates the utilization of eggshells, a renewable material, as a weighting additive in water-based drilling muds with different exploring concentrations. The primary objectives were to assess the impact of eggshells on the rheological properties of drilling muds and to determine the optimal concentration of eggshells for achieving desired density and stability, drawing comparisons with calcium carbonate ($CaCO_3$). Both eggshell powder (ESP) and $CaCO_3$ effectively increase mud weight to the target density of 8.75 ppg at 30 g. Notably, ESP exhibits favorable rheological properties at 20 g, maintaining low plastic viscosity 2.7, consistent yield points 1.1, and gel strength comparable to $CaCO_3$. Conversely, $CaCO_3$ shows signs of potential deterioration at 30 g indicated by increased viscosity to 3.5 and decreased yield point to 0.5. ESP demonstrates superior filtration performance, displaying a progressive increase in cake thickness with increasing weight 1.32 mm to 3.12 mm compared to the slower cake build-up of $CaCO_3$ 0.92 mm to 2.9 mm. Both additives slightly elevate mud pH, potentially enhancing overall stability.

Keywords: eggshell powder; calcium carbonate; drilling fluids; water-based mud; environmental sustainability; biodegradable materials

1. Introduction

It is essential to monitor the rheological parameters of the drilling fluid in the well. The data allows for precise estimation of frictional loss. Drilling fluid undergoes considerablechanges in its properties as it moves through the well and is subjected to varying conditions (such as temperature, pressure, time, etc.). This makes monitoring and controlling its rheological qualities more challenging [1]. Precisely determining the rheology to the last detail calls for a comprehensive knowledge of the drilling fluid, including the effect of relevant microstructure mechanisms on flow parameters [2].

Fluid loss must be effectively controlled in order for drilling operations to be efficient and safe, as uncontrolled fluid loss can cause formation damage when mud filtrate invades the exposed rock [3]. This infiltration not only affects productivity, but it also raises operating expenses owing to corrective efforts. Fluid loss has long been a major issue in the oil and gas sector, hurting production rates and operating efficiency. Despite developments, fluid loss management is crucial to improving drilling performance and maintaining well integrity [4].

Weighting additives are important for drilling fluids used in the oil and gas industry, especially water-based mud (WBM). These additives make the drilling fluid denser so that the pressure in the wellbore stays steady. Weighting additives keep formation fluids from getting into the well and prevents blowouts. Most of the time,

barite and $CaCO_3$ are used as bearing additives [5]. However, as people become more aware of environmental issues [6], they seek other better environmental additives [7]. Drilling fluid is acomplex mixture that relies heavily on additives. Additives can be added to the drilling fluid depending on the intended performance and the challenges encountered. The drilling operation should go smoothly, and the additives should aid with that [8].

Eggshells are primarily composed of calcium carbonate ($CaCO_3$), which constitutes about 94%–97% of their dry weight. Calcium carbonate is a naturally occurring compound also found in minerals such as limestone, marble, and chalk. In addition to $CaCO_3$, eggshells contain small amounts of other minerals like magnesium carbonate (0.3%–0.6%) and calcium phosphate (0.5%–1.0%), as well as organic matter, including proteins and other organic compounds, which make up 2%–4% of the total composition [9]. The analysis of eggshell powder (ESP) further confirms that its primary component is the thermodynamically stable calcite phase of $CaCO_3$. This calcite structure contributes to the significant hardness of the eggshell, and the characteristic peaks observed align well with $CaCO_3$, confirming its rhombohedral structure. The findings indicate that $CaCO_3$ concentrations in eggshells exceed 90%, consistent with previous studies [10]. These properties make eggshells a viable alternative as a sustainable weighting agent in drilling muds, providing both environmental and functional benefits through their high $CaCO_3$ content and structural stability.

A hyperbolic fluid loss model for HPHT conditions was developed to improve fluid loss predictions, which is relevant for controlling fluid loss in eggshell-based muds [11]. Studies on salt contamination and temperature effects [12] and filter cake formation [13] offer insights into the performance of eco-friendly additives like eggshells. Further research highlighted the impact of contaminants on mud properties, emphasizing the need for stable additives [14]. A kinetic model for filter cake formation in HPHT environments would also be useful for assessing eggshell-based muds [15].

The objective of this study is to investigate the potential use of eggshells and naturally occurring weighting additives in water-based drilling muds, evaluate their effects on the rheological properties compared to traditional weighting agents such as $CaCO_3$, and determine the optimal concentration of eggshells required to achieve the desired density and stability, while benchmarking these results against those obtained with $CaCO_3$.

The paper is organized as follows: Section 2 describes how eggshells and $CaCO_3$ were used to examine essential rheological parameters such as viscosity, gel strength, filtration, and pH, following API guidelines; In Section 3, eggshells and $CaCO_3$ are compared for their ability to increase mud weight, stabilize plastic viscosity, maintain yield point, optimize mud cake thickness, and pH levels; Section 4 highlights the important findings, stressing eggshells' better performance in terms of stable rheological characteristics and increased filtering efficiency and defines the ideal concentration for field applications.

2. Experimental

Following API standards for water-based drilling mud API RP 13B-1, eggshells and $CaCO_3$ are separately incorporated into the base mud at concentrations of 10 g, 20 g, and 30 g based on the literature [16]. Each material is blended for 10 mins to ensure homogeneity. The research systematically investigates the influence of these additives on the rheological properties of the drilling mud such as the viscosity test measures how easily mud flows at different shear rates, which helps determine the mud's resistance to flow. Gelstrength tests measure a mud's ability to prevent cuttings from settling when circulation stops.API filtrate test measures the amount of fluid that escapes from the drilling mud under pressure within a specific time frame. pH test determines the acidity or alkalinity of mudusing a pH meter or pH indicator to measure the concentration of hydrogen ions. All experimental procedures for mud testing were conducted in accordance with established methodologies outlined in the literature [16]. **Table 1** shows the formulation of base mud used in this study.

Table 1. Formulation of base mud.

Additive	Description/Function	Quantity	Mixing Time
Deionized water	Base liquid	350 mL	-
Bentonite	Clay for viscosity/APIfiltrate control	14 g	10 min
Eggshells powder (ESP)	Weighting material	10 g, 20 g and 30 g	10 min
Calcium Carbonate ($CaCO_3$)	Weighting material	10 g, 20 g and 30 g	10 min

3. Results

This section presents the results of the experimental evaluation of ESP and $CaCO_3$ as weighting agents in water-based drilling muds. The results are discussed in terms of key parameters such as density, plastic viscosity, yield point, gel strength, mud cake thickness, and pH.

3.1. Density measurement

Both ESP and $CaCO_3$ successfully increased the mud weight, achieving the target density of 8.75 ppg at 30 g (**Figure 1**). At lower concentrations (10 g and 20 g), the densities for both additives were comparable, with a slight increase at 20 g,where ESP and $CaCO_3$ both reached 8.72 ppg. These results suggest that both additives are equally effective in increasing the mud density. However, considering all factors, 20 g of ESP appears to be the optimal concentration, providing a balance between effective density and desirable rheological properties.

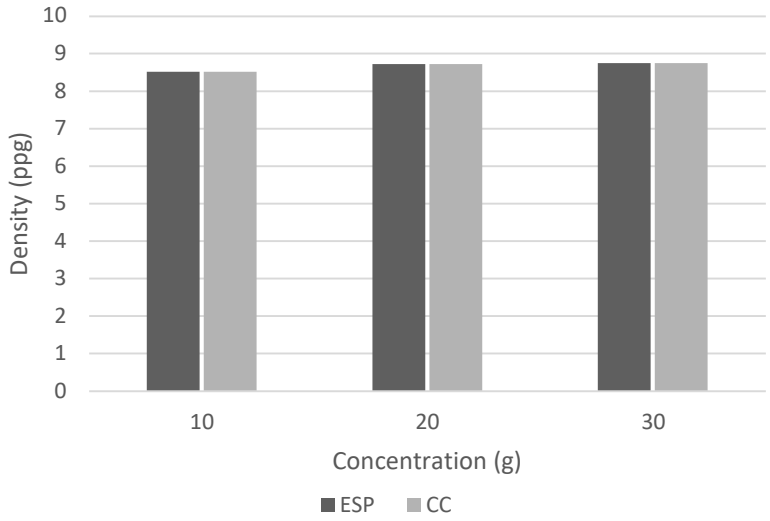

Figure 1. Results of density for both ESP and $CaCO_3$.

3.2. Plastic viscosity (PV)

Plastic viscosity is a key indicator of the flow characteristics of drilling mud. By using Fann viscometer both ESP and $CaCO_3$ measured at room temperature showed a decrease in plastic viscosity at 20 g compared to 10 g, suggesting improved flowability at intermediate concentrations (**Figure 2**).

At 30 g, ESP remained stableat a PV of 3, while $CaCO_3$ increased to 3.5, indicating potential deteriorating flow behavior in$CaCO_3$-based mud. This suggests that ESP maintains more stable rheological properties at higher concentrations, making it more suitable for scenarios where high mud weights are required without compromising flow.

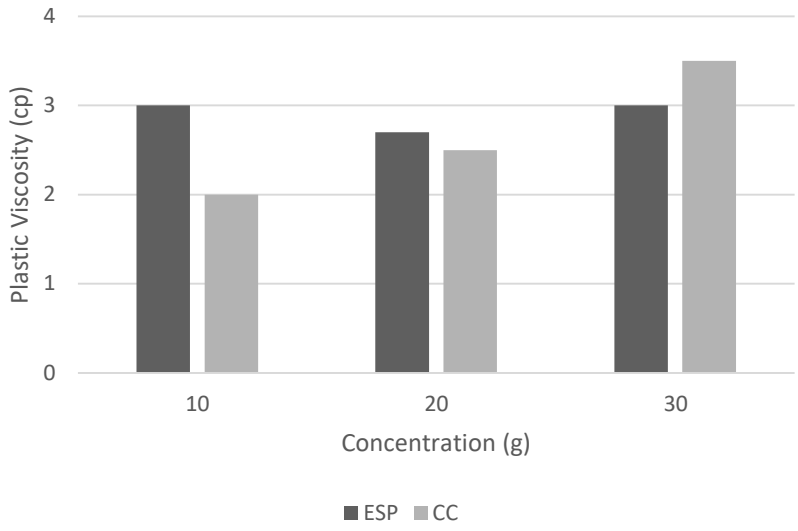

Figure 2. Plastic viscosity results for ESP and $CaCO_3$.

3.3. Point (YP)

Yield point reflects the ability of the mud to suspend solids under static conditions. By using Fann viscometer at room temperature. ESP exhibited consistent yield point values across all concentrations, maintaining a stable YP of 1 at 30 g (**Figure 3**). In contrast, $CaCO_3$ demonstrated a drop in YP at 30 g, falling from 1.5 at 20 g to 0.5 at 30 g, indicating potential challenges in maintaining wellbore stability and suspension capacity at higher concentrations. This highlights ESP's superior performance in maintaining wellbore stability.

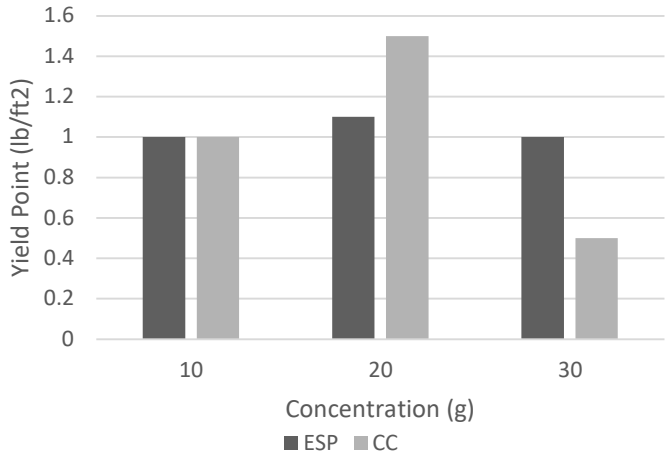

Figure 3. Yield point values for ESP and $CaCO_3$.

3.4. Gel strength (10 s and 10 min)

Gel strength measurements at 10 s and 10 min are critical for understanding the gelation behavior of drilling fluids. ESP demonstrated consistent gel strength at 2 for 10 s across all concentrations (**Figure 4**). $CaCO_3$, however, showed variability, with the 10-s gel strength increasing to 2 at 30 g. For 10-min gel strength, ESP maintained relatively stable values across concentrations, while $CaCO_3$ exhibited a more variable response, with a peak of 3 at 30 g (**Figure 5**). These results suggest that ESP provides more predictable and consistent gelation behavior, which is advantageous for maintaining wellbore stability during static conditions.

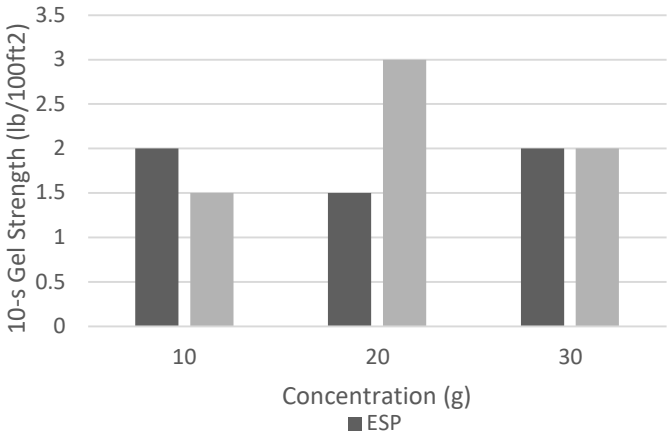

Figure 4. 10-s gel strength for ESP and $CaCO_3$.

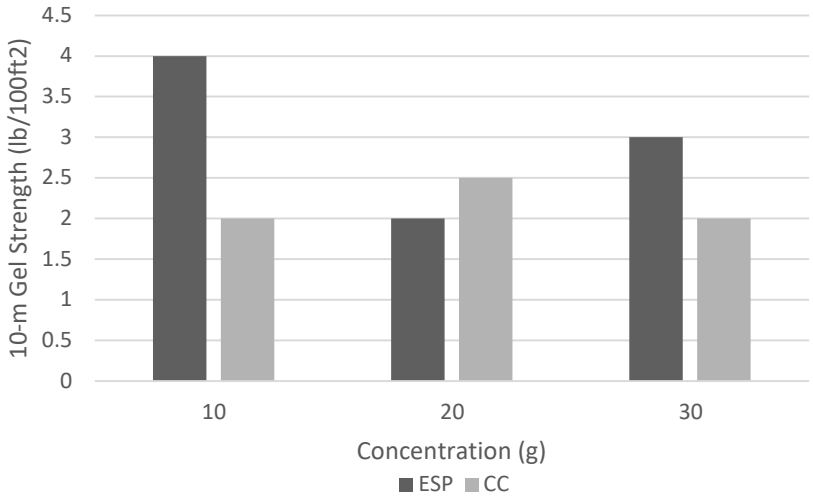

Figure 5. 10-min gel strength for ESP and $CaCO_3$.

3.5. Mud cake thickness

Mud cake thickness is an important factor in determining filtration efficiency. As shown in **Figure 6**, the mud cake thickness of ESP increased progressively with concentration, reaching 3.12 mm at 30 g. In comparison, $CaCO_3$ formed a thinner cake at 2.9 mm at 30 g. The rapid cake buildup of ESP suggests higher filtration efficiency, which could reduce fluid loss and enhance wellbore stability. The pronounced increase in ESP's mud cake thickness at higher concentrations highlights its superior filtration performance compared to $CaCO_3$.

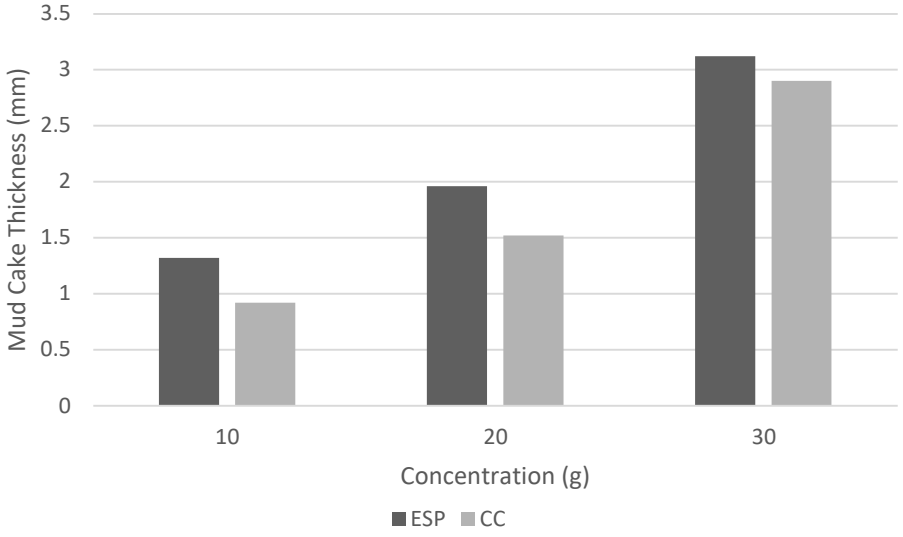

Figure 6. Mud cake thickness for ESP and $CaCO_3$.

3.6. PH

Both ESP and $CaCO_3$ slightly increased the pH of the drilling fluid, with pH rising from 9.0 to 9.6 for ESP and from 8.95 to 9.68 for $CaCO_3$ (**Figure 7**). The increase in pH contributes to enhanced drilling fluid stability by hindering the precipitation of certain compounds. At 20 g, ESP provides a moderate pH increase (9.2), which strikes a balance between effective mud cake thickness and chemical stability, making it an optimal choice for operations requiring balanced mud performance.

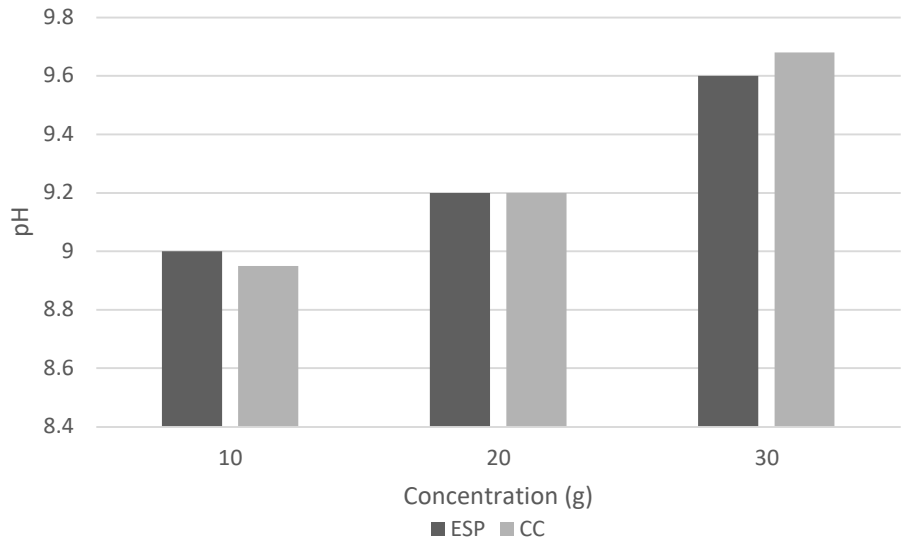

Figure 7. PH values for ESP and $CaCO_3$.

4. Discussion: Environmental impact and sustainability of eggshell powder in drilling fluids

The use of eggshell powder as a weighting agent in water-based drilling muds has a considerable environmental benefit due to its biodegradability and lower environmental effect when compared to synthetic additives commonly utilized in the oil and gas sector. As enterprises move toward more sustainable practices, the necessity for environmentally friendly materials in drilling operations has grown crucial. The oil and gas sector consumes plentiful resources like calcium carbonate, which requires large energy consumption and CO_2 emissions for extraction and processing. In contrast, ESP, a byproduct of the food industry, offers a renewable and low-carbon alternative that reduces waste and promotes the circular economy.

Research has demonstrated that integrating biodegradable compounds into drilling fluids can greatly minimize environmental concerns. Previous research [7] has proven the stability of synthetic-based mud using renewable resources, highlighting the potential of natural materials in sustainable drilling fluid systems. Similarly, another study [16] investigated the use of nano-sized tapioca starch as a natural polymer for filtration control in WBM, emphasizing the trend of replacing synthetic additives with biodegradable alternatives in drilling operations. Additional research [17] shown that adding eco-friendly additives such peanut shells in drilling fluids reduced fluid loss while simultaneously minimizing environmental impact during

disposal. Similarly, research [18] demonstrated the possibility for biodegradable drilling fluid additives to boost performance while lowering environmental impact. These findings lend credence to the concept that ESP, as a biodegradable substance, helps to reduce environmental impact, particularly in drilling fluid disposal.

Our analysis confirms that ESP and $CaCO_3$ have comparable rheological characteristics, density, and mud cake thickness. However, the important differential is ESP's biodegradability, which provides a significant benefit in reducing the environmental effect of drilling operations. Furthermore, the presence of hazardous additives and chemicals makes it difficult to dispose of old drilling fluids, particularly in environmentally sensitive locations. Using a biodegradable and renewable substance such as ESP reduces the possibility of soil and water pollution, which aligns with regulatory initiatives to prevent environmental deterioration. This is especially significant in offshore drilling, where rigorous environmental rules require the use of materials that do little harm to marine ecosystems. The use of ESP in drilling muds not only addresses regulatory issues, but it also helps to reduce the total carbon footprint of drilling operations.

This study's findings are consistent with the overall drive in the oil and gas business toward more sustainable operations that focus on waste reduction and carbon emissions. As observed in earlier research [19], the change to eco-friendly drilling fluids is gaining pace, driven by the requirement for both performance and environmental responsibility. The use of ESP as a weighing agent, together with its good performance in raising mud density and maintaining rheological characteristics, demonstrates its feasibility as a long-term alternative to conventional materials.

To summarize, ESP not only equals the performance of traditional weighing materials, but also provides considerable environmental advantages. Its biodegradability and minimal environmental effect make it a very appealing alternative for drilling operations in the face of tightening environmental restrictions and industry-wide attempts to adopt greener technology.

5. Conclusion

ESP demonstrated comparable or superior performance to $CaCO_3$ across several key drilling fluid parameters. It maintained stable plastic viscosity and yield point values, particularly at higher concentrations, resulting in improved flow characteristics and enhanced wellbore stability. Additionally, ESP exhibited superior filtration efficiency, with more effective mud cake formation. At 20 g, ESP provided an optimal balance between density, plastic viscosity, yield point, and filtration performance, making it a viable and environmentally sustainable alternative for field applications in drilling operations. These findings highlight ESP's potential as a renewable, eco-friendly weighting agent for water-based drilling muds, supporting the industry's shift toward sustainable practices.

Author contributions: Conceptualization, AE and MZ; methodology, AE; software, AE; validation, AE and MZ; formal analysis, MZ; investigation, AE; resources, AE; data curation, AE; writing—original draft preparation, AE; writing—review and editing, MZ; visualization, AE; supervision, MZ; project administration, AE; funding acquisition, MZ. All authors have read and agreed to the published version of the manuscript.

Acknowledgments: The authors declare that they have received no financial or non-financial support that could be considered as a source of competing interest in relation to this research.

Conflict of interest: The authors declare no conflict of interest.

References

1. Zoveidavianpoor M. Drilling Engineering and Technology-Recent Advances New Perspectives and Applications. IntechOpen Publishing; 2022.
2. Alshubbar G, Coryell TN, Atashnezhad A, et al. The effect of barite nanoparticles on the friction coefficient and rheology of water based mud. In: Proceedings of the 51st U.S. Rock Mechanics/Geomechanics Symposium; 25–28 June 2017; San Francisco, CA, USA. p. 0147.
3. Qutob H, Byrne M. Formation damage in tight gas reservoirs. In: Proceedings of the SPE European Formation Damage Conference and Exhibition; 3–5 June 2015; Budapest, Hungary. p. 174237.
4. Kiran R, Teodoriu C, Dadmohammadi Y, et al. Identification and evaluation of well integrity and causes of failure of well integrity barriers (A review). Journal of Natural Gas Science and Engineering. 2017; 45: 511–526.
5. Zoveidavianpoor M, Farahani V. Mud Cap Drilling in a Highly Fractured HPHT Carbonate Formation: A Case Study in an Iranian Offshore Field Persian Gulf. In: Proceedings of the SPE Nigeria Annual International Conference and Exhibition; 1–6 August 2015; Lagos, Nigeria. p. 178302.
6. Shadizadeh SR, Zoveidavianpoor M. A drilling reserve mud pit assessment in Iran: Environmental impacts and awareness. Petroleum science and technology. 2010; 28(14): 1513–1526.
7. Zoveidavianpoor M, Amnan NA, Jaafar MZ. Stabilization of Synthetic-Based Mud by Renewable Resources. In: Proceedings of the 82nd EAGE Annual Conference & Exhibition; 18–21 October 2021; Amsterdam, Netherlands. pp. 1–5.
8. Al-Shargabi M, Davoodi S, Wood DA, et al. Nanoparticle applications as beneficial oil and gas drilling fluid additives: A review. Journal of Molecular Liquids. 2022; 352: 118725.
9. Kristl M, Jurak S, Brus M, et al. Evaluation of calcium carbonate in eggshells using thermal analysis. Journal of Thermal Analysis and Calorimetry. 2019; 138: 2751–2758.
10. Hincke MT, Yves N, Joel G, et al. The eggshell: structure, composition and mineralization. Front Biosci. 2012; 17(1): 1266–1280.
11. Raheem AM, Vipulanandan C. Characterizing distinctive drilling mud properties using new proposed hyperbolic fluid loss model for high pressure and high temperature conditions. Journal of King Saud University-Engineering Sciences. 2020; 34(3): 217–229.
12. Raheem AM. Vipulanandan C. Salt contamination and temperature impacts on the rheological and electrical resistivity behaviors of water-based drilling mud. Energy Sources, Part A: Recovery, Utilization, and Environmental Effects. 2019; 42(3): 344–364.
13. Raheem AM, Vipulanandan C. Testing and modeling of filter cake formation using new seepage-consolidation concept. Engineering Science and Technology, an International Journal. 2019; 22(3): 979–989.
14. Raheem AM. Study the fluid loss and rheological behaviors of bentonite drilling mud contaminated with salt and used motor oil. Petroleum and Coal. 2018; 60(6): 1087–1101.
15. Vipulanandan C, Raheem AM, Basirat B, et al. New kinetic model to characterize the filter cake formation and fluid loss in HPHT process. In: Proceedings of the Offshore Technology Conference; 6–9 May 2019; Houston, TX, USA.
16. Zoveidavianpoor M, Samsuri A. The use of nano-sized Tapioca starch as a natural water-soluble polymer for filtration control in water-based drilling muds. Journal of Natural Gas Science and Engineering. 2016; 34: 832–840.

17. Al-Hameedi A, Alkinani H, Dunn-Norman S. Development of high-performance water-based drilling fluid using biodegradable eco-friendly additives (Peanut Shells). International Journal of Environmental Science and Technology. 2022; 19(6): 4959–4970.
18. Ghosh B, AlCheikh IM, Ghosh G, et al. Development of hybrid drilling fluid and enzyme–acid precursor-based clean-up fluid for wells drilled with calcium carbonate-based drilling fluids. ACS Omega. 2020; 5(40): 25984–25992.
19. Alshubbar, Coryell, Atashnezhad A, Akhtarmaneshet S. The effect of barite nanoparticles on the friction coefficient and rheology of water-based mud. In: Proceedings of the ARMA US Rock Mechanics/Geomechanics Symposium; 25–28 June 2017; San Francisco, CA, USA.

Academic Publishing Pte. Ltd.

Add: 73 Upper Paya Lebar Road #07-02B-01 Centro Bianco Singapore 534818

Tel: +65 83184869

E-mail: editorial_office@acad-pub.com

Web: http://ojs.acad-pub.com/